USE OF PIEZOELECTRIC ACTUATORS TO EFFECT SNAP-THROUGH BEHAVIOR OF UNSYMMETRIC COMPOSITE LAMINATES

by

Marc Robert Schultz

Dissertation submitted to the Faculty of the Virginia Polytechnic Institute and State University in partial fulfillment of the requirements for the degree of

DOCTOR OF PHILOSOPHY

in

Engineering Mechanics

M. W. Hyer, Chairman

A. C. Loos

D. H. Morris

R. H. Plaut

Y. Renardy

April 17, 2003
Blacksburg, Virginia

Key Words: morphing structures, composite materials, unsymmetric laminates, snap-through behavior, MFC™ actuator

USE OF PIEZOELECTRIC ACTUATORS TO EFFECT SNAP-THROUGH BEHAVIOR OF UNSYMMETRIC COMPOSITE LAMINATES

by

Marc Robert Schultz

M. W. Hyer, Chairman
Engineering Mechanics

(ABSTRACT)

As a new concept for morphing structures, the use of piezoelectric actuators to effect snap-through behavior of simple unsymmetric cross-ply composite laminates is examined. Many unsymmetric laminates have more than one stable room-temperature shape and can be snapped through from one stable shape to another. In this new concept for morphing structures, one or more piezoelectric actuators are bonded to unsymmetric laminates, and are then used to snap the laminate from one shape to another. The actuator would be used to change shape, but would not be required to maintain the shape. Using the Rayleigh-Ritz technique, several models are developed to predict the interaction between the base laminate and the actuator. In particular, the voltage (applied to the actuator) needed to snap the laminate is predicted. The NASA-LaRC Macro-Fiber Composite™ (MFC™) actuator is chosen as the actuator of choice for this work. A laminate is manufactured, an actuator is bonded to the laminate, and experiments are performed. Since the agreement between the initial models and experimental results was not good, the models were revised. Good agreement between the predictions of the revised model and experiment is reached. Suggestions for future research directions are presented.

Acknowledgments

First, I would like to thank my advisor, Professor M. W. Hyer, for his help and guidance, both professional and personal, over the years. I would also like to thank the other members of my committee, Professors A. C. Loos, D. H. Morris, R. H. Plaut, and Y. Renardy, for their guidance.

I would like to thank the Department of Engineering Science and Mechanics at Virginia Tech for several years of support; I appreciate the teaching opportunities that were provided to me; in particular, I would like to thank Professors N. E. Dowling, D. H. Morris, and E. G. Henneke.

Many people have given their time to help me with this effort. I would like to thanks Bob Simonds for his assistance in the lab, both teaching and research related. Professor Senthil Vel, now at the University at Maine, was a great help in understanding the mechanics of piezoelectric materials. Brett Williams, Dr. Gyuhae Park, and Professor D. J. Inman of the Center for Intelligent Material Systems and Structures at Virginia Tech were invaluable for their help with our experimental work. I would also like to thank Professor Jie-Fang Li and Christelle Jullian of the Department of Material Science and Engineering at Virginia Tech for their help with the actuation experiments in Professor Viehland's laboratory. Danny Reed gave assistance while we were working in the Composite Fabrication Lab at Virginia Tech. I would like to thank Gabriela Wolford for her assistance with the actuation experiments, particularly for the use of her video equipment and her time. Aaron Caba helped devise a way to measure curvatures and helped with experiments.

Finally, I would like to thank my family for their unwavering support over the years. I would not be where I am without their love and support. In particular, I would like to thank my lovely wife, Meagan, for her encouragement, love, and support.

Table of Contents

List of Figures

List of Tables

Chapter 1 Introduction

Through the combination of fiber-reinforced composites and actuators, it is possible to design structures that have the ability to change shape. Structures that change shape are often termed *morphing structures*. In recent years, the National Aeronautics and Space Administration (NASA) has shown significant interest in morphing structures; much of this interest has been directed toward morphing wings of future aircraft [1,2,3]. In addition, the Air Force [4] and the Defense Advanced Research Projects Agency (DARPA) [3] are conducting research to examine adaptive structures on aircraft. The research described herein focuses on what is felt to be a novel concept for the morphing of structures. The structures considered in this project are multi-layered (laminated) plates with fiber-reinforced composite layers forming the main structure, and piezo-electric layers serving as actuators. The plate material consists of a polymer matrix with graphite reinforcement and requires an elevated temperature to cure the polymer. The considered laminated plates are rather special in that they are unsymmetrically laminated. If a laminate does not have a symmetric stacking sequence, thermally-induced stresses which develop during processing can cause out-of-plane curvature as the laminate cools from the processing temperature to room temperature. Depending on stacking sequence and geometry, these processing stresses may cause the laminate to have more than one stable configuration with out-of-plane curvature at room temperature. Applying a force to such a laminate can cause it to *snap through* from one stable configuration to another, thereby morphing the structure. After snap through, the panel will remain in the new configuration until new forces are applied. The curvature of these multiple configurations can be significantly different, resulting in different structural forms. An advantage of using this characteristic to develop morphing structures is the ability to have multiple shapes without continually suppling power; that is, power is required only to transform the structure from one shape to another and not to hold it in the transformed shape with the continuous application of force.

Piezoelectric materials can be used as actuators to cause the aforementioned snap-through behavior. When an electric potential gradient is applied within a piezoelectric material, strains are developed; likewise, if a piezoelectric material is deformed, an electric potential gradient is generated. Like temperature-induced strains, the strains due to the piezoelectric effect can cause stresses, which in turn can lead to the forces and moments needed to effect the snap-through behavior of the laminate. The structures considered in this document consist of piezoelectric actuators bonded to one or both faces of an unsymmetric graphite-epoxy cross-ply laminate that has more than one stable room-temperature configuration. The piezoelectrically-induced strains produced in the piezoelectric actuator(s) will create the forces and moments necessary to snap the laminate from one stable configuration to another. While a simple laminate, with one or two actuators bonded to one or both faces, is quite far removed from a practical "structure," the work herein is considered as a "proof-of-concept" effort. Questions such as: Does the concept work?, Can the snap-through event be successfully predicted?, What future refinements are necessary? are considered. To study this concept, the research combined several mathematical modeling techniques, using primarily the Rayleigh-Ritz technique, while using elasticity-type solutions and the finite-element method for some model verification. Upon completion of the modeling, experiments were used to confirm that the proposed models accurately predicted the response of unsymmetric laminates to the effects of activating the piezoelectric layers.

1.1 Review of Past Work

Hyer [5,6] successfully modeled the room-temperature shapes of unsymmetric cross-ply graphite-epoxy laminates using the Rayleigh-Ritz technique and classical lamination theory (CLT) with the addition of nonlinear terms in the strain-displacement relations. It was found that, for certain geometric conditions, there were three room-temperature equilibrium shapes: an unstable saddle shape, which is predicted by geometrically-linear classical lamination theory, and two stable cylindrical shapes, which cannot be found without the geometrically-nonlinear terms. For other geometric conditions, there was only the saddle shape, which in these cases was stable. Hamamoto and Hyer [7] continued the work with unsymmetric cross-ply laminates by examining the effects on the laminate shape of raising and lowering the temperature; agreement with experi-

ments was good. Dano and Hyer [8], among others, continued to explore the mechanics of unsymmetric laminates by expanding the Rayleigh-Ritz formulation to more general angle-ply laminates and comparing the predictions with experiments. Dano and Hyer [9] also examined the snap-through behavior of unsymmetric laminates. The snap-through behavior was effected through the use of a post-and-wire system in which the posts provided a moment-arm and the wire, which was loaded with dead weights, transferred the load to the posts. There was good correlation between experimental and predicted results.

Work has been done in the field of smart materials and structures for many years. Because of the fast response of piezoceramics, much of the work concerning piezoceramic actuators has been in vibration analysis, using piezoceramics for both actuation and vibration control. Exact solutions of elementary problems have also been developed. These problems tend to have simple geometry and simple boundary conditions, and are often flat panels. Approximate theories have also been developed and work has been done using these theories; usually, only the linear response is sought. Finite-element solutions as a check of other solutions, or to solve more difficult problems, are also often seen.

Mason [10] discussed the history of piezoelectricity, including the discovery and some applications. The direct piezoelectric effect, namely, an electric response due to applied strains, was discovered by Pierre and Jacques Curie and was first described in 1880. The Curies found several different crystals to be piezoelectric, including quartz and Rochelle salt. The reverse piezoelectric effect, namely, a strain response from applied electric potential gradient, was theorized by other researchers, but experimentally verified by the Curies. The first practical use of the piezoelectric effect was using quartz in a depth-sounding device near the end of World War I. Quartz and Rochelle salt were also used in other acoustic applications such as sound transducers. More recently, piezoelectric ceramics have replaced other materials in most transducer applications. For example, piezoelectrics have been used “a variety of transducers including strain gages, pressure transducers, and accelerometers.” [11].

Cady and Tiersten have written definitive works on piezoelectricity [12,13]. Cady gives an over-

view of the piezoelectric effect in crystals, including some history, causes of the effect in crystals, principles of piezoelectricity, and a number of applications. Much of the work is devoted to dynamic effects and vibrations in crystals. Considerable discussion is given to quartz and Rochelle salt. Tiersten concentrates on plate vibrations and the linear theory of piezoelectricity, giving an overview of linear piezoelectricity, discussing and solving several standing wave problems, and finally discussing some approximations and their uses.

Exact solutions to simple piezoelectric problems have been presented by a number of authors, including Ray et al. [14,15,16], Heyliger et al. [17,18,19], and Benveniste and Dvorak [20]. These papers can best be divided into those that deal with single-layer piezoelectric plates and those that deal with multiple-layer piezoelectric plates. In both cases, the solved problems tend to be restricted to cylindrical bending of semi-infinite plates under simple harmonic electrical or distributed physical loads. The multiple-layer problems are constructed and solved in a manner similar to that of Pagano [21,22] in his work with composite laminates. For the work considered here, these solutions are helpful primarily as a check on the assumptions and results of the simplified theories. For example, Ray et al. [15,16] found that, for thin, single-layer plates with length-to-thickness ratios greater than six, “the deformations, stresses and electric potential vary linearly across the thickness” of the plate. In some of these solutions, dynamic effects are considered [19]. Vel and Batra presented exact solutions of multi-layered piezoelectric plates with arbitrary boundary conditions and examined the boundary layer effect near clamped and free edges [23].

There has also been work that uses approximate theories to solve problems that are more realistic than those that were solved using exact solutions. Crawley et al. [11,24] have looked at beams of various configurations which included segmented piezoelectric actuators. Euler-Bernoulli and modified Euler-Bernoulli beam theories were used in these papers. Aluminum, glass/epoxy, and graphite/epoxy beams were considered. In [24], Crawley and Anderson also examined the effect of a finite-thickness bond layer between the beam and the actuator. Lee [25], and Wang and Rogers [26] have developed classical-lamination-theory-type theories which include piezoelectric effects, but decouple the electromechanical and mechanoelectrical piezoelectric equations. Finally, Huang and Wu [27] contend that most linear piezoelectric approximations are not accu-

rate enough, so they present a coupled first-order shear-deformable piezoelectric theory in which the electric potential is assumed to vary quadratically through the thickness. In addition, several researchers discuss the nonlinearity of piezoelectrics: Crawley and Anderson [24] discuss "non-idealities" including depoling, dependence of the piezoelectric constant, d_{31}, on strain, hysteresis, frequency dependence, and creep, and conclude that if high strain actuation is used, then nonidealities must be considered. Depoling can be avoided, but a mechanism for repoling should be included in a design. It was found that d_{31} is not a linear function of strain and, therefore, Crawley and Anderson suggest defining a secant piezoelectric coefficient, d^*_{31}. Hysteresis can be significant; however, d^*_{31} can be used instead of d_{31} to account for some of the hysteresis. Crawley and Anderson also found the creep and strain rate effects to be small.

Much finite-element work has also been done, often as a comparison to other work or to solve specific problems. Heyliger et al. [28] and Saravanos [29] present piezoelectric finite-element models. Crawley and Anderson [24] use the finite-element method to check the accuracy of their simple models.

Recently, attention is being directed towards fibrous piezoelectric composites instead of monolithic piezoelectric plates [30,31]. These composites generally consist of unidirectional lead zirconate titanate (PZT) fibers embedded in a polymer matrix. Benefits of piezoelectric composites include the ability to use the more powerful 1-1 actuation instead of the usual 3-1 actuation used in monolithic piezoceramics, more robustness, increased flexibility, and the ability to tailor the direction of actuation strains or sensing capability [30]. Janos and Hagood [30] discuss the Active Fiber Composite (AFC) actuator, developed at the Active Materials and Structures Laboratory at the Massachusetts Institute of Technology, which consists of extruded PZT fiber in an epoxy matrix. Several issues have prevented the full realization of the potential benefits of the AFC actuator, including the poor quality of extruded PZT, the nonuniform electric fields near the electrodes, and the low dielectric of the epoxy matrix. Because a significant drawback to piezoelectric composites has been the high cost, Wilkie et al. [31] developed the low-cost NASA Langley Research Center Macro-Fiber Composite™ (LaRC-MFC™ or MFC™) actuator. The MFC actuator is similar to the AFC actuator in that it consists of PZT "fibers" embedded in a polymer matrix

and is actuated using interdigitated electrodes. However, in the case of the MFC actuator, the fibers are rectangular in cross section and are made by dicing a monolithic PZT-5A wafer into fibers. The fibers are embedded in an epoxy matrix and are sandwiched between electroded polyimide films. The MFC actuator solves a number of the problems that plague the AFC actuator, including the quality and cost of the piezoelectric fibers. In addition, with the rectangular fibers, the electrodes can be placed in close proximity to a larger area of the fiber, thereby diminishing the deleterious effect of the low dielectric of the epoxy. As will be seen, the MFC actuator is used in this work.

A review of articles in the field of smart materials and adaptive structures, including several overview articles such as [32,33,34], has found no work that utilizes the multiple equilibrium states of unsymmetric laminates in conjunction with piezoelectric actuators. Hence, the research discussed herein is considered unique.

1.2 Objectives of Research Activities

As mentioned earlier, the work considered consists of studying the feasibility of using piezoelectric actuators to effect the snap-through behavior of unsymmetric composite laminates. In particular, the following question is posed: Can piezoelectric actuators be used to snap a simple, rectangular, two-layer cross-ply laminate? Cross-ply laminates, laminates with only 0° and 90° fiber orientations, are examined because they have the simplest (as opposed to general unsymmetric laminates) laminate stiffness matrices, and modeling the behavior of cross-ply laminates is more straightforward. Unsymmetric cross-ply laminates also have more room-temperature curvature and lower bending stiffnesses than general unsymmetric laminates. More room-temperature curvature will make it more difficult for the actuator to snap the laminate. However, the lower bending stiffness of cross-ply laminates will mitigate this effect. Hence, the cross-ply laminate is a good starting point to study the proposed concept. Although only simple cross-ply laminates are considered, there may be some practical applications for such laminates. For example, as in Figure 1.1, a duct with a transformable cross section could be created. In a certain section of the duct, the sides consist of unsymmetric laminates, while the top and bottom consist of some flexible

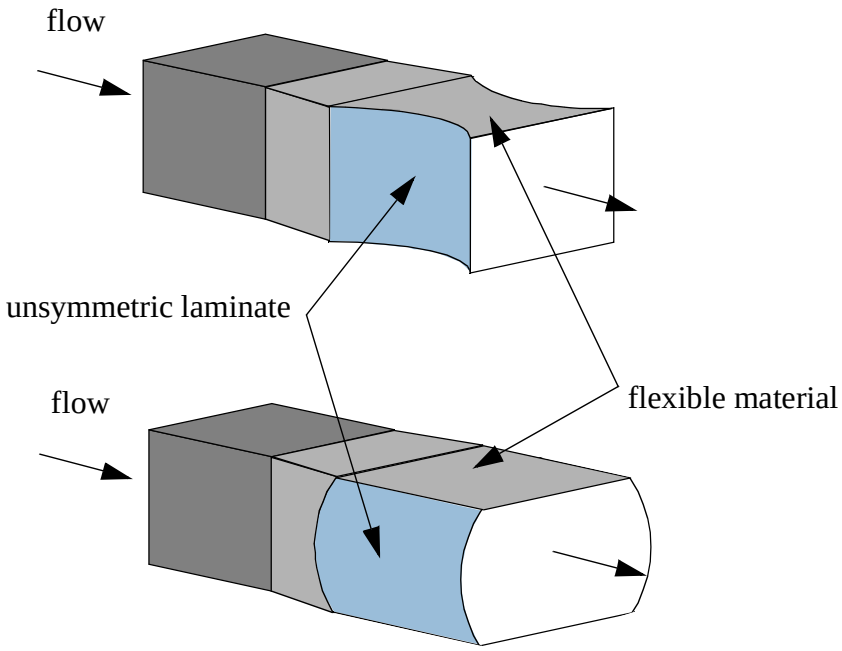

Figure 1.1: Example of application: transformable cross-section duct made with unsymmetric cross-ply laminates

material. When the laminates are in the equilibrium configurations shown in the upper portion of Figure 1.1, the flow through the duct is restricted, but when the laminates are snapped to the configurations shown in the lower portion of the figure, the flow is more free.

The specific objectives of this of this research effort were

- to develop a model to predict the snap-through behavior of simple, rectangular, two layer, unsymmetric cross-ply laminates actuated with piezoelectric actuators,
- to use the model to design an experiment where snap through of such an unsymmetric laminate could be effected with a piezoelectric actuator, and
- to perform the designed experiment to compare with the developed model.

1.3 Outline of Document

Chapter 2 will discuss some initial modeling efforts. Covered will be introductions to unsymmetric laminates, the snap-through behavior thereof, and piezoelectric materials. Chapter 2 will include a discussion of a simple model, which utilizes the Rayleigh-Ritz technique, that examines

the use of piezoceramic actuators to effect snap-through behavior.

The Macro-Fiber Composite actuator is introduced as the actuator of choice for this study in Chapter 3. The constitutive equations for the MFC actuator are given and a way to calibrate the actuation capacity of the MFC actuator is devised and carried out. Details of the calibration experiment are given and the piezoelectric constants are found.

Chapter 4 discusses in-depth modeling of the snap-through behavior of unsymmetric laminates actuated with MFC actuators. The use of the in-depth modeling to select the geometry of laminates for experiments is discussed.

Details of the aforementioned experiments, including model prediction, laminate manufacture, and snap-through experiments are discussed in Chapter 5. The voltage required to effect snap-through behavior of an actuator/laminate structure is compared with the predictions. Discrepancies between experiment and prediction are discussed.

Revised in-depth models are presented in Chapter 6. These revised models take into account certain geometric aspects of the laminates that were observed during the experiments and were felt to be somewhat responsible for the discrepancies between experiment and prediction. The predictions from these revised models are then compared with the experimental results.

Chapter 7 further discusses the correlation between the predictions and the experiments, including reasons for discrepancies. In addition, ideas for future work to continue this research are presented.

A series of appendices go further into some issues that are not directly related to the body of the document, but were important preludes to the work. In addition, a summary of the experimental test results is given.

Chapter 2 Initial Modeling of an Unsymmetric Laminate and Actuators

In order to better understand some of the major issues with piezoelectric materials and their ability to produce snap-through in unsymmetric laminates, a simple, somewhat idealized, model was initially developed. This model included the major features of the more in-depth models that were later developed, but some key simplifications were made. This initial model was intended to provide a broad overview of the concept of using piezoelectric actuators with unsymmetric composite laminates. The model considered an unsymmetric graphite-epoxy laminate with a layer of piezoceramic on both faces of the laminate. The Rayleigh-Ritz technique and classical lamination theory with the inclusion of geometric nonlinearities were used to predict the room-temperature shapes of the laminate and the shapes when the piezoceramic layer was activated by a through-thickness electric field. The model was programmed using the symbolic programming software *Mathematica* [35] and built upon the work by Hyer [5].

2.1 Laminated Composite Materials

The composite laminates throughout this study consist of thin layers, or laminae, that are made of unidirectional graphite fibers in an epoxy matrix, and are manufactured on a flat tool. An arbitrary number of layers may be stacked together with arbitrary ply-orientation angles. In order to consolidate and cure these composite laminates, they are heated under pressure. In the case of symmetric laminates, a panel that is cured on a flat form will remain flat after cure and cooling to the operating temperature. A symmetric laminate is a laminate in which “for every layer to one side of the laminate reference surface with a specific thickness, specific material properties, and specific fiber orientation, there is another layer the identical distance on the *opposite* side of the reference

surface with the identical thickness, material properties, and fiber orientation" [36]. The thermally-induced stresses developed in *unsymmetric* laminates, laminates which are not symmetric, will cause curvature to develop as the panel cools. The laminates of interest in the present study are thin unsymmetric laminates with more than one stable equilibrium state at room temperature.

2.1.1 Modified Classical Lamination Theory

In order to proceed with the analysis, classical lamination theory, but with geometric nonlinearities, was used to model unsymmetric laminates. The coordinate system for this section is the usual system that is used with classical lamination theory, i.e., a structural or global coordinate system in *x*, *y*, and *z*, with the *z* direction as the thickness direction and a material coordinate system in 1, 2, and 3, with the fibers in the 1 direction, and the 3 direction as the thickness direction. Classical lamination theory is a plate theory for laminated composite materials, in which properties are smeared through the thickness and defined at a reference surface, and in-plane loads are defined in terms of force and moment resultants acting on the reference surface. In classical lamination theory, a number of simplifying assumptions are made, including the assumptions that

- the Kirchhoff hypothesis is valid,
- the plane stress assumption (through the thickness stresses are much smaller than in-plane stresses) is valid,
- the material behavior is linearly elastic,
- the strain-displacement equations are linear.

As can be seen, classical lamination theory is an extension of classical linear elastic Kirchhoff theory for homogeneous plates to laminated composite plates. Hyer [5,6] has shown that classical lamination theory cannot always accurately predict the room-temperature shapes of unsymmetric laminates. However, if geometric nonlinearities are included in the theory, by using nonlinear strain-displacement equations, the shapes could be much more accurately predicted. For this reason, nonlinear strain-displacement equations were used in the present work. A summary of the equations that were used in this early modeling effort is given below.

The constitutive equations, in terms of the force and moment resultants, are given by

$$\begin{bmatrix} N_x \\ N_y \\ N_{xy} \\ M_x \\ M_y \\ M_{xy} \end{bmatrix} = \begin{bmatrix} A_{11} & A_{12} & A_{16} & B_{11} & B_{12} & B_{16} \\ A_{12} & A_{22} & A_{26} & B_{12} & B_{22} & B_{26} \\ A_{16} & A_{26} & A_{66} & B_{16} & B_{26} & B_{66} \\ B_{11} & B_{12} & B_{16} & D_{11} & D_{12} & D_{16} \\ B_{12} & B_{22} & B_{26} & D_{12} & D_{22} & D_{26} \\ B_{16} & B_{26} & B_{66} & D_{16} & D_{26} & D_{66} \end{bmatrix} \begin{bmatrix} \varepsilon_x^\circ \\ \varepsilon_y^\circ \\ \gamma_{xy}^\circ \\ \kappa_x^\circ \\ \kappa_y^\circ \\ \kappa_{xy}^\circ \end{bmatrix} - \begin{bmatrix} N_x^D \\ N_y^D \\ N_{xy}^D \\ M_x^D \\ M_y^D \\ M_{xy}^D \end{bmatrix} \tag{2.1}$$

where the *N*s and *M*s are the force and moment resultants; the *A*s, *B*s, and *D*s are the components of the well-known *ABD* matrix; the ε°s and κ°s are the midplane strains and curvatures; and the N^Ds and M^Ds are effective force and moment resultants. The strains are given by the simplified nonlinear strain-displacement relations for small strains and moderate rotations:

$$\begin{aligned} \varepsilon_x^\circ &= \frac{\partial u^\circ}{\partial x} + \frac{1}{2}\left(\frac{\partial w^\circ}{\partial x}\right)^2 \\ \varepsilon_y^\circ &= \frac{\partial v^\circ}{\partial y} + \frac{1}{2}\left(\frac{\partial w^\circ}{\partial y}\right)^2 \\ \gamma_{xy}^\circ &= \frac{\partial u^\circ}{\partial y} + \frac{\partial v^\circ}{\partial x} + \left(\frac{\partial w^\circ}{\partial x}\right)\left(\frac{\partial w^\circ}{\partial y}\right) \end{aligned} \tag{2.2}$$

where u°, v°, and w° are the midplane displacements in the *x*, *y*, and *z* directions, respectively. The terms involving w° are the nonlinear terms. The equations for the curvatures in terms of the displacements are

$$\kappa_x^\circ = -\frac{\partial^2 w^\circ}{\partial x^2}$$
$$\kappa_y^\circ = -\frac{\partial^2 w^\circ}{\partial y^2} \tag{2.3}$$
$$\kappa_{xy}^\circ = -2\frac{\partial^2 w^\circ}{\partial x \partial y}$$

The effective force and moment resultants take into account both thermal and piezoelectric strain effects and are defined as

$$N_x^D \equiv \int_{-\frac{H}{2}}^{\frac{H}{2}} (\varepsilon_x^D \ \overline{Q}_{11} + \varepsilon_y^D \ \overline{Q}_{12} + \gamma_{xy}^D \ \overline{Q}_{16}) dz$$
$$N_y^D \equiv \int_{-\frac{H}{2}}^{\frac{H}{2}} (\varepsilon_x^D \ \overline{Q}_{12} + \varepsilon_y^D \ \overline{Q}_{22} + \gamma_{xy}^D \ \overline{Q}_{26}) dz$$
$$N_{xy}^D \equiv \int_{-\frac{H}{2}}^{\frac{H}{2}} (\varepsilon_x^D \ \overline{Q}_{16} + \varepsilon_y^D \ \overline{Q}_{26} + \gamma_{xy}^D \ \overline{Q}_{66}) dz \tag{2.4}$$
$$M_x^D \equiv \int_{-\frac{H}{2}}^{\frac{H}{2}} (\varepsilon_x^D \ \overline{Q}_{11} + \varepsilon_y^D \ \overline{Q}_{12} + \gamma_{xy}^D \ \overline{Q}_{16}) z dz$$
$$M_y^D \equiv \int_{-\frac{H}{2}}^{\frac{H}{2}} (\varepsilon_x^D \ \overline{Q}_{12} + \varepsilon_y^D \ \overline{Q}_{22} + \gamma_{xy}^D \ \overline{Q}_{26}) z dz$$
$$M_{xy}^D \equiv \int_{-\frac{H}{2}}^{\frac{H}{2}} (\varepsilon_x^D \ \overline{Q}_{16} + \varepsilon_y^D \ \overline{Q}_{26} + \gamma_{xy}^D \ \overline{Q}_{66}) z dz$$

where H is the laminate thickness and the $\overline{Q}$s are the transformed reduced stiffnesses. The ε^Ds and the γ^Ds are effective strains, take into account both thermal and piezoelectric effects, and are defined as

$$\begin{aligned} \varepsilon_x^D &\equiv \varepsilon_x^T + \varepsilon_x^E \\ \varepsilon_y^D &\equiv \varepsilon_y^T + \varepsilon_y^E \\ \gamma_{xy}^D &\equiv \gamma_{xy}^T + \gamma_{xy}^E \end{aligned} \tag{2.5}$$

The superscript "*T*" represents thermally-induced strain effects and the superscript "*E*" represents piezoelectrically-induced strains effects. The strains caused by temperature change are given by

$$\begin{aligned} \varepsilon_x^T &= \alpha_x \Delta T \\ \varepsilon_y^T &= \alpha_y \Delta T \\ \gamma_{xy}^T &= \alpha_{xy} \Delta T \end{aligned} \tag{2.6}$$

where

$$\begin{aligned} \alpha_x &= \alpha_1 \cos^2\theta + \alpha_2 \sin^2\theta \\ \alpha_y &= \alpha_1 \sin^2\theta + \alpha_2 \cos^2\theta \\ \alpha_{xy} &= 2(\alpha_1 - \alpha_2)\cos\theta \sin\theta \end{aligned} \tag{2.7}$$

and θ is the fiber angle relative to the *x* axis. The quantities α_1 and α_2 are the thermal expansion coefficients in the principal material coordinate system, and ΔT is the change in temperature from the cure temperature. The strains caused by the piezoelectric actuation will be discussed in Section 2.2.

2.1.2 Unsymmetric Cross-Ply Laminates

When the discussion is limited to anti-symmetric cross-ply laminates, as will be done throughout

this initial modeling effort, several simplifications can be made to equation (2.1). In particular, A_{16}, A_{26}, B_{12}, B_{16}, B_{26}, D_{16}, D_{26}, and α_{xy} are zero for such laminates and equation (2.1) becomes

$$\begin{bmatrix} N_x \\ N_y \\ N_{xy} \\ M_x \\ M_y \\ M_{xy} \end{bmatrix} = \begin{bmatrix} A_{11} & A_{12} & 0 & B_{11} & 0 & 0 \\ A_{12} & A_{22} & 0 & 0 & -B_{11} & 0 \\ 0 & 0 & A_{66} & 0 & 0 & B_{66} \\ B_{11} & 0 & 0 & D_{11} & D_{12} & 0 \\ 0 & -B_{11} & 0 & D_{12} & D_{22} & 0 \\ 0 & 0 & B_{66} & 0 & 0 & D_{66} \end{bmatrix} \begin{bmatrix} \varepsilon_x^\circ \\ \varepsilon_y^\circ \\ \gamma_{xy}^\circ \\ \kappa_x^\circ \\ \kappa_y^\circ \\ \kappa_{xy}^\circ \end{bmatrix} - \begin{bmatrix} N_x^D \\ N_y^D \\ N_{xy}^D \\ M_x^D \\ M_y^D \\ M_{xy}^D \end{bmatrix} \tag{2.8}$$

which allows for the decoupling of this equation, namely,

$$\begin{bmatrix} N_x \\ N_y \\ M_x \\ M_y \end{bmatrix} = \begin{bmatrix} A_{11} & A_{12} & B_{11} & 0 \\ A_{12} & A_{22} & 0 & B_{22} \\ B_{11} & 0 & D_{11} & D_{12} \\ 0 & B_{22} & D_{12} & D_{22} \end{bmatrix} \begin{bmatrix} \varepsilon_x^\circ \\ \varepsilon_y^\circ \\ \kappa_x^\circ \\ \kappa_y^\circ \end{bmatrix} - \begin{bmatrix} N_x^D \\ N_y^D \\ M_x^D \\ M_y^D \end{bmatrix} \tag{2.9}$$

$$\begin{bmatrix} N_{xy} \\ M_{xy} \end{bmatrix} = \begin{bmatrix} A_{66} & B_{66} \\ B_{66} & D_{66} \end{bmatrix} \begin{bmatrix} \gamma_{xy}^\circ \\ \kappa_{xy}^\circ \end{bmatrix} - \begin{bmatrix} N_{xy}^D \\ M_{xy}^D \end{bmatrix}$$

Because, in the current discussion, there are no applied force or moment resultants and no effective shear force or moment resultants due to temperature or piezoelectric effects, the shear strain and twist curvature will be zero. Therefore, only the first equation of equation (2.9) will be considered.

2.2 Piezoelectric Plates

The three-dimensional piezoelectric constitutive equations (see equations (A.1) and (A.2) in Appendix A) can also be simplified for plate-type analyses. In the simplified version, the electromechanical and mechanoelectrical effects are assumed to be decoupled, so the effect of an applied electric potential gradient on an unconstrained volume is just a strain. For piezoelectric plates that are poled in the x_3 direction, the simplified relationships between the applied gradient in the electric potential, ϕ, and the strains in the principal material coordinate system become

$$\begin{aligned} \varepsilon_1^E &= d_{31}\frac{d\phi}{dx_3} \\ \varepsilon_2^E &= d_{32}\frac{d\phi}{dx_3} \\ \gamma_{12}^E &= 0 \end{aligned} \tag{2.10}$$

where the d_{31} and d_{32} are the piezoelectric constants and $d\phi/dx_3$ represents the gradient in the electric potential; the gradient in the electric potential is commonly referred to as the electric field. Orthotropic material behavior has been assumed. As a simplification, since the electromechanical and mechanoelectrical equations are assumed uncoupled, it is also assumed that the gradient in equation (2.10) is independent of thickness location. This is what Ray et al. [15,16] essentially found to be the case, as mentioned in Section 1.1. Here this assumption is verified in Appendix A with the solution of Problems II, III, and IV.

As with the thermally-induced strains of equation (2.6), the piezoelectrically-induced strains in the *x-y* coordinate system are

$$\begin{aligned} \varepsilon_x^E &= \varepsilon_1^E \cos^2\theta' + \varepsilon_2^E \sin^2\theta' \\ \varepsilon_y^E &= \varepsilon_1^E \sin^2\theta' + \varepsilon_2^E \cos^2\theta' \\ \gamma_{xy}^E &= 2(\varepsilon_1^E - \varepsilon_2^E)\cos\theta' \sin\theta' \end{aligned} \tag{2.11}$$

where θ' is the angle between the piezoelectric material coordinate system and the structural coordinate system. Because piezoelectric materials often show in-plane isotropy, equation (2.11) is often not needed. The derivation of the piezoelectric constants, d_{31} and d_{32}, from the three-dimensional piezoelectric coefficients is given in Appendix B.

2.3 Initial Model

The initial model consisted of a two-dimensional $[90°/90°/0°/0°]_T$ graphite/epoxy (Gr/Ep) laminate sandwiched between monolithic layers of PZT piezoceramic to form a $[PZT/90°/90°/0°/0°/PZT]_T$ laminate, as shown in Figure 2.1; only rectangular plates, with side lengths L_x and L_y, were considered. Additional simplifications were made to reduce the complexity of the model: it was assumed that the piezoceramic layers were applied at the epoxy cure temperature, a condition for which the composite laminate has no curvature, and any adhesive layer and the thin electrode layers that would be on the top and bottom faces of the piezoceramic layers were ignored. The Rayleigh-Ritz technique was used to determine actuated and unactuated room-temperature shapes of these laminates.

2.3.1 Initial Model Based on the Rayleigh-Ritz Technique

With the Rayleigh-Ritz technique, approximate displacement fields are assumed in terms of undetermined parameters and the total potential energy is made stationary with respect to the undetermined parameters in the displacement fields. The total potential energy, Π, for a rectangular plate with no external loads can be represented as

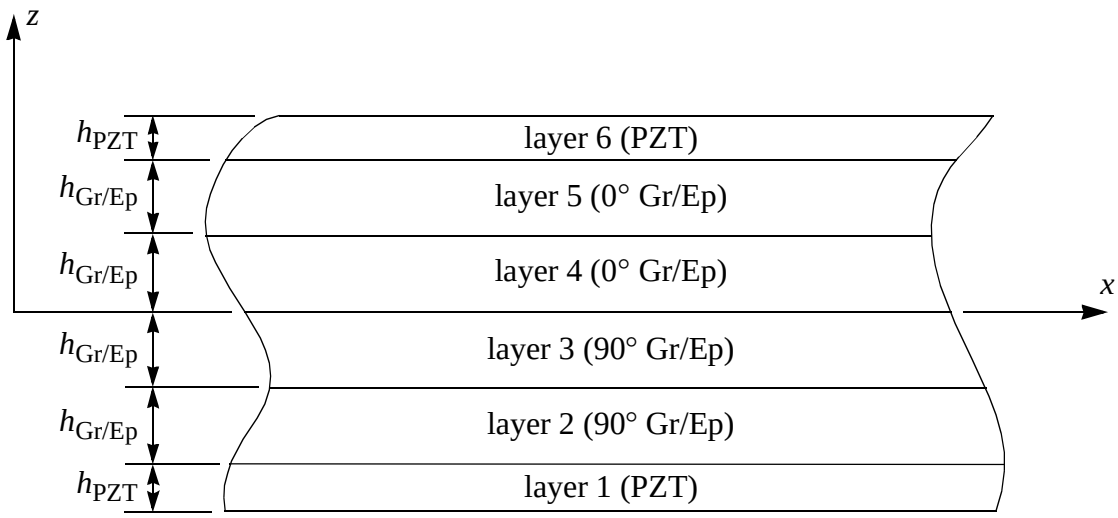

Figure 2.1: Cross-sectional geometry of initial model

$$\Pi = \frac{1}{2}\int_{-\frac{L_x}{2}}^{\frac{L_x}{2}}\int_{-\frac{L_y}{2}}^{\frac{L_y}{2}} [(N_x - N_x^D)\varepsilon_x^\circ + (N_y - N_y^D)\varepsilon_y^\circ + (N_{xy} - N_{xy}^D)\gamma_{xy}^\circ + (M_x - M_x^D)\kappa_x^\circ + (M_y - M_y^D)\kappa_y^\circ + (M_{xy} - M_{xy}^D)\kappa_{xy}^\circ]\,dx\,dy \tag{2.12}$$

In order for the Rayleigh-Ritz technique to be effective, displacement fields that accurately represent the displacements are needed. It has been shown that, for rectangular unsymmetric cross-ply laminates, the room-temperature shapes can be accurately represented by the following displacement fields [5,6]:

$$\begin{aligned} u^\circ(x,y) &= c_3 x - \frac{c_1^2 x^3}{6} - \frac{c_1 c_2 x y^2}{4} \\ v^\circ(x,y) &= c_4 y - \frac{c_2^2 y^3}{6} - \frac{c_1 c_2 x^2 y}{4} \\ w^\circ(x,y) &= \frac{1}{2}(c_1 x^2 + c_2 y^2) \end{aligned} \tag{2.13}$$

where $c_1 - c_4$ are the undetermined parameters, or coefficients, which will be varied to minimize

the total potential energy. After substituting equation (2.13) into equations (2.2) and (2.3), the midplane strains and curvatures become

$$\begin{aligned} \varepsilon_x^\circ &= c_3 - \frac{c_1 c_2 y^2}{4} \\ \varepsilon_y^\circ &= c_4 - \frac{c_1 c_2 x^2}{4} \\ \gamma_{xy}^\circ &= 0 \end{aligned} \tag{2.14}$$

and

$$\begin{aligned} \kappa_x^\circ &= -c_1 \\ \kappa_y^\circ &= -c_2 \\ \kappa_{xy}^\circ &= 0 \end{aligned} \tag{2.15}$$

It should be noted that, as shown in equation (2.15), coefficients c_1 and c_2 are just the negative of the curvatures in the x and y directions, respectively.

Once equations (2.14) and (2.15) are substituted into equation (2.9) and, in turn, into equation (2.12) and the spatial integrals carried out, the equation for the total potential energy is reduced to an algebraic equation in terms of the undetermined coefficients, $c_1 - c_4$. Stationary solutions of Π are found by setting the first variation of the total potential energy, $\delta\Pi$, to zero. This reduces to solving a series of simultaneous algebraic equations for the undetermined coefficients, specifically, setting the partial derivatives of Π with respect to $c_1 - c_4$ equal to zero, and solving for $c_1 - c_4$ from:

$$\frac{\partial \Pi}{\partial c_1} = 0 \qquad \frac{\partial \Pi}{\partial c_2} = 0 \qquad \frac{\partial \Pi}{\partial c_3} = 0 \qquad \frac{\partial \Pi}{\partial c_4} = 0 \tag{2.16}$$

These solutions correspond to the equilibrium shapes of the laminate. If Π has been minimized, the equilibrium solution is a stable solution, and if the Π has not been minimized, the solution is unstable. In order for the solution to be stable, the second variation, $\delta^2\Pi$, must be positive definite. For the current problem, if the matrix

$$\begin{bmatrix} \frac{\partial}{\partial c_1}\left(\frac{\partial \Pi}{\partial c_1}\right) & \frac{\partial}{\partial c_2}\left(\frac{\partial \Pi}{\partial c_1}\right) & \frac{\partial}{\partial c_3}\left(\frac{\partial \Pi}{\partial c_1}\right) & \frac{\partial}{\partial c_4}\left(\frac{\partial \Pi}{\partial c_1}\right) \\ \frac{\partial}{\partial c_1}\left(\frac{\partial \Pi}{\partial c_2}\right) & \frac{\partial}{\partial c_2}\left(\frac{\partial \Pi}{\partial c_2}\right) & \frac{\partial}{\partial c_3}\left(\frac{\partial \Pi}{\partial c_2}\right) & \frac{\partial}{\partial c_4}\left(\frac{\partial \Pi}{\partial c_2}\right) \\ \frac{\partial}{\partial c_1}\left(\frac{\partial \Pi}{\partial c_3}\right) & \frac{\partial}{\partial c_2}\left(\frac{\partial \Pi}{\partial c_3}\right) & \frac{\partial}{\partial c_3}\left(\frac{\partial \Pi}{\partial c_3}\right) & \frac{\partial}{\partial c_4}\left(\frac{\partial \Pi}{\partial c_3}\right) \\ \frac{\partial}{\partial c_1}\left(\frac{\partial \Pi}{\partial c_4}\right) & \frac{\partial}{\partial c_2}\left(\frac{\partial \Pi}{\partial c_4}\right) & \frac{\partial}{\partial c_3}\left(\frac{\partial \Pi}{\partial c_4}\right) & \frac{\partial}{\partial c_4}\left(\frac{\partial \Pi}{\partial c_4}\right) \end{bmatrix} \tag{2.17}$$

is positive definite, then the equilibrium solution is stable.

2.3.2 Numerical Example

Using the geometry of Figure 2.1, an example problem is examined. This problem consists of a six-layer square plate with PZT and graphite/epoxy layers each 0.125 mm thick and side lengths of 0.25 m. The material properties for each layer are given in Table 2.1. The two piezoceramic layers are considered to be isotropic. It is assumed that the laminate is cooled 156 °C from the curing temperature to the operating temperature, room temperature.

When cooled to room temperature, the laminate has three equilibrium shapes: two stable cylindri-

Table 2.1: Assumed layer properties used in the initial model

Quantity	Gr/Ep	PZT
E_1 (GPa)	181.0	69.0
E_2 (GPa)	10.3	69.0
G_{12} (GPa)	7.17	———
ν_{12}	0.28	0.3
α_1 (/°C)	-0.106×10^{-6}	2.0×10^{-6}
α_2 (/°C)	25.6×10^{-6}	2.0×10^{-6}
d_{31} (m/V)	0	-122×10^{-12}

cal shapes and an unstable saddle shape; these as-cooled shapes are shown in Figure 2.2. As can be seen, the saddle, Figure 2.2c, is flat relative to the cylinders, and because it is unstable, the saddle shape will never actually occur. One can snap the laminate from one cylinder to the other through the application of forces, or, as will be seen, through electrical actuation of the piezoelectric layers.

The shapes may also be represented by the curvatures κ_x° and κ_y° (recall that $c_1 = -\kappa_x^\circ$ and $c_2 = -\kappa_y^\circ$). In order to explore the effect of actuating the piezoceramic layers, the curvatures κ_x° and κ_y° are plotted as a function of electric field in Figure 2.3. The electric field was applied in opposite directions in the top and bottom piezoceramic layers so that, when the top piezoceramic layer contracted in its plane, the bottom piezoceramic layer would expand; the electric field in layer 1, the top layer, is used for the independent axis in Figure 2.3. As an example of how piezoelectric actuation could be used to effect snap-through behavior, consider a laminate in the shape shown by point 3 in Figures 2.2 and 2.3. In the shape of point 3, the laminate has considerable curvature in the *y* direction, but little curvature in the *x* direction. If the electric field in layer 1 is increased in the positive direction (negatively increased in layer 6), the magnitude of the curvature in the *x* direction, though small, gradually increases, while the curvature in the *y* direction decreases. These trends continue until point 4 is reached, corresponding to an electric field strength of about 8×10^5 V/m, where, if the electric field is further increased, the laminate will suddenly snap to the

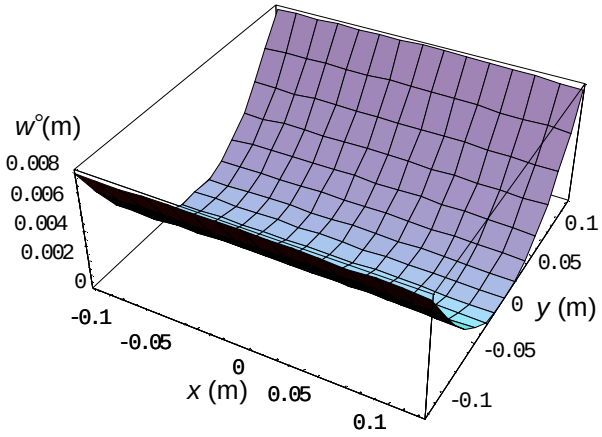

point 3
(a) - a stable cylindrical shape

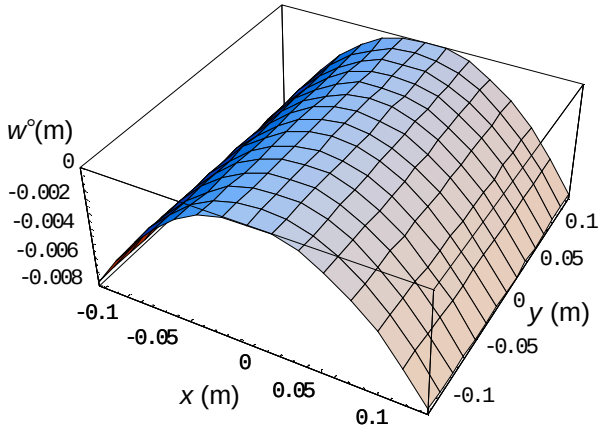

point 1
(b) - the other stable cylindrical shape

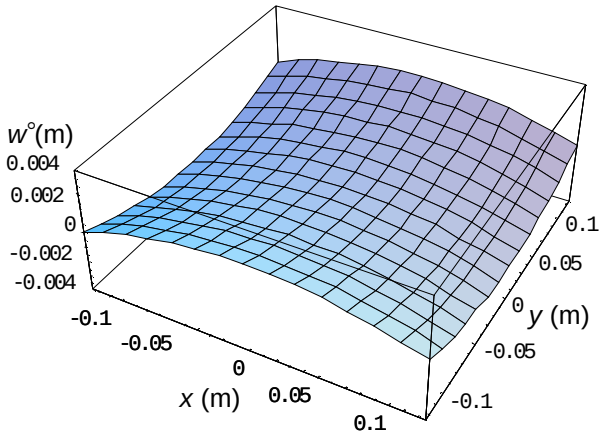

point 2
(c) - the unstable saddle shape

Figure 2.2: As-cooled room-temperature shapes

shape of point 5, with little curvature in the *y* direction and a large curvature in the *x* direction. When the electric field is reduced to zero, the laminate is in the shape of point 1. The laminate has had the shape changed from one with the major curvature in the *y* direction to one with the major curvature in the *x* direction, and no power is needed to keep the laminate in this new shape. This is the phenomenon that is focused upon in this research effort.

In this initial model, it has been demonstrated that a change of shape induced by piezoceramic actuation is possible. However, it has been assumed that the actuators are monolithic layers of

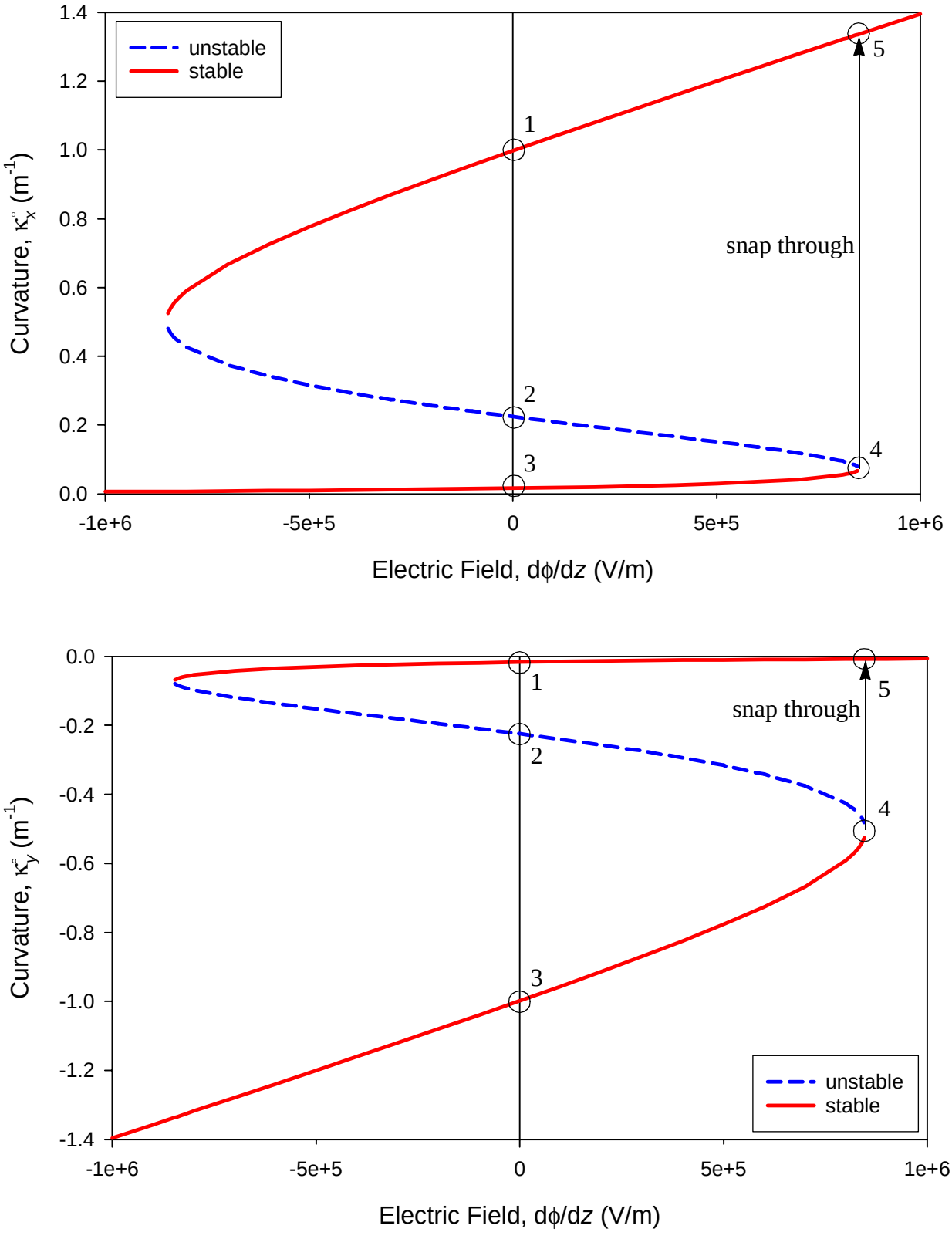

Figure 2.3: Curvatures vs. electric field in layer 1

PZT, that they cover the entire plate surface, and that they were bonded to the laminate at the laminate cure temperature. In fact, it is unlikely that covering the entire surface of both sides of the laminate with a monolithic layer of piezoceramic material is feasible. Also, it is more practical to consider bonding the piezoceramic material to the cooled laminate after the laminate has been manufactured as a separate step. This avoids exposing the piezoceramic material to an elevated temperature. The next chapter describes the actuator actually used in this study, namely, the Macro-Fiber Composite actuator.

Chapter 3 The Macro-Fiber Composite Actuator

During the course of this research, a new piezoelectric actuator, the NASA Langley Research Center Macro-Fiber Composite (LaRC-MFC or MFC) actuator, evolved as a viable alternative to using a monolithic piezoelectric material, as was assumed in the previous chapter (see Figure 2.1). The MFC actuator, which was used in this research effort, is a low-cost piezocomposite actuator with orthotropic mechanical and actuation properties.

3.1 Details of the MFC Actuator

The MFC actuator consists of piezoceramic PZT cross-sectionally rectangular *macrofibers* embedded in an epoxy matrix and sandwiched between polyimide films that have attached interdigitated electrode patterns, as shown in Figure 3.1. The piezoceramic fibers are cut from a monolithic PZT wafer using a dicing saw. The piezoceramic fibers are then coated with epoxy, sandwiched between electroded polyimide films, and cured under heat and pressure. The interdigitated electrodes are placed perpendicular to the fibers and are used for both poling and actuation. Because poling and the primary actuation take place in the same direction, the MFC fiber direction, or the 1 direction, this setup uses the stronger d_{11} piezoelectric constant for the main actuation effect.

Two-dimensional modeling of the MFC actuator can be done in a manner very similar to the modeling of the monolithic piezoelectric plate in the previous chapter. Because the MFC actuator uses the d_{11} actuation instead of the d_{31} actuation used in the monolithic piezoelectric plate, the equations for the piezoelectrically-induced strains (given as equation (2.10) for the monolithic piezo-

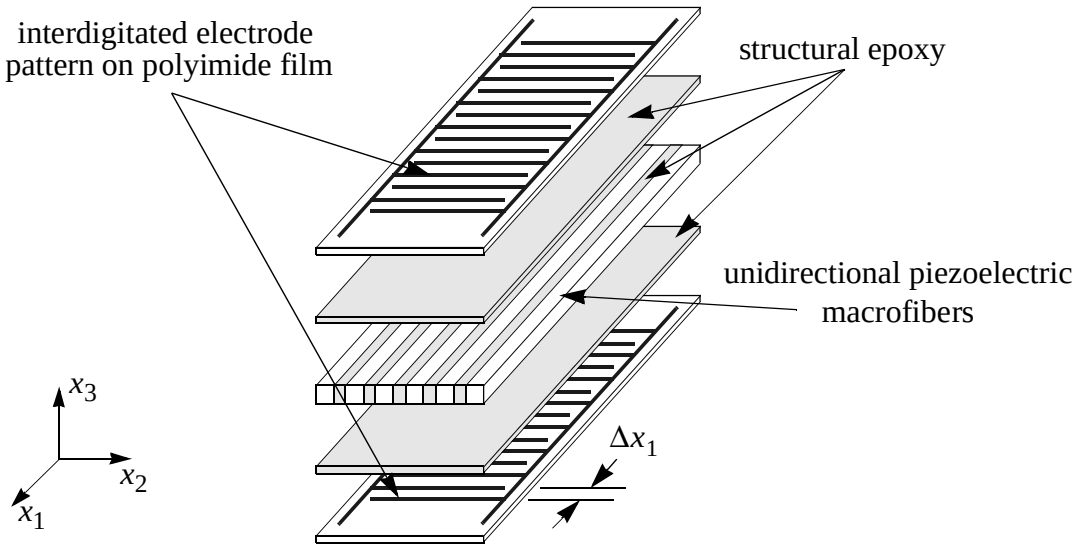

Figure 3.1: MFC actuator (adapted from [31])

electric) are slightly different. For the MFC actuator, these relations are

$$\begin{aligned} \varepsilon_1^E &= d_{11}\frac{\Delta V}{\Delta x_1} \\ \varepsilon_2^E &= d_{12}\frac{\Delta V}{\Delta x_1} \\ \gamma_{12}^E &= 0 \end{aligned} \tag{3.1}$$

where d_{11} and d_{12} are the effective piezoelectric constants for the MFC actuator, ΔV is the voltage applied to the MFC actuator, and Δx_1 is the electrode spacing. There are no induced shear strains. The transformation equations, equation (2.11), still hold for the MFC, where θ' is the angle between the piezoelectric macrofibers and the global, or structural, x axis.

3.2 Calibration of the MFC Actuator

Because the MFC actuator is still under development and there are various styles and designs, it was believed prudent to calibrate the actuation capabilities of the particular actuators that were to

be used in the research. A calibration experiment was devised to measure the actuation potential of the MFC actuators. A finite-element analysis of the calibration experiment was used to determine the major piezoelectric constant, d_{11}, based on the data from the experiment.

3.2.1 Calibration Experiment

The idea behind the calibration experiment was to bond an MFC actuator to a thin aluminum plate, clamp one edge of the plate, and measure displacement of the opposite, free edge, as the actuator was actuated. Figure 3.2 shows a planform schematic of the aluminum plate with MFC actuator: as the actuator was actuated, the free-edge displacement of the plate, measured by three linear variable differential transformers (LVDTs) distributed along the free edge, was read, recorded, and plotted using LabVIEW software and a personal computer. To proceed with the calibration experiment, the aluminum plate and the MFC actuator were cleaned and prepared for the adhesive, Epotek 301 two-part epoxy; the epoxy was mixed and applied to the aluminum plate, and the actuator was positioned on the plate. Vacuum pressure was used to provide pressure while the epoxy was curing; the plate and actuator were placed on a flat tool with a vacuum bag on one side and a vacuum was drawn to press the actuator against the plate. When the epoxy had cured, the aluminum plate was removed from the vacuum bag and one end was clamped into a test fixture. The free portion of the aluminum plate was 232 mm long, 102 mm wide, and 0.79 mm thick. The dimensions of the active portion of the MFC actuator were 86 mm in the piezoelectric fiber direction and 57 mm perpendicular to the fibers. Figure 3.3 shows the experimental setup. In Figure 3.3a, the overall layout is shown; the aluminum plate and the three vertical LVDTs are seen near the center of the figure. Also seen are the computer with a LabVIEW plot, displacement as a function of time, on the screen, and the voltage supply. Figure 3.3b shows a view similar to that of the diagram of Figure 3.2; on the left are the three LVDTs and the aluminum plate with the MFC actuator is seen to the right, positioned beneath the LVDTs. The LVDTs were numbered, from top to bottom in Figure 3.3b, LVDT (0), LVDT (1), and LVDT (2).

The voltage supply that was used had a nominal maximum voltage of 1000V, so ±1000 V were the voltage limits for the calibration. In order to calibrate the actuator, the magnitude of the volt-

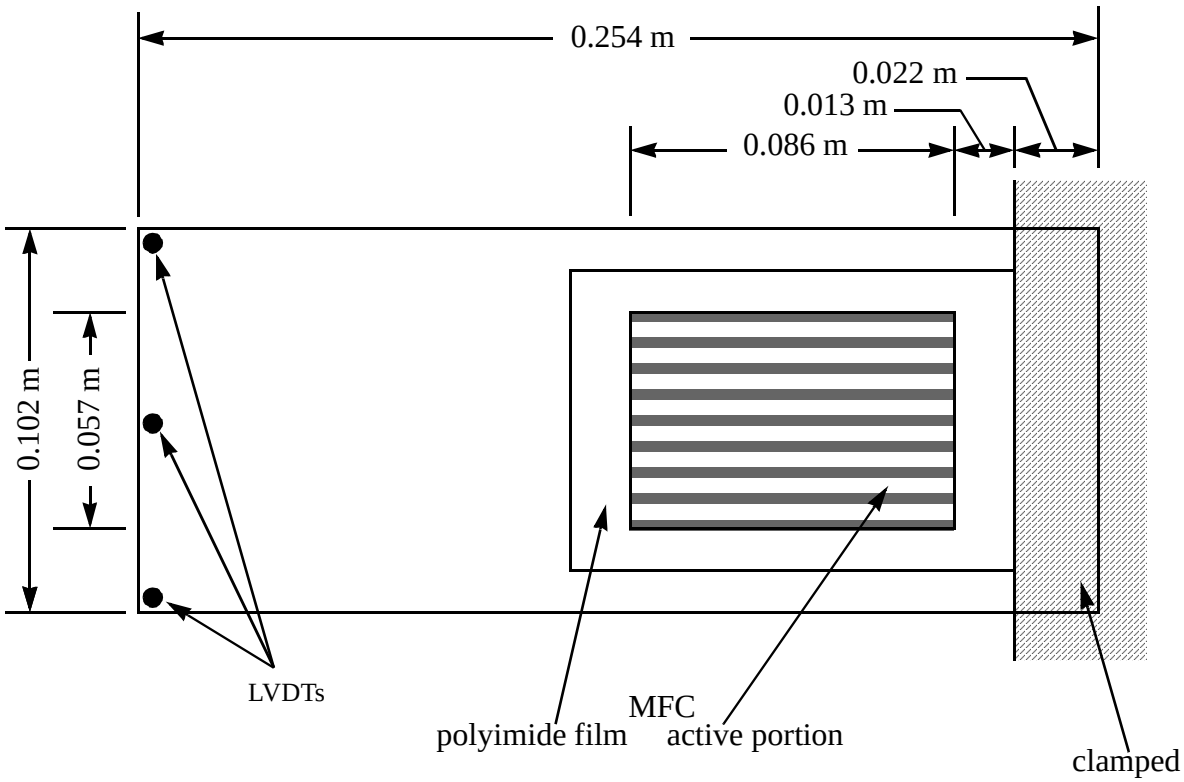

Figure 3.2: Planform view of experimental setup for the calibration experiments

age was slowly increased from zero to a particular voltage, held at that voltage for a time, and then slowly decreased back to zero. The sequence of voltages that were aimed for were 250 V, 500 V, 750 V, 1000 V, −250 V, −250 V, −500 V, −750 V, −1000 V, 250 V, 500 V, 750 V, 1000 V, 750 V, 500 V, 250 V. An example of one of these free-edge displacement versus time plots is seen in Figure 3.4; the maximum voltage that was applied in this figure was −752 V. The displacements from all three LVDTs are shown in the figure and all are quite close to each other. It is also seen in Figure 3.4 that the zero-voltage displacement is not the same before and after the application of the voltage. This difference in displacement, i.e., the displacement not returning to zero with zero voltage, was seen in a number of the calibration tests. Examination of the series of all calibration tests showed this displacement difference was a hysteresis effect. If a voltage was applied to the MFC actuator that was higher than any previous voltage of the same sign since the last reversal of voltage, the displacement difference would be seen. If a smaller voltage of the same sign was applied, the displacement would return to the starting position, and if the voltage was reversed, the displacement difference would again be seen.

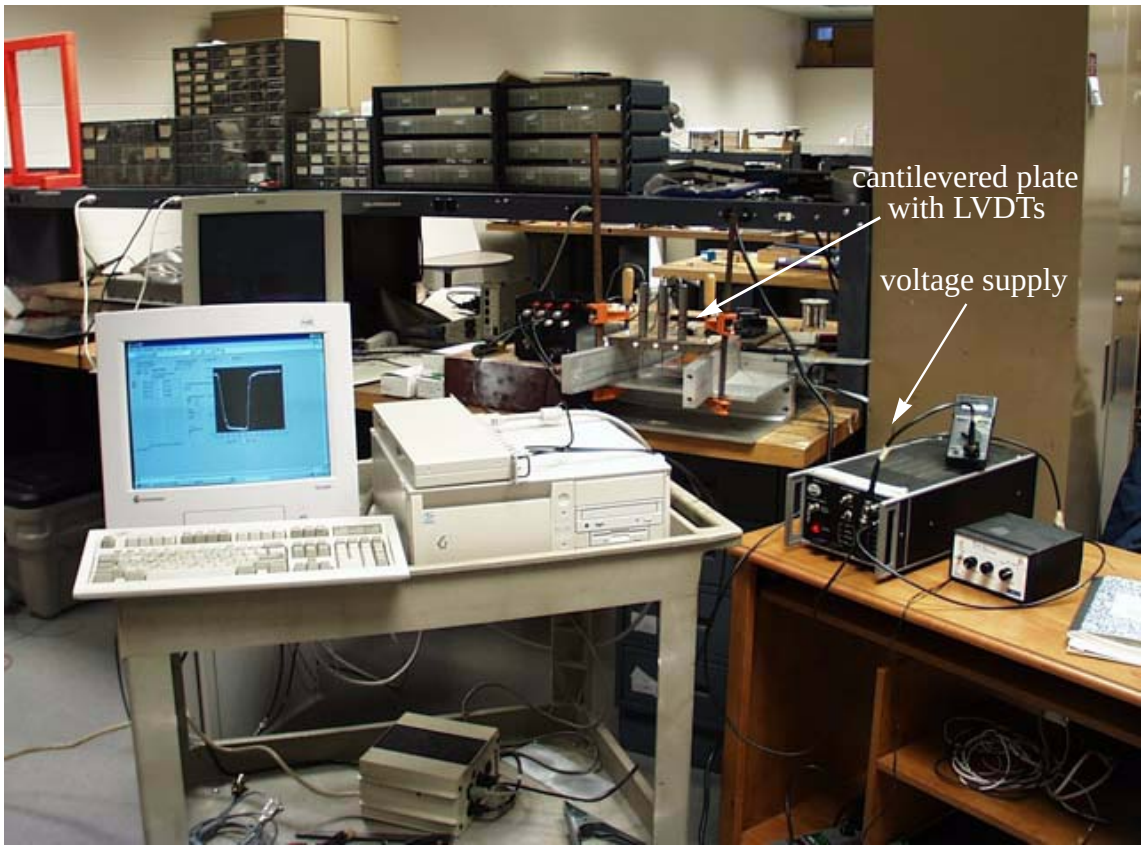

(a) - overall setup

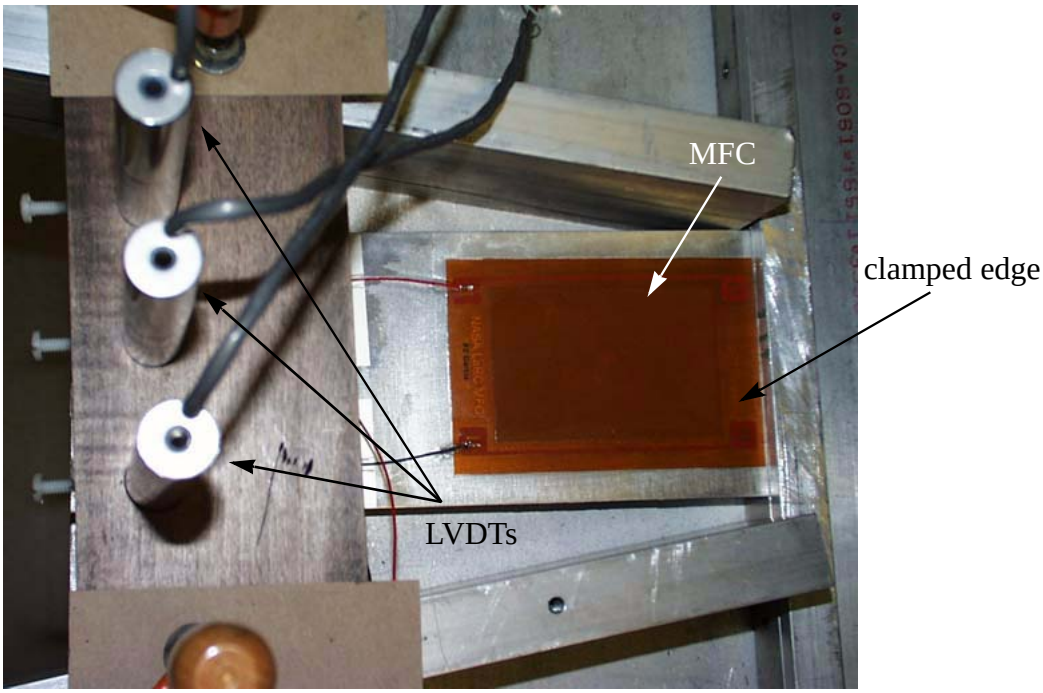

(b) - detail of the cantilevered plate, MFC actuator, and LVDTs

Figure 3.3: Setup for the MFC actuator calibration experiments

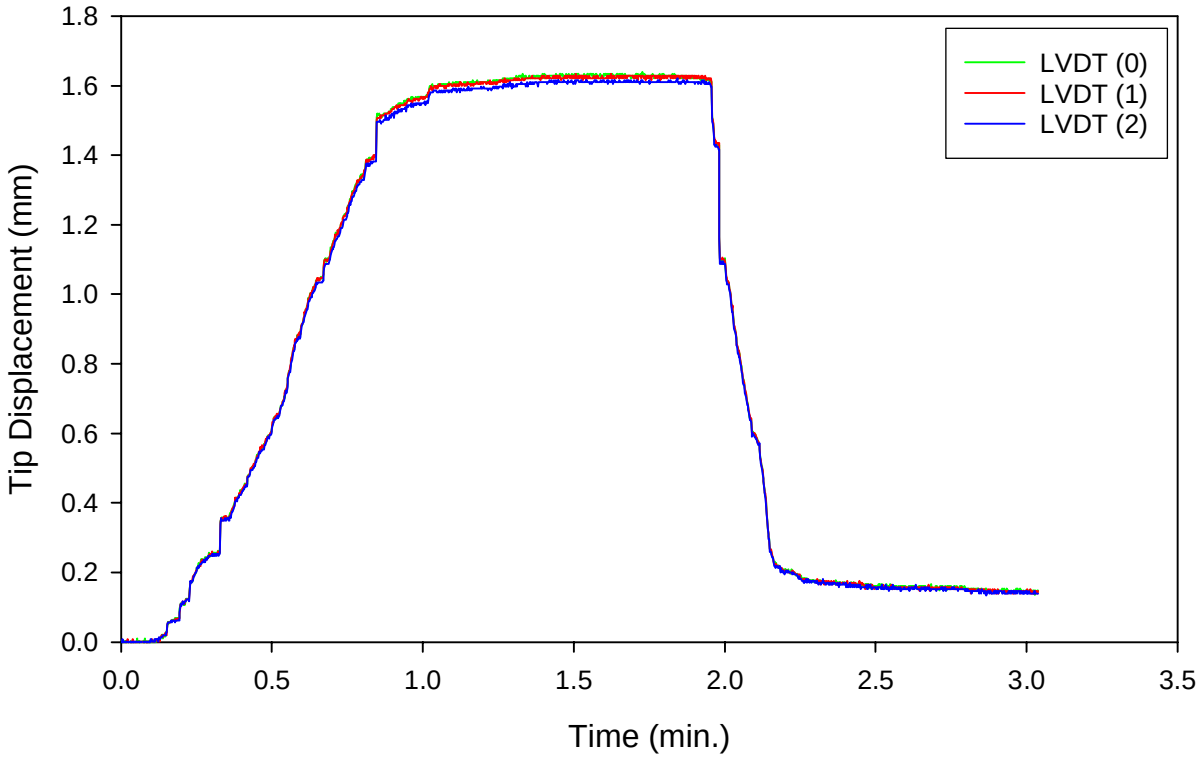

Figure 3.4: Free-edge displacement vs. time for a calibration test (–752 V maximum voltage)

In order to determine the relationship between the free-edge displacement and applied voltage for the cantilevered aluminum plate with the bonded MFC actuator, the maximum displacement for each of the LVDTs was plotted as a function of applied voltage; this relationship is seen in Figure 3.5. Figure 3.5 includes data from all of the voltage cycles discussed above. Because of the displacement difference before and after the voltage was applied in some of the tests, the displacements shown in Figure 3.5 were calculated as the difference between the displacement with the maximum voltage applied and the end displacement when the voltage was zero. It is seen that the displacements obtained from the three LVDTs are again very close to each other, and that the free-edge displacement is, for all intents and purposes, a linear function of applied voltage.

3.2.2 Finite-Element Analysis of the Calibration Experiment

Using *ABAQUS* [37], a finite-element model of the cantilevered aluminum plate with the MFC actuator was created to compare with the calibration experiments. The model used the SR4 two-

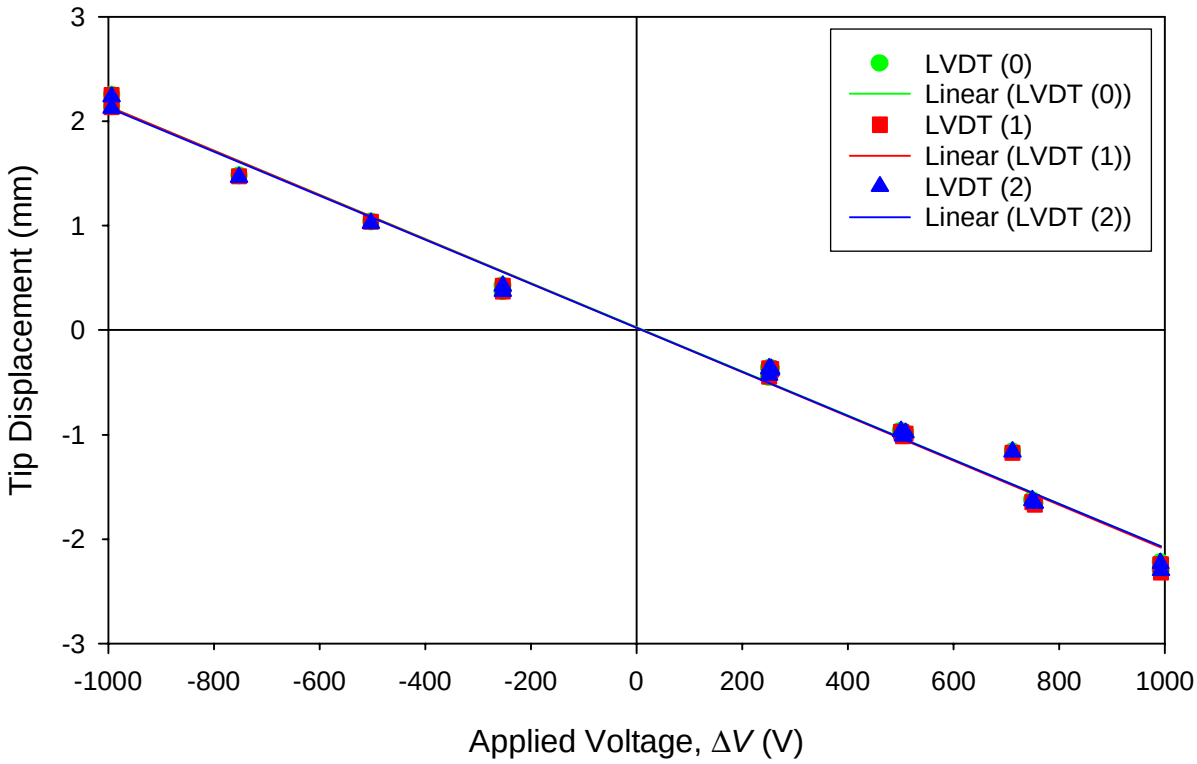

Figure 3.5: Free-edge displacement vs. voltage for calibration experiments

dimensional plate element with the elements arranged as a ten-by-eight element array. The model accounted for the aluminum plate and the active portion of the MFC actuator; the polyimide film outside the active region and the epoxy bond between the MFC actuator and aluminum plate were ignored. The material properties that were used in this model are given in Table 3.1. The MFC actuator material properties were obtained from Wilkie [38].

Table 3.1: Material properties used in finite-element calibration model

Property	Aluminum	MFC Actuator (closed circuit)
E_1 (GPa)	72.4	29
E_2 (GPa)	72.4	18
G_{12} (GPa)	———	5.3
ν_{12}	0.3	0.28

3.2.3 Determination of the Piezoelectric Constants

The piezoelectric constants were determined from the experiment and the *ABAQUS* finite-element model using the influence method. With the influence method, it was assumed that, for given geometry, boundary conditions, and applied voltage, the displacement was only a function of position and the piezoelectric constants, namely,

$$\begin{aligned} w_{\text{LVDT \#1}} &= (a)d_{11}\Delta V + (b)d_{12}\Delta V \\ w_{\text{LVDT \#0,2}} &= (c)d_{11}\Delta V + (d)d_{12}\Delta V \end{aligned} \tag{3.2}$$

where the *w*s are the displacements at the position of the indicated LVDTs (0, 1, or 2), ΔV is the applied voltage, and *a*, *b*, *c*, and *d* are to-be-determined coefficients. To find the values of *a*, *b*, *c*, and *d*, in the *ABAQUS* finite-element model, first $d_{11}\Delta V$ was set to unity and $d_{12}\Delta V$ was set to zero and *a* and *c* were determined. Next, $d_{11}\Delta V$ was set to zero and $d_{12}\Delta V$ was set to unity, and *b* and *d* were determined. From the experiments, as seen in Figure 3.5, the slope of the displacement vs. voltage relationship was known for each LVDT, so equation (3.2), with known values of the *w*s and ΔV, and the calculated values of a, b, c, and d, was used to determine d_{11} and d_{12}. The piezoelectric constants were calculated to be

$$\begin{aligned} d_{11} &= 329\ \mu\varepsilon/\text{kV/mm} \\ d_{12} &= -529\ \mu\varepsilon/\text{kV/mm} \end{aligned} \tag{3.3}$$

The values given by Wilkie et al. [31] were

$$\begin{aligned} d_{11} &= 530\ \mu\varepsilon/\text{kV/mm} \\ d_{12} &= -210\ \mu\varepsilon/\text{kV/mm} \end{aligned} \tag{3.4}$$

It is seen that the value of d_{11} measured here is smaller, but d_{12} is much larger than the value measured by Wilkie et al. [31]. By running the *ABAQUS* model, it was found that the free-edge displacement was insensitive to changes in d_{12}, so d_{12} could be ignored in trying to determine d_{11}. Equation (3.2) then reduces to

$$w_{\text{LVDT \#1}} = (a) d_{11} \Delta V \tag{3.5}$$

Using equation (3.5), d_{11} was found to be

$$d_{11} = 281 \ \mu\varepsilon/\text{kV/mm} \tag{3.6}$$

An estimate of d_{12} was made from this calculated value of d_{11} by using the same d_{11}/d_{12} ratio as Wilkie et al. [31]; d_{12} was then found to be

$$d_{12} = -111 \ \mu\varepsilon/\text{kV/mm} \tag{3.7}$$

With these properties of the actuator determined, the next step in this study was to develop a model of a cross-ply laminate with an MFC actuator bonded to one side. This is a more detailed model than the previously discussed initial model. Because the actuator was to be bonded to the cross-ply *after* the laminate had been fabricated and cooled to room temperature, the more in-depth model had to account for cooling the laminate, bonding the MFC actuator to the laminate, and then applying a voltage to the actuator. Also, the MFC actuator only partially covered the surface of the laminate. This model is the subject of the next chapter.

Chapter 4 In-Depth Modeling of an Unsymmetric Laminate and Actuator

Because the focus of this work moved from using monolithic piezoelectric layers covering the entire laminate to using MFC actuators, the initial model of Chapter 2 had to be revised to include the orthotropy of the MFC actuator and partial coverage of the laminate by the actuator. Also, bonding the MFC actuator to the laminate at room temperature changed the room-temperature curvature of the laminate, as well as the snap-through characteristics. Finally, the curvature changes and snap-through due to the actuation needed to be modeled. A *Mathematica* program was written to implement the details of this new model.

4.1 In-Depth Model Based on the Rayleigh-Ritz Technique

The in-depth model considered the following steps in order: cooling the laminate from the cure temperature, bonding the MFC actuator to the laminate, and then activating the actuator/laminate structure. The particular laminate considered was a $[0°/90°]_T$ graphite-epoxy laminate. The model was, as in Chapter 2, based on the semi-closed form Rayleigh-Ritz technique. Figure 4.1 shows the cross-sectional configuration of the model. The coordinate system was placed at the center of the laminate. The MFC actuator was centered on the laminate with the piezoceramic fibers in the *x* direction. The laminate had side lengths in the *x* and *y* directions of L_x and L_y, respectively, and the MFC actuator had side lengths in the *x* and *y* directions of L_x^{MFC} and L_y^{MFC}, respectively. The model was broken into three sections: *Part I* considered cooling the laminate from the cure temperature to room temperature, *Part II* considered bonding the MFC actuator to the laminate, and *Part III* considered the actuation of the actuator/laminate structure. Although the three parts of the

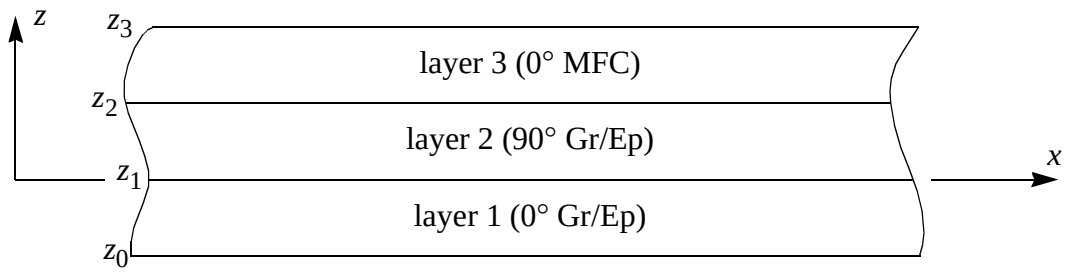

Figure 4.1: Cross-sectional geometry of in-depth model

model consist of sequential steps in the experiments conducted, the model for Part II does not depend on information computed from the solution of Part I. However, as developed here, Part III of the model does use information computed from the solution to Part II. As will be seen, in Parts II and III, terms are added to the total potential energy of the cooled laminate.

4.1.1 Part I: Laminate Cooling

The first step, Part I, of this model was to consider the initial cooled shape of the $[0°/90°]_T$ graphite-epoxy laminate. A Rayleigh-Ritz model, much like that of Chapter 2, was created to model the cooling of the graphite-epoxy laminate. Because this part did not consider the MFC actuator, only thermal effects were considered in determining the effective force and moment resultants.

The equation for the total potential energy of the cooled laminate, Π_1, is given by

$$\Pi_1 = \frac{1}{2}\int_{-\frac{L_x}{2}}^{\frac{L_x}{2}}\int_{-\frac{L_y}{2}}^{\frac{L_y}{2}}\int_{z_0}^{z_2}[(\sigma_x - \sigma_x^T)\varepsilon_x + (\sigma_y - \sigma_y^T)\varepsilon_y + (\sigma_{xy} - \sigma_{xy}^T)\gamma_{xy}]\,dx\,dy\,dz \tag{4.1}$$

where the σs are the stresses, the σ^Ts are the thermally-induced stresses, and the εs and γ_{xy} are the strains in the laminate. In equation (4.1), if the integration with respect to *z* is carried out, an equation similar to equation (2.12) is obtained. The stresses are given by

$$\begin{aligned}
\sigma_x &= \overline{Q}_{11}\varepsilon_x + \overline{Q}_{12}\varepsilon_y + \overline{Q}_{16}\gamma_{xy} - \sigma_x^T \\
\sigma_y &= \overline{Q}_{12}\varepsilon_x + \overline{Q}_{22}\varepsilon_y + \overline{Q}_{26}\gamma_{xy} - \sigma_y^T \\
\sigma_{xy} &= \overline{Q}_{16}\varepsilon_x + \overline{Q}_{26}\varepsilon_y + \overline{Q}_{66}\gamma_{xy} - \sigma_{xy}^T
\end{aligned} \tag{4.2}$$

where the $\overline{Q}$s are the transformed reduced stiffnesses of the laminate and

$$\begin{aligned}
\sigma_x^T &= \overline{Q}_{11}\varepsilon_x^T + \overline{Q}_{12}\varepsilon_y^T + \overline{Q}_{16}\gamma_{xy}^T \\
\sigma_y^T &= \overline{Q}_{12}\varepsilon_x^T + \overline{Q}_{22}\varepsilon_y^T + \overline{Q}_{26}\gamma_{xy}^T \\
\sigma_{xy}^T &= \overline{Q}_{16}\varepsilon_x^T + \overline{Q}_{26}\varepsilon_y^T + \overline{Q}_{66}\gamma_{xy}^T
\end{aligned} \tag{4.3}$$

As in Chapter 2,

$$\begin{aligned}
\varepsilon_x^T &= \alpha_x \Delta T \\
\varepsilon_y^T &= \alpha_y \Delta T \\
\gamma_{xy}^T &= \alpha_{xy} \Delta T
\end{aligned} \tag{4.4}$$

and the midplane strains are given by the simplified nonlinear strain-displacement relations for small strains and moderate rotations as

$$\begin{aligned}
\varepsilon_x^\circ &= \frac{\partial u^\circ}{\partial x} + \frac{1}{2}\left(\frac{\partial w^\circ}{\partial x}\right)^2 \\
\varepsilon_y^\circ &= \frac{\partial v^\circ}{\partial y} + \frac{1}{2}\left(\frac{\partial w^\circ}{\partial y}\right)^2 \\
\gamma_{xy}^\circ &= \frac{\partial u^\circ}{\partial y} + \frac{\partial v^\circ}{\partial x} + \left(\frac{\partial w^\circ}{\partial x}\right)\left(\frac{\partial w^\circ}{\partial y}\right)
\end{aligned} \tag{4.5}$$

The midplane curvatures are given by

$$\begin{aligned} \kappa_x^\circ &= -\frac{\partial^2 w^\circ}{\partial x^2} \\ \kappa_y^\circ &= -\frac{\partial^2 w^\circ}{\partial y^2} \\ \kappa_{xy}^\circ &= -2\frac{\partial^2 w^\circ}{\partial x \partial y} \end{aligned} \tag{4.6}$$

so the strains in the laminate are taken to be

$$\begin{aligned} \varepsilon_x &= \varepsilon_x^\circ + z\kappa_x^\circ \\ \varepsilon_y &= \varepsilon_y^\circ + z\kappa_y^\circ \\ \gamma_{xy} &= \gamma_{xy}^\circ + z\kappa_{xy}^\circ \end{aligned} \tag{4.7}$$

The assumed displacement fields of Chapter 2, equation (2.13), are again used, namely

$$\begin{aligned} u^\circ &= c_3 x - \frac{c_1^2 x^3}{6} - \frac{c_1 c_2 x y^2}{4} \\ v^\circ &= c_4 y - \frac{c_2^2 y^3}{6} - \frac{c_1 c_2 x^2 y}{4} \\ w^\circ &= \frac{1}{2}(c_1 x^2 + c_2 y^2) \end{aligned} \tag{4.8}$$

From equations (4.8), (4.6), and (4.5), the midplane strains and curvatures of the laminate are given by

$$\begin{aligned}
\varepsilon_x^\circ &= c_3 - \frac{c_1 c_2 y^2}{4} \\
\varepsilon_y^\circ &= c_4 - \frac{c_1 c_2 x^2}{4} \\
\gamma_{xy}^\circ &= 0 \\
\kappa_x^\circ &= -c_1 \\
\kappa_y^\circ &= -c_2 \\
\kappa_{xy}^\circ &= 0
\end{aligned} \tag{4.9}$$

Once all the integrations of equation (4.1) are carried out, Π_1, is reduced to an algebraic equation in terms of c_1, c_2, c_3, and c_4 and, as in equation (2.16), the determination of the stationary solutions of Π_1 is reduced to solving the following series of simultaneous equations for $c_1 - c_4$:

$$\frac{\partial \Pi_1}{\partial c_1} = 0 \qquad \frac{\partial \Pi_1}{\partial c_2} = 0 \qquad \frac{\partial \Pi_1}{\partial c_3} = 0 \qquad \frac{\partial \Pi_1}{\partial c_4} = 0 \tag{4.10}$$

and then checking the second variation of the total potential energy for stability, as in equation (2.17).

For the purpose of illustration, typical as-cooled room-temperature shapes are shown in Figure 4.2. These shapes are similar to those that were seen in Figure 2.2 in that there are two stable cylindrical shapes and one unstable saddle shape. In Figure 4.2, the saddle is very shallow, appearing almost flat.

4.1.2 Part II: Bonding the MFC Actuator to the Laminate

Part II of the model considered bonding of the MFC actuator to the laminate substrate. The exper-

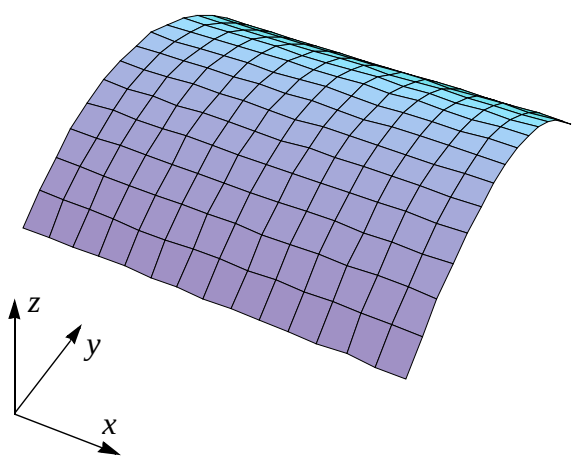

(a) - a stable cylindrical shape

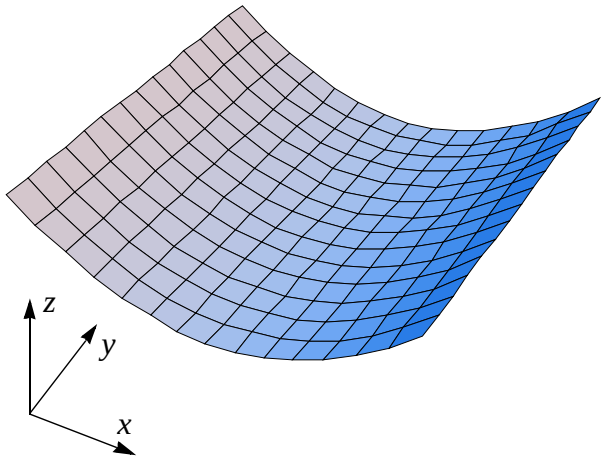

(b) - the other stable cylindrical shape

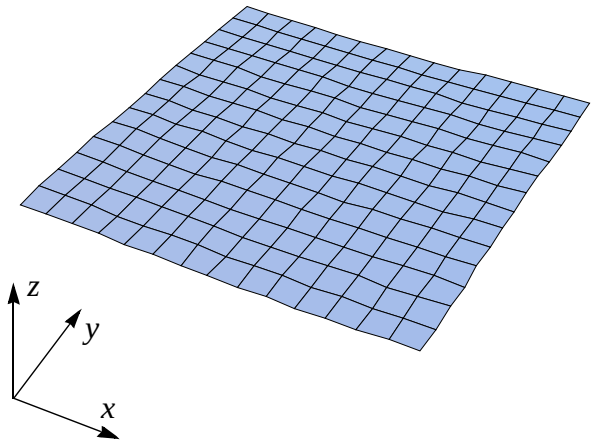

(c) - the unstable saddle shape

Figure 4.2: As-cooled room-temperature shapes

imental method of bonding the MFC actuator to the laminate would be to place the laminate and actuator with adhesive into a vacuum bag and, using a vacuum pump, evacuate the bag to pull the laminate and the actuator into contact until the adhesive cures. Since the MFC actuator was initially flat, the vacuum deformed it to bring it into contact with the curved laminate; however, since the cylindrical laminate was also in the vacuum bag, the curvature of the laminate was also changed, specifically, it was reduced slightly. The result was that the contacting surfaces of the actuator and the laminate developed the same curvature. At the outset, this curvature is unknown, but it is the starting configuration for activating the actuator and snapping the laminate to the other cylindrical configuration, and therefore it is important that the *actuator-added* shape charac-

teristics of the laminate be known. Part II of the model was created to simulate this vacuum bonding technique, namely, to simulate the actuator and laminate conforming so that both the actuator and laminate had the same curvatures. This part also relied on the Rayleigh-Ritz technique.

The total potential energy of the laminate with the MFC actuator bonded to the laminate will be the sum of Π_1 from equation (4.1) and the total potential energy of the actuator, Π_2, which is given as

$$\Pi_2 = \frac{1}{2}\int_{-\frac{L_x^{MFC}}{2}}^{\frac{L_x^{MFC}}{2}}\int_{-\frac{L_y^{MFC}}{2}}^{\frac{L_y^{MFC}}{2}}\int_{z_2}^{z_3}[\sigma_x^a\varepsilon_x^a + \sigma_y^a\varepsilon_y^a + \sigma_{xy}^a\gamma_{xy}^a]\mathrm{d}x\mathrm{d}y\mathrm{d}z \tag{4.11}$$

where σ_x^a, σ_y^a, and σ_{xy}^a and ε_x^a, ε_y^a, and γ_{xy}^a are the stresses and strains in the MFC actuator due to the bonding process. Recall from Figure 4.1 that z_2 and z_3 define the thickness of the actuator. The stresses created in the actuator due to the bonding process will be due just to the actuator being bent to the same curvature as the laminate; because, until the adhesive begins to cure, the actuator can slip relative to the laminate and the midplane strains in the actuator will be zero. The stress-strain relations for the bonded actuator are

$$\begin{aligned}
\sigma_x^a &= \overline{Q}_{11}\varepsilon_x^a + \overline{Q}_{12}\varepsilon_y^a + \overline{Q}_{16}\gamma_{xy}^a \\
\sigma_y^a &= \overline{Q}_{12}\varepsilon_x^a + \overline{Q}_{22}\varepsilon_y^a + \overline{Q}_{26}\gamma_{xy}^a \\
\sigma_{xy}^a &= \overline{Q}_{16}\varepsilon_x^a + \overline{Q}_{26}\varepsilon_y^a + \overline{Q}_{66}\gamma_{xy}^a
\end{aligned} \tag{4.12}$$

where the $\overline{Q}$s are the transformed reduced stiffnesses of the actuator. For simplification, it is assumed that the curvatures of the midplane of the laminate and the actuator are the same, rather than the curvatures of the contacting surfaces. The strains may then be approximated as

$$\begin{aligned} \varepsilon_x^a &= \left(z - \left(\frac{z_3 - z_0}{2}\right)\right)\kappa_x^\circ \\ \varepsilon_y^a &= \left(z - \left(\frac{z_3 - z_0}{2}\right)\right)\kappa_y^\circ \\ \gamma_{xy}^a &= \left(z - \left(\frac{z_3 - z_0}{2}\right)\right)\kappa_{xy}^\circ = 0 \end{aligned} \tag{4.13}$$

where κ_x° and κ_y° are unknowns, but will be the same in the actuator and the laminate. The displacement fields of equation (4.8) are again assumed to be valid, with $c_1 - c_4$ being unknown and different from the case of Part I, i.e., different from just cooling the laminate from the cure temperature.

For Part II, the total potential energy of the actuator/laminate structure, Π, is given as

$$\Pi = \Pi_1 + \Pi_2 \tag{4.14}$$

When the integrations embedded in equation (4.14) are carried out, the minimization of Π is reduced to solving a system of simultaneous algebraic equations for c_1, c_2, c_3, and c_4, and checking for stability.

As an example of how the curvatures change during the bonding of the actuator, consider the cooled shape seen in Figure 4.2a. If an MFC actuator, like the ones used in this study, with the piezoceramic fibers in the x direction, is bonded to the top-side of this laminate, the κ_y° curvature in the actuator-added configuration is changed by about 14%.

4.1.3 Part III: Actuation of the Actuator/Laminate Structure

Part III of the model considered the actuation of the bonded actuator/laminate structure. Because

the laminate had two stable cylindrical equilibrium shapes, the actuator could be bonded to the laminate while the laminate was in either of two different cylindrical configurations; this was automatically accounted for in the bonding portion, Part II, of the model because two stable equilibrium shapes were obtained. However, because the actuator could not slip on the laminate once bonding was complete, the actuator-added configuration of the laminate (one of the two stable shapes resulting from the analysis of Part II) was the *initial* configuration for Part III and was specified by the coefficients, c_1, c_2, c_3, and c_4 of the actuator-added configuration; these actuator-added coefficients were renamed c_1^i, c_2^i, c_3^i, and c_4^i, respectively, for Part III. The total potential energy of the model was again broken into the laminate contribution, again Π_1, and the actuator contribution, called Π_3. The actuator contribution, Π_3, is more complicated than was Π_2 in Part II of the model. Because the strain in the actuator during Part II was due only to bending, in Part III additional terms need to be added to the actuator strains of equation (4.13). The contribution to the total potential energy from the MFC actuator in Part III can be written as

$$\Pi_3 = \frac{1}{2}\int_{-\frac{L_x^{MFC}}{2}}^{\frac{L_x^{MFC}}{2}}\int_{-\frac{L_y^{MFC}}{2}}^{\frac{L_y^{MFC}}{2}}\int_{z_2}^{z_3}[(\sigma_x^a - \sigma_x^{Es})\varepsilon_x + (\sigma_y^a - \sigma_y^{Es})\varepsilon_y + (\sigma_{xy}^a - \sigma_{xy}^{Es})\gamma_{xy}]\,dx\,dy\,dz \tag{4.15}$$

where the εs and γ_{xy} are the strains in the actuator and are defined the same in the actuator and the laminate, by equation (4.7); the reference surface remains the midsurface of the laminate. The σ^as are the stresses in the actuator and are given by

$$\begin{aligned}
\sigma_x^a &= \bar{Q}_{11}\varepsilon_x + \bar{Q}_{12}\varepsilon_y + \bar{Q}_{16}\gamma_{xy} - \sigma_x^{Es} \\
\sigma_y^a &= \bar{Q}_{12}\varepsilon_x + \bar{Q}_{22}\varepsilon_y + \bar{Q}_{26}\gamma_{xy} - \sigma_y^{Es} \\
\sigma_{xy}^a &= \bar{Q}_{16}\varepsilon_x + \bar{Q}_{26}\varepsilon_y + \bar{Q}_{66}\gamma_{xy} - \sigma_{xy}^{Es}
\end{aligned} \tag{4.16}$$

where the $\overline{Q}$s are the transformed reduced stiffnesses of the actuator. The σ^{Es}s are induced stresses that take into account stresses from bonding the MFC actuator to the laminate (i.e., forcing the actuator to conform to the laminate and the fact that the actuator is now bonded, without slipping, to the laminate) and the piezoelectrically-induced stresses due to actuation, and are given by

$$\begin{aligned}
\sigma_x^{Es} &= \overline{Q}_{11}(\varepsilon_x^E + \varepsilon_x^s) + \overline{Q}_{12}(\varepsilon_y^E + \varepsilon_y^s) + \overline{Q}_{16}(\gamma_{xy}^E + \gamma_{xy}^s) \\
\sigma_y^{Es} &= \overline{Q}_{12}(\varepsilon_x^E + \varepsilon_x^s) + \overline{Q}_{22}(\varepsilon_y^E + \varepsilon_y^s) + \overline{Q}_{26}(\gamma_{xy}^E + \gamma_{xy}^s) \\
\sigma_{xy}^{Es} &= \overline{Q}_{16}(\varepsilon_x^E + \varepsilon_x^s) + \overline{Q}_{26}(\varepsilon_y^E + \varepsilon_y^s) + \overline{Q}_{66}(\gamma_{xy}^E + \gamma_{xy}^s)
\end{aligned} \tag{4.17}$$

where the ε^Es and γ_{xy}^E are the piezoelectrically-induced strains, and are given by equations (3.1) and (2.11). The ε^ss and γ_{xy}^s, which may be called *shift strains*, are formulated for the midsurface of the actuator. These shift strains are needed to account for the strains in the actuator due to the bonding process so that the strains and curvatures of the reference surface, i.e., $c_1 - c_4$, may be used in finding the extrema of the total potential energy of the entire actuator/laminate structure. Finding these extrema will give all of the equilibrium shapes (either one or three equilibrium shapes, depending on applied voltage) of the bonded actuator/laminate structure, whether or not there is voltage applied to the actuator; recall that in Part II, only actuator-added configurations were found. In reality, as is seen in Figure 4.3a, because there are only bending strains in the actuator in the actuator-added configuration, the strain distributions through the thickness of the laminate and actuator are not continuous. In addition, it is assumed here, in the spirit of the Kirchhoff hypothesis, that the *strain increment*, i.e., piezoelectrically-induced strains, due to the application of the voltage to the actuator are continuous, as shown in Figure 4.3b. Thus the total strain in the laminate and the actuator will be the sum of the strains shown in Figures 4.3a and 4.3b. As a result, whether voltage is applied or not, the profile of strain through the laminate and actuator is discontinuous, as in Figure 4.3c. To account for this discontinuity, yet have one set of variables, i.e., $c_1 - c_4$, to define the strains within the laminate *and* the actuator, the shift of strain measures

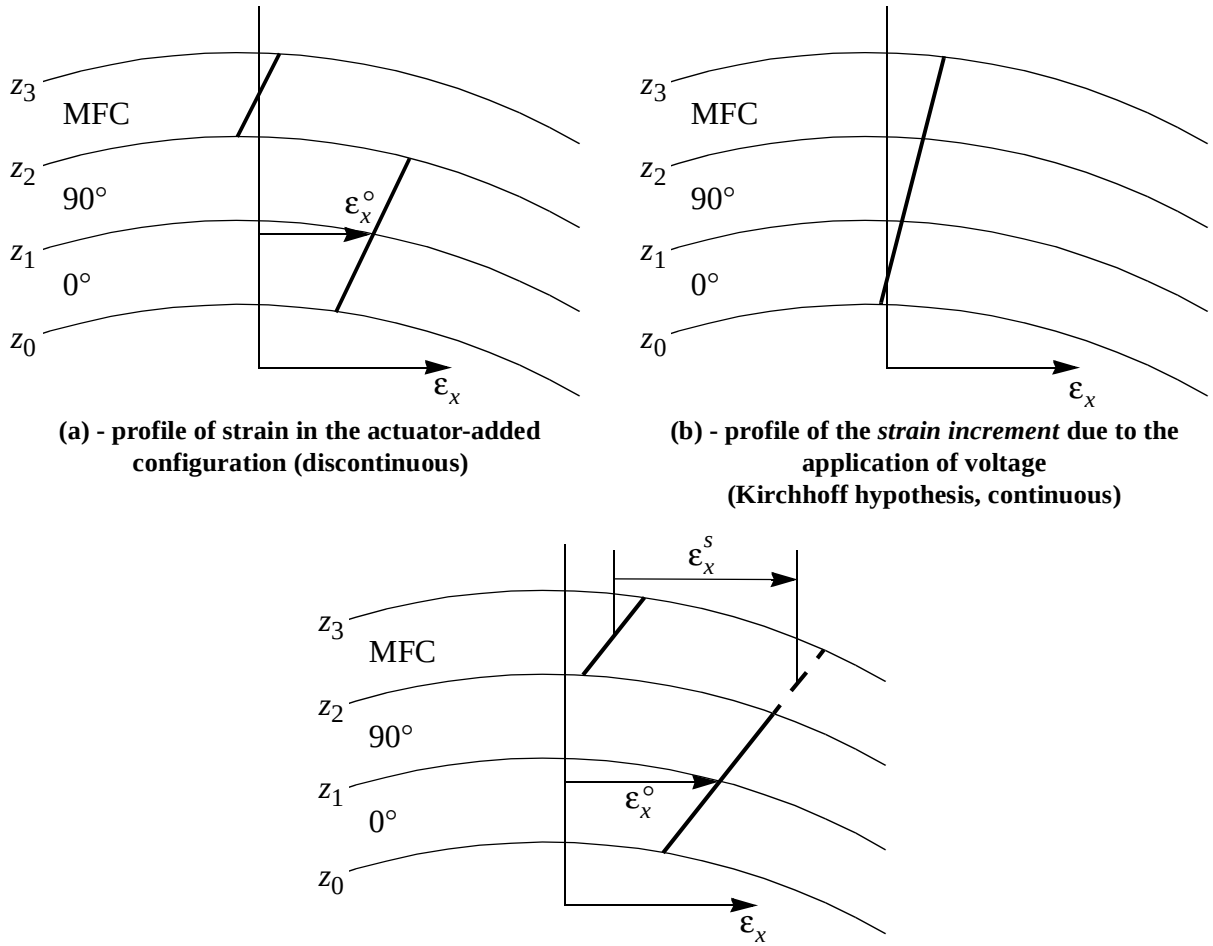

(a) - profile of strain in the actuator-added configuration (discontinuous)

(b) - profile of the *strain increment* due to the application of voltage (Kirchhoff hypothesis, continuous)

(c) - profile of the strain with the application of voltage (discontinuous)

Figure 4.3: Strain through the thickness of the laminate and actuator for Part III

is necessary. In Figure 4.3c, the solid lines represent the actual strain, while the combination of the solid line in the laminate and the dashed line in the actuator represent the linear and continuous strain field that is represented by $c_1 - c_4$. The shift strains are thus given by

$$\begin{aligned} \varepsilon_x^s &= \varepsilon_x^{i\circ} + \left(\frac{z_3 - z_0}{2}\right)\kappa_x^{i\circ} \\ \varepsilon_y^s &= \varepsilon_y^{i\circ} + \left(\frac{z_3 - z_0}{2}\right)\kappa_y^{i\circ} \\ \gamma_{xy}^s &= \gamma_{xy}^{i\circ} + \left(\frac{z_3 - z_0}{2}\right)\kappa_{xy}^{i\circ} = 0 \end{aligned} \tag{4.18}$$

where the $\varepsilon^{i\circ}$ s and $\gamma_{xy}^{i\circ}$ are the initial strains and the $\kappa^{i\circ}$ s are the initial curvatures, i.e., the strains and curvatures in the actuator-added configuration, at the midplane of the composite. Note that the shift strains are not dependent upon the applied voltage. The initial strains and curvatures are known, and are given by (from equation (4.9))

$$\begin{aligned}
\varepsilon_x^{i\circ} &= c_3^i - \frac{c_1^i c_2^i y^2}{4} \\
\varepsilon_y^{i\circ} &= c_4^i - \frac{c_1^i c_2^i x^2}{4} \\
\gamma_{xy}^{i\circ} &= 0 \\
\kappa_x^{i\circ} &= -c_1^i \\
\kappa_y^{i\circ} &= -c_2^i \\
\kappa_{xy}^{i\circ} &= 0
\end{aligned} \tag{4.19}$$

The total potential energy for the actuation portion of the model, Part III, is given as

$$\Pi = \Pi_1 + \Pi_3 \tag{4.20}$$

The total potential energy is minimized to solve for the undetermined coefficients, c_1, c_2, c_3, and c_4 and, therefore, for the actuated shape(s) of the actuator/laminate structure. For a given set of geometric and material properties and other parameters, curves similar to those of Figure 2.3 can be created.

4.2 Description of the Use of the In-Depth Model to Design Experiment

Parameters such as laminate thickness, laminate size and shape, laminate material properties,

actuator geometry, and actuator properties were varied in order to determine a laminate and actuator combination that would have a reasonable chance of snapping from one configuration to another with the available power supply (±1000 V); the piezoelectric constants of the actuator were assumed to be those given by equations (3.6) and (3.7). The use of the model to design a such a laminate and actuator combination is discussed in the next chapter.

Chapter 5 Experimental Work to Examine Snap Through

A $[0°/90°]_T$ graphite-epoxy laminate was manufactured in order to support the predictions of the developed models. Specifically, the experimental work would be compared with the model predictions for the laminate and actuator/laminate shapes, and with the predictions for the snap-through voltage. This square laminate, with side lengths of 300 mm, was manufactured in a press-clave using AS4/3502 graphite-epoxy prepreg following the manufacturer's recommended cure cycle with a cure temperature of 177 °C, giving a ΔT of −157 °C; later this laminate would have an MFC actuator bonded to it.

5.1 Use of the In-Depth Model to Design Experiment

With the laminate constructed, measurements could be made to determine the laminate thickness: the total thickness was 0.273 mm, so it was assumed that the layer thickness was 0.136 mm. The assumed material properties for the AS4/3502 and also for the MFC actuator are given in Table 5.1. The properties for AS4/3502 have, in the past, been used successfully to model the response of AS4/3502 laminates. The MFC properties were a combination of those given by Wilkie [38] and the measured piezoelectric constants discussed in Chapter 3.

5.1.1 Checking Room-Temperature Shape of Uncut Laminate

The first step taken was to compare the room-temperature shape of the 300 mm by 300 mm $[0°/90°]_T$ laminate with the predicted shape of this laminate. The major diameter of curvature of the laminate was measured, using a ruler, to be 156 mm in one of the stable cylindrical config-

Table 5.1: AS4/3502 and MFC actuator material properties

AS4/3502		MFC Actuator	
Property	**Value**	**Property**	**Value**
E_1 (GPa)	130.0	E_1 (GPa)	29
E_2 (GPa)	9.701	E_2 (GPa)	18
G_{12} (GPa)	5.000	G_{12} (GPa)	5.3
ν_{12}	0.3	ν_{12}	0.28
α_1 (1/°C)	-0.018×10^{-6}	d_{11} (με/kV/mm)	281
α_2 (1/°C)	24.282×10^{-6}	d_{12} (με/kV/mm)	−111

urations and 162 mm in the other cylindrical configuration. These diameters of curvature correspond with curvatures of

$$\kappa^{\circ} = 12.8 \text{ m}^{-1} \quad \text{and} \quad \kappa^{\circ} = 12.3 \text{ m}^{-1} \tag{5.1}$$

(Note: There are no subscripts on the curvatures in equation 5.1 because at this point in the experiments, the coordinate system for the laminate had not yet been established.) Using Part I of the in-depth model and a change of temperature from the cure temperature to room temperature of −157 °C, the major curvature of the cylindrical shapes is calculated to be 11.7 m^{-1}, which is within 10% of the measured value.

Over the course of about four months, the curvature in the panel relaxed. Rather than using a ruler to measure the curvature directly from the laminate, the curvatures were measured by tracing the curved shapes of the laminate onto paper (see Figure 5.1) and the height, *h*, and secant, 2*d*, of the arc were measured. The curvatures were then calculated using a geometric argument: assuming that the arc is a circular arc, the radius of curvature, *R*, and the curvature, κ°, can be found as

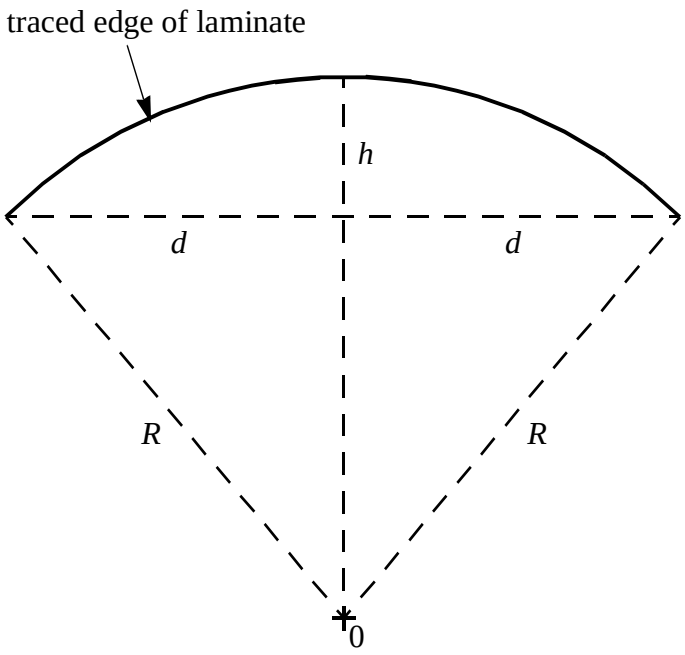

$$R = \frac{\sin\left(\text{Arctan}\left(\frac{d}{h}\right)\right)\sqrt{d^2 + h^2}}{\sin\left(\pi - 2\ \text{Arctan}\left(\frac{d}{h}\right)\right)} \qquad (5.2)$$

$$\kappa^\circ = \frac{1}{R}$$

Figure 5.1: Diagram for the experimental measurement of curvature

shown, by equation (5.2). Using this process, the relaxed major curvatures in the two equilibrium configurations were measured to be

$$\begin{aligned} \kappa_x^\circ &= -5.37\ \text{m}^{-1} \\ \kappa_y^\circ &= 4.34\ \text{m}^{-1} \end{aligned} \qquad (5.3)$$

where the coordinate system used is that of Figure 4.2. It was speculated that this relaxation was caused by moisture absorption of the laminate. The laminate was placed in an oven at 50 °C in an effort to drive this moisture out of the laminate. After 24 hours in the oven, the laminate was snapped to the other equilibrium configuration and returned to the oven for an additional 24 hours. After the laminate was removed from the oven and cooled, the major laminate curvatures in the two equilibrium configurations were found to be

$$\kappa_x^\circ = -10.3 \text{ m}^{-1}$$
$$\kappa_y^\circ = 9.36 \text{ m}^{-1} \tag{5.4}$$

Heating the laminate allowed it to recover most of the original curvature. Because moisture and temperature effects may be modeled in the same manner, ΔT in the model was decreased from -157 °C to -131 °C in order to produce curvatures similar to those measured when the laminate was removed from the oven; the model predicts curvatures of 9.8 m^{-1} with this temperature change.

5.1.2 Modeling Snap Through of the Actuator/Laminate Structure

The material properties given in Table 5.1 and the ΔT of -131 °C, which was discussed above, were used as input data for the actuator/laminate model using laminate side length as a variable parameter. It was assumed, as in Chapter 4, that the MFC actuator would be bonded to the top side of the laminate with the piezoelectric fibers in the x direction to form a $[0°/90°/0°_{\text{MFC}}]_{\text{T}}$ structure. The idea was to find a side length (keeping the laminate square) for which the laminate could be snapped by applying a voltage (1000 V or less) to the MFC actuator. Such a laminate was indeed found and was to be the basis for the experimental verification. The laminate decided upon would have the MFC actuator bonded to it while the laminate was in a configuration similar to the one in Figure 4.2a, a configuration with the major curvature being positive κ_y°. The side length decided upon was 0.152 m; the laminate was cut to this size. Figure 5.2 shows the predicted curvatures of the actuator/laminate structure as a function of the voltage applied to the MFC actuator for voltages from -1000 V to $+1000$ V. Figure 5.2 is analogous to Figure 2.3, but as can be seen, there are differences. Figure 5.3 shows the w° displacement of the actuator/laminate structure for selected voltages. At the zero voltage condition, there are two stable equilibrium shapes: one with considerable curvature in the y direction and little curvature in the x direction (Figure 5.3a), and the other, much flatter, but with the major curvature in the x direction (Figure 5.3b). Unlike the situation in Figures 2.3 and 2.2, the curvatures for the room-temperature shapes are not equal and

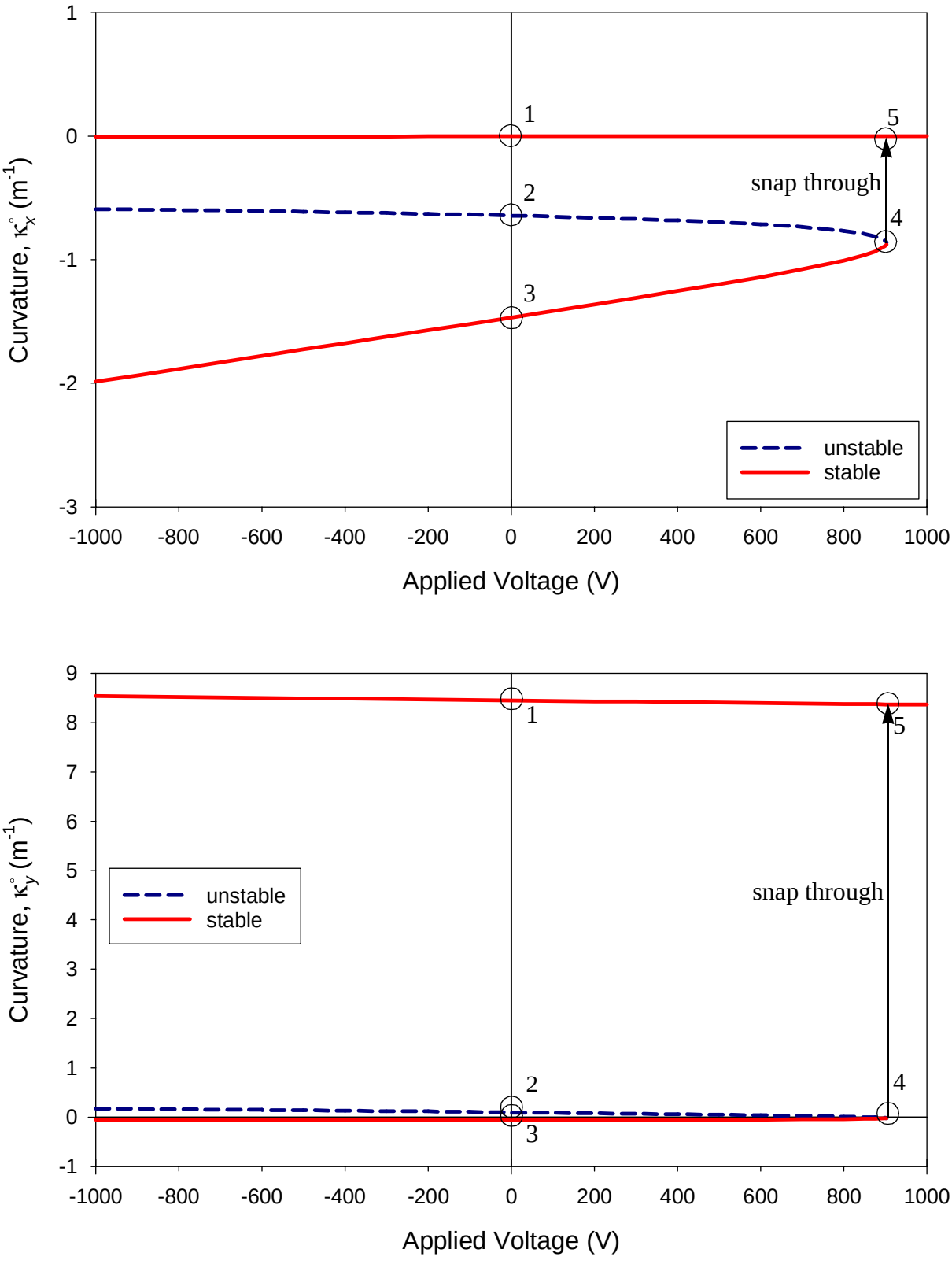

Figure 5.2: Curvatures vs. applied voltage for the actuator/laminate structure

opposite because the MFC actuator was added to only one side of the laminate; adding the MFC actuator to just one side biases the curvatures of the room-temperature shapes. Also, the MFC actuator has orthotropic material properties, so, compared to the isotropic monolithic layers assumed when computing the results of Figures 2.2 and 2.3, there are directional effects with the MFC actuator which translate into curvature effects for the actuator/laminate structure.

Referring to Figures 5.2 and 5.3, if the actuator/laminate structure begins in the configuration given by the lower branch of Figure 5.2, in position 3, as shown in Figure 5.3b, and the voltage is

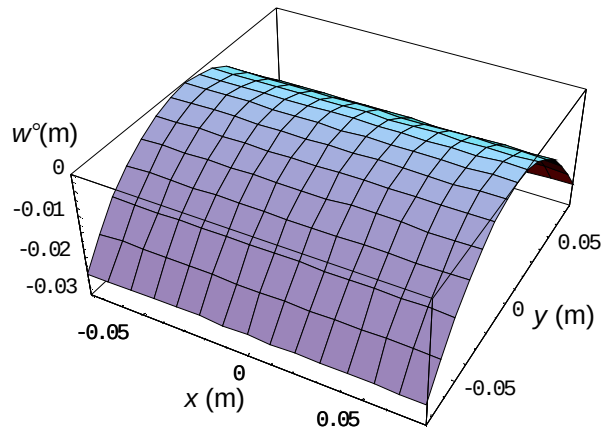

point 1
(a) - a stable cylindrical shape at 0 V

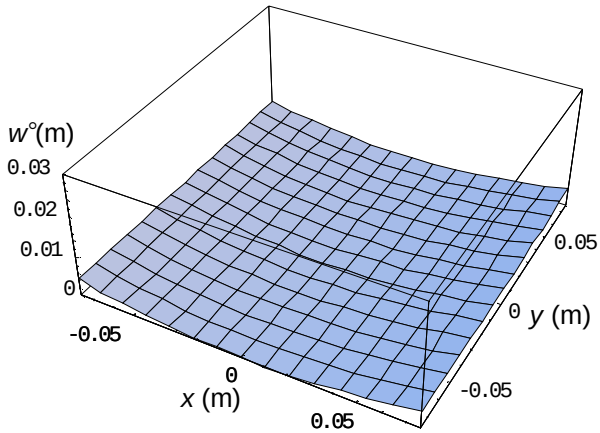

point 3
(b) - the other stable cylindrical shape at 0 V

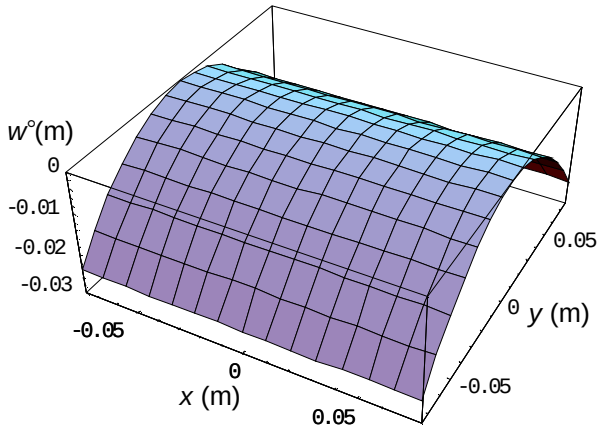

point 5
(c) - the only stable shape at 904 V

Figure 5.3: Unactuated and actuated shapes of the actuator/laminate structure

increased, the structure changes curvatures along the path from point 3 to point 4. The structure is predicted to snap to the upper branch when the voltage reaches +904 V, i.e., from point 4 to point 5. Using reasonable voltages, it is not possible to effect snap through of this laminate combination using negative voltages; this is seen by the disconnected top and middle branches at −1000 V in Figure 5.2.

It is worth noting at this point that the discussion has come full circle to some degree. In Chapter 2, it was shown with an idealized model that the concept proposed for the morphing of structures works. Here, in Chapter 5, considering many of the practical considerations, it is again shown that the concept will work. There remains the task of experimentally verifying the predictions. This is the subject of the following sections of this chapter.

5.2 Actuator/Laminate Structure Assembly

The $[0°/90°]_T$ laminate was cut to have a side length of 0.152 m. But before experiments could be run, several steps still needed to be completed. The first step was to bond a single strain gage to the laminate. The single strain gage would allow precise measurement of the snapping voltage; it was bonded such that it read strain in the *y* direction, the direction perpendicular to the main actuation direction of the actuator. The next step was to again measure the curvatures of the laminate to see if relaxation of the laminate again occurred. The final step was to bond the actuator to the laminate.

5.2.1 Checking Room-Temperature Shape of Cut Laminate

As with the laminate while still uncut (discussed in Section 5.1.1), once cut to 0.152 m per side, the laminate again lost curvature, this time over the course of about one month. Again, to force out any moisture, the laminate was put into an oven set to 50 °C; the laminate was snapped to the other cylindrical configuration after 23 hours and put back into the oven for another 20 hours. Upon removal from the oven, the laminate was placed into a desiccator. Later that same day, the

laminate was removed from the desiccator, the major curvatures of the laminate were measured, and the actuator was bonded to the laminate. The major curvatures in the two configurations just prior to bonding the actuator were found to be (considering the coordinate system of, and shapes similar to, Figures 4.2a and b)

$$\begin{aligned} \kappa_x^\circ &= -9.46 \text{ m}^{-1} \\ \kappa_y^\circ &= 8.63 \text{ m}^{-1} \end{aligned} \tag{5.5}$$

5.2.2 Bonding the MFC Actuator to the Laminate

The MFC actuator was bonded to the laminate using Epotek 301 low-viscosity, two-part epoxy. The laminate, in the configuration with the major curvature being positive κ_y°, like Figure 4.2a, was placed so that the major curvature was concave down and the actuator was centered on top of the laminate and placed such that the piezoceramic fibers were in the *x* direction. The surfaces of the laminate and the actuator were prepared for the epoxy, the epoxy was mixed and spread on the laminate, and the actuator was carefully centered and taped to the laminate. The laminate and actuator were then placed into a vacuum bag. The vacuum bag was sealed and a vacuum was drawn. The vacuum forced the laminate and actuator into contact; the vacuum was applied for 48 hours, until the epoxy was cured. The actuator/laminate structure, a $[0°/90°/0°_{\text{MFC}}]_{\text{T}}$ structure, was removed from the vacuum bag, and the curvature in this configuration, the actuator-added configuration, was traced as in Section 5.1.1. (The curvature in the second configuration was recorded later when it was first snapped in preparation for running the first experiment with applied voltage.) The actuator/laminate structure was placed in the desiccator until it was ready to be used.

5.3 Experiments to Study the Snap-Through Behavior of the Actuator/Laminate Structure

5.3.1 Equipment for Experiment

The experimental setup to verify the predictions developed consisted of a voltage supply, voltage amplifier, strain gage amplifier/conditioner, voltmeter, LabVIEW data acquisition system on a personal computer, and the actuator/laminate structure. The voltage supply, which output voltage from 0 V to 20 V, was used as an input to the voltage amplifier. The voltage amplifier, which was not available previously, was a 1:1000 amplifier with a maximum voltage output of 4000 V. The strain gage amplifier/conditioner was used to balance and calibrate the strain gage, and to output strain to the data acquisition system. Inputs to the LabVIEW data acquisition system were strain from the strain gage and a monitor voltage from the amplifier, which allowed measurement of the voltage output of the amplifier. The voltage output from the amplifier was connected to the leads of the MFC actuator; as the voltage was varied, the strain and voltage were measured. When the actuator/laminate structure snapped from one configuration to another, a large jump in the strain was seen.

5.3.2 Experiments

Figure 5.4 shows pictures of the actuator/laminate structure in both stable configurations; the picture on the left shows the actuator/laminate structure in the actuator-added configuration. The picture on the right, Figure 5.4b, shows the *second* stable configuration. Viewed from a slightly different perspective, these shapes correspond to the predicted shapes illustrate in Figures 5.3a and 5.3b, respectively.

The experimental equipment was set up and the actuator/laminate structure was carefully snapped from the actuator-added configuration to the second configuration, the configuration of Figure 5.4b, by hand. With the actuator/laminate structure in the second configuration, and while recording the data, the voltage was slowly increased and the laminate was monitored for any snapping

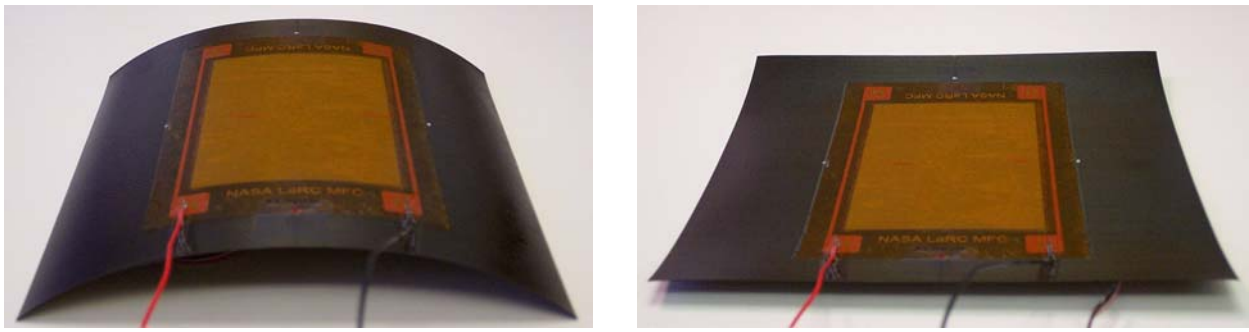

(a) - actuator-added configuration **(b) - second configuration**

Figure 5.4: Experimental stable shapes of actuator/laminate structure with no applied voltage

events.

For each run of the experiments, the laminate was placed in one of three positions; these positions translate to three sets of boundary conditions. These positions were as follows: the laminate lying on a flat surface with the actuator facing up as in Figure 5.4b (laminate concave up), the laminate lying on a flat surface with the actuator facing down (laminate concave down), and the laminate hanging freely by the strain gage wire. The last position, shown in Figure 5.5a, was the only position in which the laminate consistently snapped from one configuration to the other with only a single snapping event, as predicted with the transition from point 4 to point 5 in Figure 5.2. In the other positions, the laminate would sometimes only partially snap (only one or two corners reversing curvature), partially snap and then completely snap at a higher voltage as the voltage increased, or partially snap as the voltage was being increased and then completely snap as the voltage was decreased back to zero. The configurations of the laminate while only partially snapped were not captured by the model. However, in the model, the laminate is also pinned in the middle; experimentally, this condition was most closely met by hanging the laminate by the strain gage wire, so these hanging experiments were examined most carefully. A review of all of the experimental data is given in Appendix C.

Six replicate experiments with the laminate hanging by the strain gage wire were performed. A representative strain vs. voltage relation from one of these experiments is seen in Figure 5.6. At zero voltage, the strain begins at zero; as the voltage to the actuator is increased, the strain initially becomes negative until about 800 V, where the strain then becomes positive and continues to

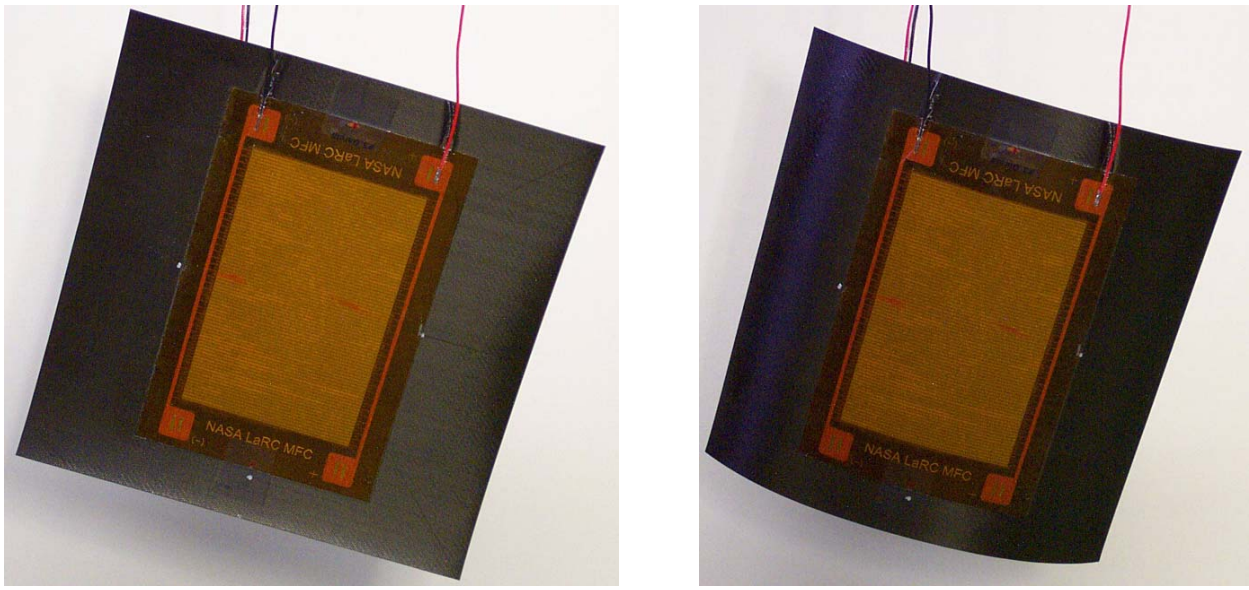

(a) - laminate in the other configuration, to be snapped (same configuration as Figure 5.4b)

(b) - laminate in the actuator-added configuration, after snapping (same configuration as Figure 5.4a)

Figure 5.5: The laminate hanging freely by the strain gage wire

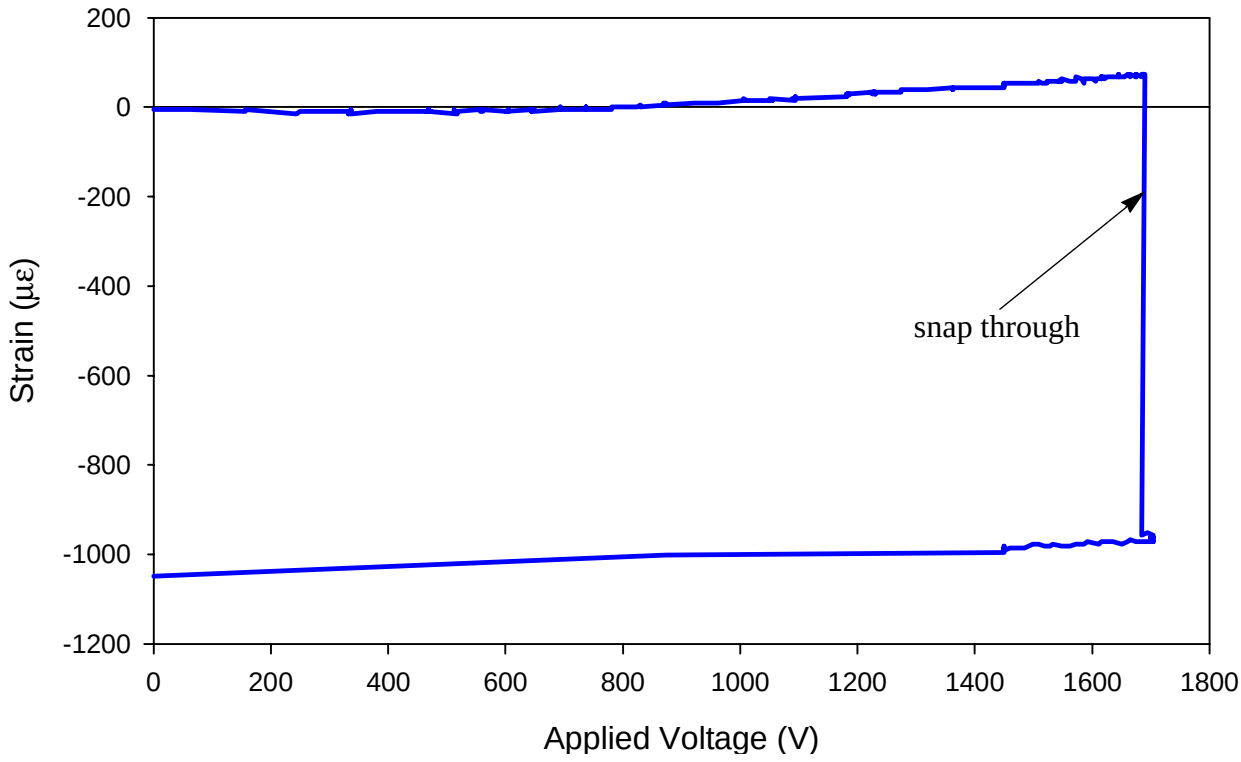

Figure 5.6: Representative strain vs. applied voltage for experiment with actuator/laminate structure hanging

increase until 1685 V. When the voltage reaches 1685 V, there is a sudden large jump in the strain that indicates that the actuator/laminate structure has snapped through to the other configuration.

For the case shown in Figure 5.6, the snapping voltage was 1685 V, almost twice the voltage of 904 V predicted by the model. In fact, for all six of the experiments with the actuator/laminate structure hanging, the snapping voltages were much higher than the predicted snapping voltage; these snapping voltages were 1773 V, 1665 V, 1714 V, 1685 V, 1636 V, 1704 V, with an average snapping voltage of 1695 V.

This factor-of-two discrepancy was troubling and certainly less than satisfying. The next chapter will reexamine the in-depth model and present revisions intended to decrease the discrepancies between the analysis and the experiments.

Chapter 6 Revised In-Depth Modeling of an Unsymmetric Laminate and Actuator

As discussed in Chapter 5, the snapping voltages measured during the experiments were much greater than they were predicted to be. Because of this discrepancy in snapping voltages, the experimental conditions, including details of the laminate, and the model were reexamined. First, the major curvatures of the laminate before the actuator was bonded were reconsidered, including consideration of the magnitude difference in the major curvatures of the two cylindrical shapes. Calculation of the curvatures that were measured just prior to bonding the actuator revealed that the curvatures were smaller than those used in the model prediction; the precaution of reheating the laminate prior to bonding the actuator did not recover all of the lost curvature. As given by equation (5.5), the curvatures just prior to bonding the actuator to the laminate were measured to be

$$\begin{aligned} \kappa_x^\circ &= -9.46 \text{ m}^{-1} \\ \kappa_y^\circ &= 8.63 \text{ m}^{-1} \end{aligned} \tag{6.1}$$

In addition, the *shapes* of the actual laminate were reexamined. The model predicted well the shapes of the laminate without the actuator and the actuator-added shape of the laminate. However, the model did not predict well the second stable shape of the laminate after the actuator was added. As is seen in Figure 6.1, the actual second shape of the laminate was not a cylinder, as assumed by the displacement fields of equation (4.8). Near the middle of the actual laminate, there was a region where the curvature was opposite to the main direction of curvature; in other

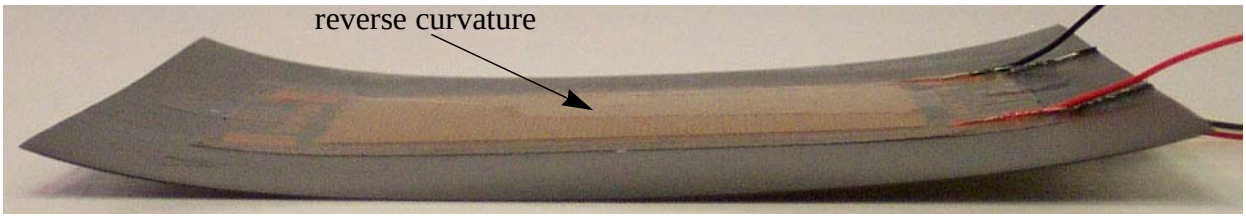

Figure 6.1: Side view of the laminate in the second stable configuration

words, there was a localized region of reverse curvature in the middle of the actual laminate when it was in the second stable configuration. The displacement fields that were used in the model were not of high enough order to capture this reverse curvature. Equation (4.9) indicates that the assumed displacement field for $w^{\circ}(x, y)$ results in constant curvature predictions over the entire laminate. It was believed that the inability to capture this localized region of reverse curvature was one reason for the lower snapping voltage in the prediction. Not coincidentally, this region of localized reverse curvature coincided with the location of the actuator. It is felt that the increase in local stiffness, particularly in the direction of the piezoceramic macrofibers, due to the addition of the actuator was responsible for the reverse curvature effect.

A number of revisions were made to the in-depth model in order to obtain better agreement between the model and the experiment. First, the ΔT in the model was again changed to match the average of the actual major curvatures of equation (6.1). Second, using that ΔT, the difference in the major curvatures in the two different configurations of the laminate was considered by assuming that the two layers of the laminate were not of equal thickness. Physically, this could easily be the case due to uneven matrix bleed-off during fabrication of the laminate in the pressclave. Hamamoto and Hyer [7] used this approach with success when trying to match experimental results with predictions. A revised ten-coefficient in-depth Rayleigh-Ritz model with higher order displacement fields was also created to try to capture the localized reverse curvature that is seen in the actuator/laminate structure. These points are discussed in the next sections.

6.1 Revised Four-Coefficient In-Depth Model

6.1.1 Temperature Adjustment

Similar to the method discussed in Section 5.1.1, in order to match the average major curvature of the laminate prior to bonding the actuator, the ΔT was again varied relative to the actual temperature change from the cure temperature. However, this time, rather than calculating κ_x° and κ_y° from equation (4.6), the major curvatures from the model were calculated along the edge of the laminate using the geometric argument of equation (5.2), the same way as for the actual laminate. To match the experimentally measured curvatures of equation (6.1), the ΔT was chosen to be -117 °C. This resulted in a calculated average curvature of 9.02 m^{-1} and a snapping voltage of 599 V. By decreasing the magnitude of the ΔT to -117 °C, the discrepancy between the model prediction for snapping voltage and the experiments was increased. This modification, obviously, did not resolve the problem.

6.1.2 Thickness Adjustment

Next, the curvature difference of the two different configurations of the laminate prior to bonding on the actuator was addressed. As mentioned earlier, the layers were previously assumed to be the same thickness (0.136 mm) and to have the same material properties (given in Table 5.1). It was assumed that the difference in the measured major curvatures in the two cylindrical configurations prior to bonding on the actuator was caused by a difference in matrix bleed in the two layers during manufacture. In order to capture this analytically, the layer thicknesses were varied, keeping the laminate thickness constant at 0.272 mm. For consistency, the layer properties were also varied using micromechanics equations [36], as follows:

$$
\begin{aligned}
E_1 &= E_1^f V^f + E^m(1 - V^f) \\
\nu_1 &= \nu_{12}^f V^f + \nu^m(1 - V^f) \\
\frac{1}{E_2} &= \frac{\dfrac{V^f}{E_2^f} + \dfrac{\eta(1 - V^f)}{E^m}}{V^f + \eta(1 - V^f)} \\
\frac{1}{G_{12}} &= \frac{\dfrac{V^f}{G_{12}^f} + \dfrac{\eta'(1 - V^f)}{G^m}}{V^f + \eta'(1 - V^f)} \\
\alpha_1 &= \frac{(\alpha_1^f E_1^f - \alpha^m E^m)V^f + \alpha^m E^m}{(E_1^f - E^m)V^f + E^m} \\
\alpha_2 &= \alpha^m + (\alpha_2^f - \alpha^m)V^f + \left(\frac{E_1^f \nu^m - E^m \nu_{12}^f}{E_1}\right)(\alpha^m - \alpha_1^f)(1 - V^f)V^f
\end{aligned}
\tag{6.2}
$$

In the above, E^m, ν^m, and α^m are the extensional modulus, Poisson's ratio, and the coefficient of thermal expansion of the matrix, respectively. The variables E_1^f and E_2^f are the axial and diametrical extensional moduli of the fiber, respectively, ν_{12}^f is the major Poisson's ratio, and G_{12}^f is the shear modulus of the fiber in the axial-diametrical plane of the fiber. The fiber volume fraction is V^f, and η and η' are stress-partitioning factors. Matrix properties were assumed, as were fiber volume fraction and the stress partitioning factors. Equation (6.2) was then used to calculate the fiber properties based on the layer properties of Table 5.1 and the values of Table 6.1. This was done by first using the first four equations of equation 6.2 to calculate E_1^f, ν_{12}^f, E_2^f, and G_{12}^f. Then the calculated values of E_1^f and ν_{12}^f, and the last two equations of equation 6.2 were used to calculate α_1^f and α_2^f. Once the fiber properties were calculated, the thickness, and as a consequence the fiber volume fractions, of each layer was varied and equation (6.2) was used to determine the material properties as a function of layer thickness.

Table 6.1: Assumed properties for micromechanics models

Property	Value	Property	Value
E_m (GPa)	4.62	η	0.45
ν_m	0.360	η'	0.6
α_m (1/°C)	41.4×10^{-6}	V_f	0.65

In order to match the measured values of major curvature for the laminate with no actuator added, it was necessary to increase the thickness of layer 1 and decrease the thickness of layer 2 by 1.6%. The new layer properties, using the new layer thicknesses, are given in Table 6.2. The predicted major curvatures, again calculated using equation (5.2), with the new layer material properties, thickness, and ΔT of −117 °C were

$$\begin{aligned} \kappa_x^\circ &= -9.43\ \mathrm{m}^{-1} \\ \kappa_y^\circ &= 8.61\ \mathrm{m}^{-1} \end{aligned} \tag{6.3}$$

These curvatures are meant to compare with the values of $-9.46\ \mathrm{m}^{-1}$ and $8.64\ \mathrm{m}^{-1}$ of equation (6.1), which were measured just prior to bonding the actuator. The predicted snapping voltage was again calculated, using $\Delta T = -117$ °C, rather than the actual decrease to room temperature of −157 °C, and found to be 771 V. This is an increase of 172 V over the prediction of 599 V, discussed earlier in Section 6.1.1, when the thicknesses were not adjusted to account for the curvature difference. Although the snapping voltage was still much lower than the experimental values, the increase in voltage indicates that the thickness adjustment was an important consideration.

The curvature vs. voltage relations for the temperature- and thickness-adjusted four-coefficient in-depth model are seen in Figure 6.2. These figures show the best prediction for the behavior of the laminate that could be obtained with the four-coefficient model. This figure is similar to Figure 5.2, except only positive voltages are considered.

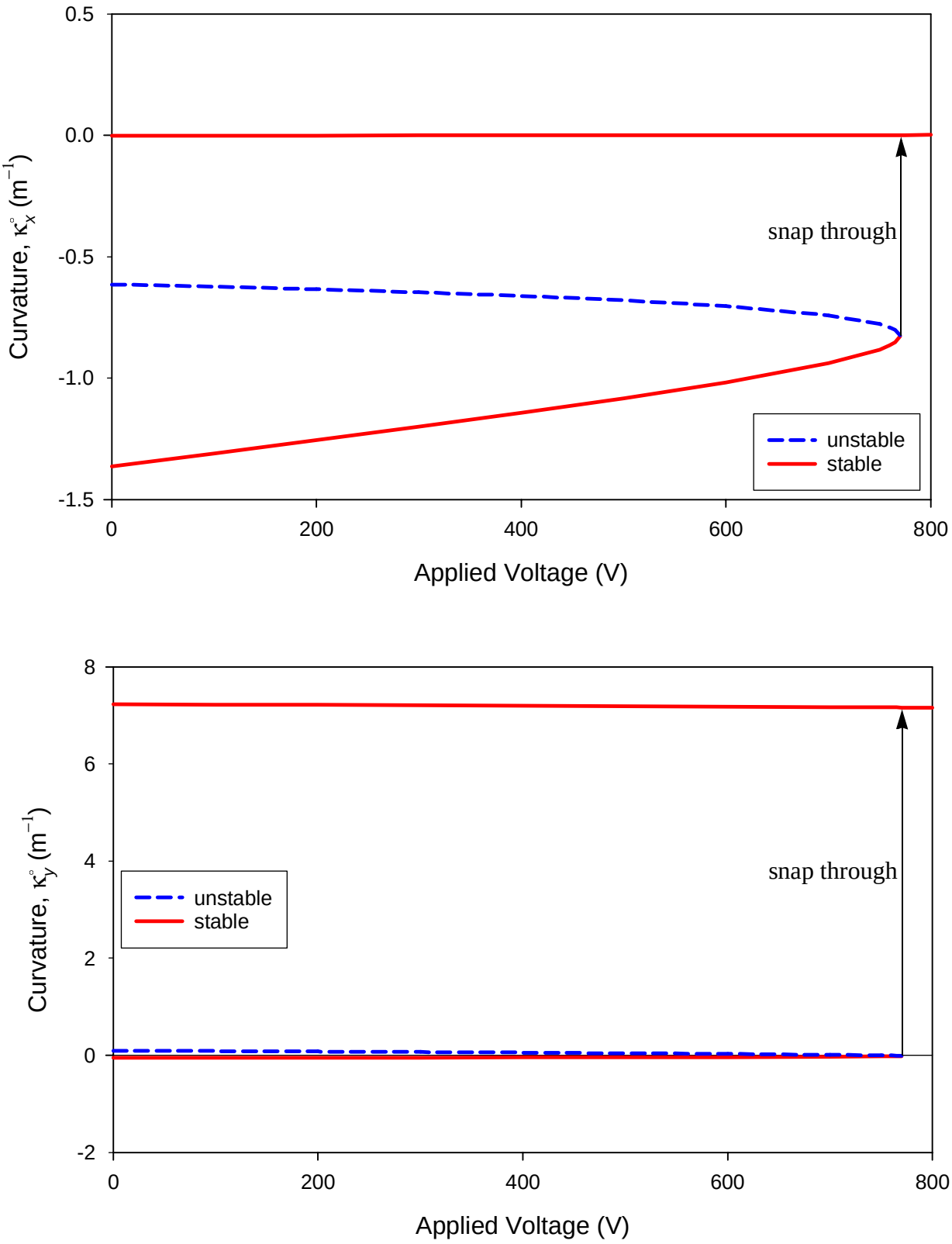

Figure 6.2: Curvatures vs. applied voltage for the temperature- and thickness-adjusted four-coefficient in-depth model

Table 6.2: Thickness-adjusted layer properties

Layer 1		Layer 2	
Property	Value	Property	Value
E_1 (GPa)	132.0	E_1 (GPa)	128.0
E_2 (GPa)	9.798	E_2 (GPa)	9.608
G_{12} (GPa)	5.112	G_{12} (GPa)	4.895
ν_{12}	0.2990	ν_{12}	0.3009
α_1 (1/°C)	-0.04156×10^{-6}	α_1 (1/°C)	5.538×10^{-9}
α_2 (1/°C)	23.77×10^{-6}	α_2 (1/°C)	24.78×10^{-6}
h (m)	1.338×10^{-4}	h (m)	1.382×10^{-4}

6.2 Ten-Coefficient In-Depth Model

Because, even with revisions, the four-coefficient model was unable to predict snapping voltages that were close to the experimental values, the in-depth model was modified with more complex displacement fields. The main goal for considering new displacement fields was to be able to capture the more localized effect of the area with the local reverse curvature that was discussed earlier and is seen in Figure 6.1. The in-depth model was modified to use higher-order displacement fields.

6.2.1 Development of the Ten-Coefficient In-Depth Model

To account for the localized reverse curvature effect, the new displacement fields are chosen to be

$$
\begin{aligned}
u^\circ &= c_5 x + \frac{1}{3}c_6 x^3 + c_7 x y^2 - \frac{1}{6}c_1^2 x^3 - \frac{1}{8}c_1 c_3 x^4 - \frac{1}{40}c_3^2 x^5 \\
v^\circ &= c_8 y + c_9 x^2 y + \frac{1}{3}c_{10} y^3 - \frac{1}{6}c_2^2 y^3 - \frac{1}{8}c_2 c_4 y^4 - \frac{1}{40}c_4^2 y^5 \\
w^\circ &= \frac{1}{2}(c_1 x^2 + c_2 y^2) + \frac{1}{6}(c_3 x^3 + c_4 y^3)
\end{aligned}
\tag{6.4}
$$

Because of symmetry requirements on the displacement for the entire laminate, the third-order w° displacement cannot be used to capture the w° displacement over the whole laminate. However, it is assumed that the laminate response exhibits quadrant symmetry. Therefore, a quarter-symmetry argument is used to allow the use of the third-order w°-displacement field, and the total potential energy is calculated over only one quarter of the laminate.

The approach used with the ten-coefficient model is very similar to that of the four-coefficient model, which was discussed in Chapter 4. However, because of the new displacement fields, there are some differences. Most notably, the expressions for total potential energy are modified to reflect the quarter-symmetry argument, and the midplane in-plane shear strain is no longer zero. The expressions for total potential energy become

$$
\begin{aligned}
\Pi_1 &= 4\left(\frac{1}{2}\int_0^{\frac{L_x}{2}}\int_0^{\frac{L_y}{2}}\int_{z_0}^{z_2}[(\sigma_x - \sigma_x^T)\varepsilon_x + (\sigma_y - \sigma_y^T)\varepsilon_y + (\sigma_{xy} - \sigma_{xy}^T)\gamma_{xy}]\,dx\,dy\,dz\right) \\
\Pi_2 &= 4\left(\frac{1}{2}\int_0^{\frac{L_x^{MFC}}{2}}\int_0^{\frac{L_y^{MFC}}{2}}\int_{z_2}^{z_3}[\sigma_x^a \varepsilon_x^a + \sigma_y^a \varepsilon_y^a + \sigma_{xy}^a \gamma_{xy}^a]\,dx\,dy\,dz\right) \\
\Pi_3 &= 4\left(\frac{1}{2}\int_0^{\frac{L_x^{MFC}}{2}}\int_0^{\frac{L_y^{MFC}}{2}}\int_{z_2}^{z_3}[(\sigma_x^a - \sigma_x^{Ea})\varepsilon_x + (\sigma_y^a - \sigma_y^{Ea})\varepsilon_y + (\sigma_{xy}^a - \sigma_{xy}^{Ea})\gamma_{xy}]\,dx\,dy\,dz\right)
\end{aligned}
\tag{6.5}
$$

and the midplane strains and curvatures are given by (using equations (4.5) and (4.6))

$$
\begin{aligned}
\varepsilon_x^\circ &= c_5 + c_6 x^2 + c_7 y^2 \\
\varepsilon_y^\circ &= c_8 + c_9 x^2 + c_{10} y^2 \\
\gamma_{xy}^\circ &= \frac{xy}{4}(2c_1 + c_3 x)(2c_2 + c_4 y) + 2xy(c_7 + c_9) \\
\kappa_x^\circ &= -(c_1 + c_3 x) \\
\kappa_y^\circ &= -(c_2 + c_4 y) \\
\kappa_{xy}^\circ &= 0
\end{aligned}
\tag{6.6}
$$

A comparison with equation (4.9), from the four-coefficient model, shows an increased complexity, in particular, nonconstant curvatures. The ten-coefficient model is completed in a manner similar to the four-coefficient model (equations (4.2) – (4.7), (4.12) – (4.14), (4.16) – (4.18), and (4.20) are used). In particular, the ten-coefficient model is separated into three parts, and, in each part, the stationary states of the total potential energy are found by solving a series of ten nonlinear simultaneous algebraic equations, namely solving

$$
\frac{\partial \Pi}{\partial c_k} = 0 \qquad k = 1, 10 \tag{6.7}
$$

where the total potential energy, Π, is equal to Π_1, or given by equation (4.14) or (4.20), depending on which part of the model is being considered. Fortunately, coefficients $c_5 - c_{10}$ may be solved for in terms of c_1, c_2, c_3, and c_4, so the problem reduces to solving four simultaneous equations in $c_1 - c_4$. The shape of the entire laminate can be described using these four coefficients. Stability of the solutions is found by determining if the stability matrix, a ten-by-ten matrix similar to equation (2.17), is positive definite.

6.2.2 Use and Results of the Ten-Coefficient In-Depth Model

6.2.2.1 Temperature Adjustment

A procedure similar to that of the four-coefficient model was used to determine the snapping voltage of a laminate like that used in the experiment. First, assuming equal layer thicknesses, ΔT was varied until the predicted major curvature, using equation (5.2), matched the average experimental major curvature. A ΔT of –117 °C was chosen and gave a major curvature of 9.01 m^{-1} for the stable shapes. With this value of ΔT and equal layer thicknesses, the snapping voltage was found to be 918 V. The use of the higher-order displacement fields increased the prediction of the snapping voltage by 319 V over the four-coefficient model with equal layer thicknesses, Section 6.1.1. This value, because it is closer to the measured snapping voltage, shows that the increased complexity of the ten-coefficient model has increased its accuracy.

6.2.2.2 Thickness Adjustment

Next, in order to match the major curvatures of the two stable shapes of the actual laminate, the layer thicknesses were changed using the same procedure as described in Section 6.1.2. Again a 1.6% change in layer thickness from the nominal thickness produced the best correlation with the experiment, namely major curvatures of

$$\begin{aligned} \kappa_x^\circ &= -9.43 \text{ m}^{-1} \\ \kappa_y^\circ &= 8.61 \text{ m}^{-1} \end{aligned} \tag{6.8}$$

Using the ΔT of –117 °C and the 1.6% change in layer thickness, the predicted snapping voltage was predicted to be 1262 V. Because the curvatures of the laminate are not constant over the entire laminate and may no longer be described by only one coefficient each, the variations of the four coefficients, $c_1 - c_4$, vs. voltage are shown in Figures 6.3 and 6.4. As with the earlier calcula-

tions of the laminate shape, there were values of the coefficients that correspond to stable solutions and values that correspond to unstable solutions. The predicted shapes and pictures of the actuator/laminate structure with the actuator are seen in Figure 6.5. Examination of the actual and predicted shapes of Figure 6.5 shows good qualitative agreement. In particular, note the quite flat, though slightly concave down, section and turned up corners that are captured by the model in Figure 6.5b and seen in the actual laminate in Figures 6.1 and 6.5a. To compare the predicted shapes of the second stable shape for the four- and ten-coefficient models, Figure 6.5b should be compared with Figure 5.3b, though details are difficult to discern. Also, the four- and ten-coefficient predicted w° displacements for the second shape are seen in Figure 6.6.

Adjusted for temperature and thickness, the ten-coefficient model did a good job of predicting both the snapping voltage and the shapes of the actuator/laminate structure. The predicted snapping voltage of 1262 V is 26% different from the average experimental snapping voltage of 1695 V. The quantitative agreement of the shapes was also reasonably good. For example, the measured rise, *h* of Figure 5.1, of the edge of the actual shape in Figure 6.5c and the predicted rise in Figure 6.5d are both 20 mm. In Figure 6.5a, the rise, *h*, of the edge of the actual laminate is 9 mm, while the predicted value in Figure 6.5b is 4 mm.

It can be concluded that the primary overall objective of the study, namely to prove that the concept of using unsymmetric laminates in conjunction with actuators is a viable approach to developing morphing structures, was met. Additionally, the final model developed in this study correlates fairly well with observations and measurements. The next chapter provides more detailed conclusions and discusses topics for moving the concept forward to the next level.

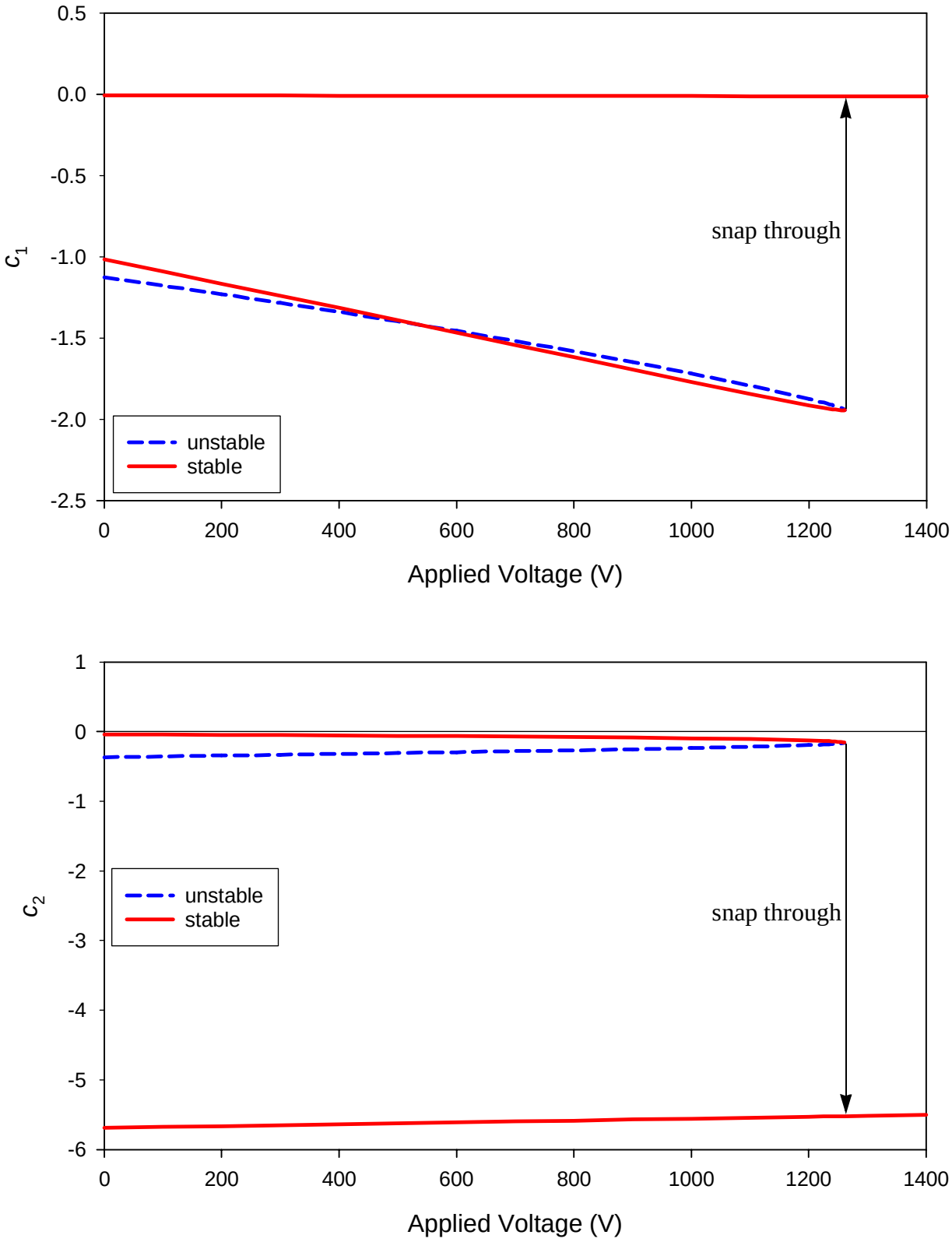

Figure 6.3: Coefficients c_1 and c_2 vs. applied voltage for the temperature- and thickness-adjusted ten-coefficient in-depth model

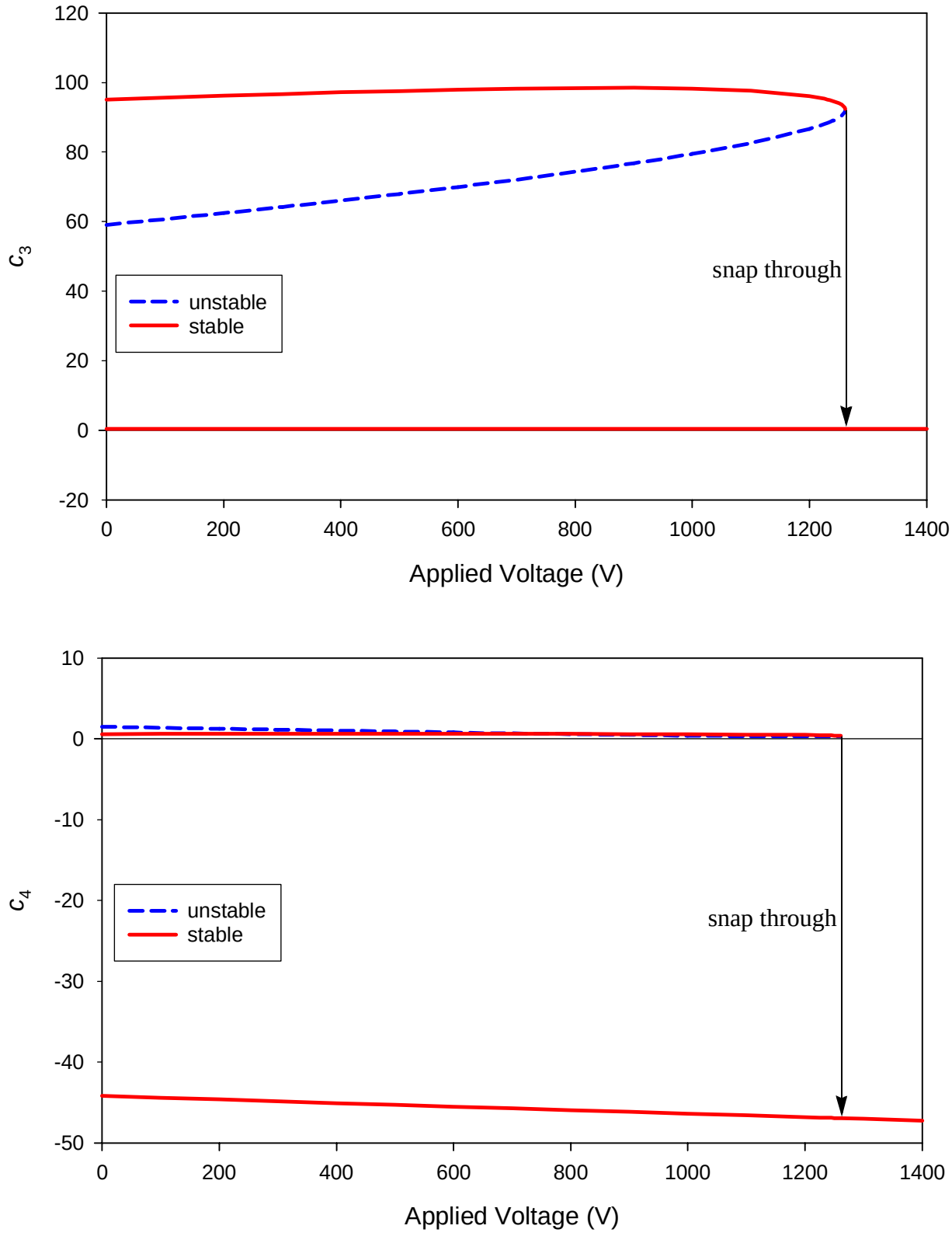

Figure 6.4: Coefficients c_3 and c_4 vs. applied voltage for the temperature- and thickness-adjusted ten-coefficient in-depth model

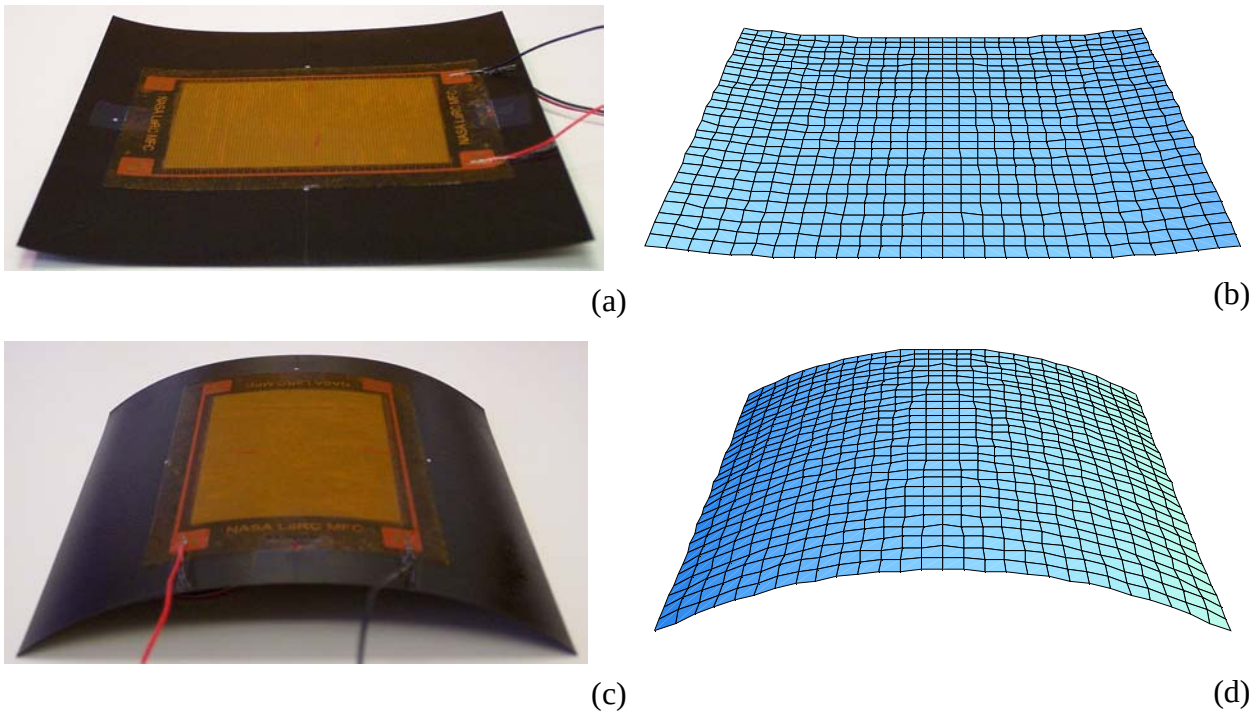

Figure 6.5: Shapes of the laminate with bonded actuator:
(a) and (c), actual shapes; (b) and (d), predicted shapes

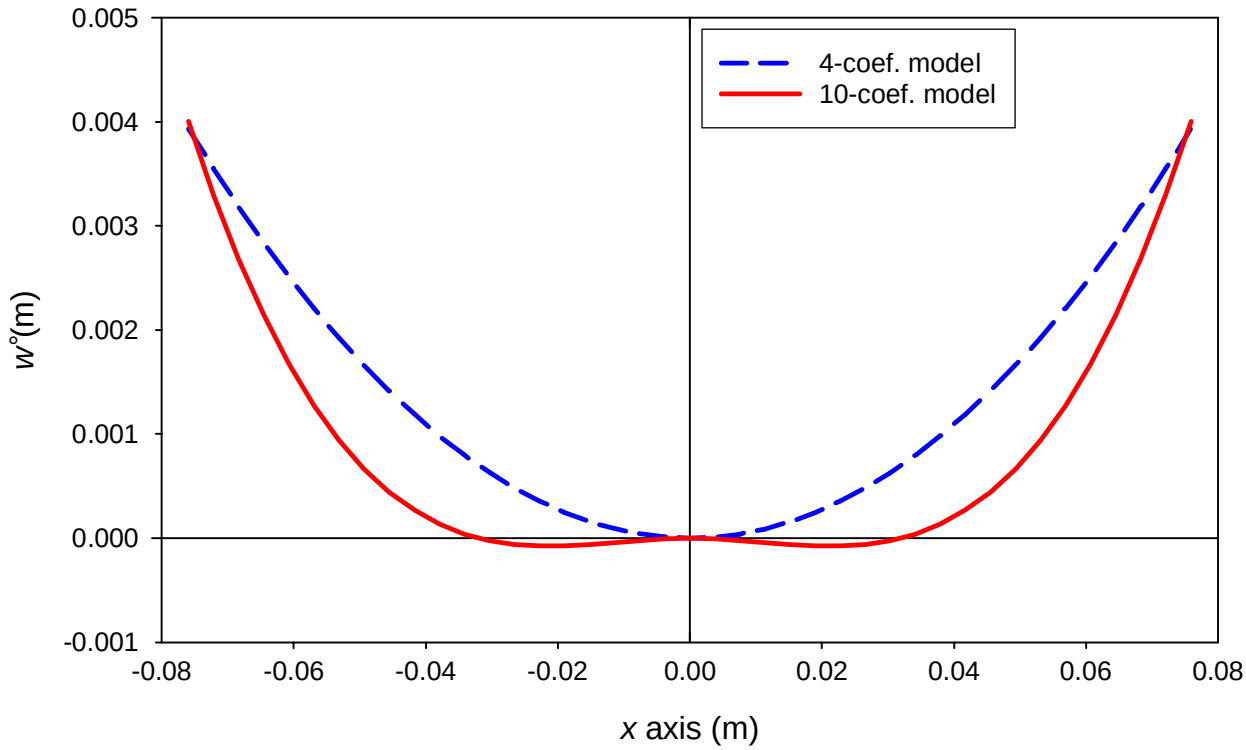

Figure 6.6: Comparison of $w°$ for the temperature- and thickness-corrected four-coefficient and ten-coefficient models, $y = 0$

Chapter 7 Conclusions and Future Work

7.1 Conclusions

Outlined in Chapter 1 were three specific objectives for this research effort: develop a model to predict the snap-through behavior of unsymmetric cross-ply laminates actuated with piezoelectric actuators; use the model to design an experiment where an unsymmetric laminate could be snapped through with a piezoelectric actuator; perform the designed experiments to compare with the developed model. These goals were intertwined and this discussion of how the goals were met will reflect this.

Several models were developed to predict the snap-through behavior of unsymmetric laminates with piezoelectric actuators. First, a simple and somewhat unrealistic initial model was developed as a proof-of-concept model and to learn about the problem. The major unrealistic assumption of this initial model was that the actuators were assumed to have been applied to the base laminate at the cure temperature of the laminate, when the laminate was curvature free. Other simplifying assumptions were that the actuators were isotropic piezoceramic, that the actuators fully covered the base laminate, and that the electric potential gradients in the top and bottom actuators were equal and opposite. Next, a much more realistic in-depth model was developed. This in-depth model considered partial coverage of the laminate by the actuator; the actuator on only one side of the laminate; the orthotropy of the NASA LaRC MFC actuator, which was the considered actuator; and room-temperature bonding of the laminate to the actuator. This in-depth model was used to design an experiment. A laminate was manufactured, an MFC actuator was bonded to it, and the actuator was actuated while monitoring the laminate shape. During and after the experimental phase of the work, the in-depth model was modified to better reflect the actual experiments. How-

ever, even with these adjustments, the in-depth model was not found to be adequate to predict the snap-through behavior of the modeled structure; the model did not do a good job of predicting either the shapes of the actuator/laminate structure, or of predicting the voltage needed to snap the laminate. Because of this inadequacy, the in-depth model was refined to include higher-order displacement fields that were better able to predict the actual laminate shapes; much better agreement with experiments was found. Experimentally, the major curvatures of the two stable equilibrium shapes were not the same. Agreement with experiment was again improved by modifying the layer thickness, and, for consistency, fiber volume fraction and material properties of the layers in the model to match the different experimental major curvatures. With these modifications, the model was able to better predict the shapes of the laminate, and was able to predict the snapping voltage within 26% of the measured values.

Although good correlation between model and experiment was eventually obtained, there are a number of reasons for differences. Perhaps the biggest reason for the differences is the Rayleigh-Ritz solution technique itself; the technique may not be able to capture localized interactions between the laminate and the actuator. As was seen, the correlation between model and experiment improved greatly with the higher-order displacement fields. However, increasing the order of the displacement fields quickly increases the complexity of simultaneous equations to be solved; this practically limits the order of the displacement fields. Another reason for differences may have had to do with characterization of the MFC actuators; full characterization of the MFC actuators is still being conducted. In this work, the piezoelectric effect was assumed (and, through the calibration tests, shown) to be linear; however; for large voltages or strains, the effect may be nonlinear, and, in fact, dependent on stress level. Through full characterization, the material properties may also be found to be different from those used in this work. It is troubling that the primary piezoelectric coefficient, d_{11}, that was found through the calibration experiments was almost a factor of two less than that provided by Wilkie et al. [31].

7.2 Future Work

In order to progress with this research, there is a need to develop a more general approach to analyzing the actuator/laminate structures. Though there are many approaches to studying structures, simple or complex, with actuators, as evidenced by the list of references, the work here is more complicated. The concept presented includes large deformations, large enough to require the inclusion of geometric nonlinearities. Additionally, there are multiple equilibrium solutions for a given value of applied voltage. Finding multiple solutions, either analytically or numerically, is often difficult. Finally, since some of the multiple equilibrium solutions represent unstable conditions, the ability to evaluate stability is important. One way to continue this work would be to model the problem using finite-element methods. The finite-element approach could be compared with the Rayleigh-Ritz model and with experiments. However, finite-element approaches can become complicated for multiple-solution nonlinear problems with instabilities. It is, nonetheless, felt to be a valuable approach, but one that must be applied in an evolutionary fashion, starting with simple finite-element models and then developing more complex models.

Once a finite-element approach has been developed, finite-element modeling could be used to consider other interesting actuator/laminate structures. The actuation properties of the MFC actuators have been improved since the actuators were obtained for the Ph.D research. In addition, several geometries of MFC actuators are produced, and the ability to produce other geometries exists. The availability of the newer MFC actuators in additional geometries would allow investigation into several areas, some of which are discussed below.

To be useful, the actuator/laminate structures will probably have to be able to be snapped both ways; i.e. starting in one configuration, the laminate is snapped to the second configuration and then back, using only voltage input to the MFC actuators. This will be an improvement over the current work where the laminate has been snapped only in one direction, but not back again. One could search for combinations of laminates and actuators for which the laminate can be snapped both ways. With this concept, the actuator/laminate structure would be able to be made to have a flapping-type action, an action that could prove useful.

As was indicated by the sound that was heard as the laminate snaps, snapping from one shape to the other was a dynamic and rather violent event. It would be desirable if the laminate could be morphed from one shape to another in a more controlled manner. Perhaps, if back-to-back actuators were used on a laminate, one of the actuators could be used to “catch” the laminate as it begins to snap from one shape to another. This controlled morphing could be another aspect to be examined during future work.

In the course of examining actuator/laminate structures that can be snapped both ways and those that have controlled morphing, laminates other than cross-ply laminates could be considered. In addition, a series of smaller, distributed actuators, rather than a single large actuator on each side, could be considered. Also, any nonlinearity of the piezoelectric effect could be taken into effect with new modeling. If desirable combinations of laminates and actuators were found analytically, experiments could be designed to verify the results.

References

1. Goldin, D. S., Venneri, S. L., and Noor, A. K. “Fresh Air, Wide-Open Space,” *Mechanical Engineering*, Vol. 123, No. 11, Nov. 2001, pp. 48–55.
2. Sietzen, F. Jr. “New Blueprint for NASA Aeronautics,” *Aerospace America*, Aug. 2002, pp. 24–28.
3. Agnes, G. S. “Adaptive Structures,” *Aerospace America*, Dec. 2001, p. 78.
4. Wilson, J. R. “Active Aeroelastic Wing: A New/Old Twist on Flight,” *Aerospace America*, Sept. 2002, pp. 34–37.
5. Hyer, M. W. “Calculations of the Room-Temperature Shapes of Unsymmetric Laminates,” *Journal of Composite Materials*, Vol. 15, Jul. 1981, pp. 296–310.
6. Hyer, M. W. “The Room-Temperature Shapes of Four-Layer Unsymmetric Cross-Ply Laminates,” *Journal of Composite Materials*, Vol. 16, Jul. 1982, pp. 319–340.
7. Hamamoto, A. and Hyer, M. W. “Non-Linear Temperature-Curvature Relationships for Unsymmetric Graphite-Epoxy Laminates,” *International Journal of Solids and Structures*, Vol. 23, No. 7, 1987, pp. 919–935.
8. Dano, M.-L. and Hyer, M. W. “Thermally-Induced Deformation Behavior of Unsymmetric Laminates,” *International Journal of Solids and Structures*, Vol. 35, No. 17, 1998, pp. 2101–2120.
9. Dano, M.-L. and Hyer, M. W. “Snap-Through of Unsymmetric Fiber-Reinforced Composite Laminates,” *International Journal of Solids and Structures*, Vol. 39, 2002, pp. 175–198.
10. Mason, W. P. “Piezoelectricity, Its History and Applications,” *Journal of the Acoustical Society of America*, Vol. 70, 1981, pp. 1561–1566.
11. Crawley, E. F. and de Luis, J. “Use of Piezoelectric Actuators as Elements of Intelligent Structures,” *AIAA Journal*, Vol. 25, 1987, pp. 1373–1385.
12. Cady, W. G. *Piezoelectricity: An Introduction to the Theory and Applications of Electromechanical Phenomena in Crystals*, McGraw-Hill, New York, 1946.
13. Tiersten, H. F. *Linear Piezoelectric Plate Vibrations: Elements of the Linear Theory of Piezoelectricity and the Vibrations of Piezoelectric Plates*, Plenum Press, New York, 1969.
14. Ray, M. C., Bhattacharya, R., and Samanta, B. “Exact Solutions for Static Analysis of Intelligent Structures,” *AIAA Journal*, Vol. 31, pp. 1684–1691.
15. Ray, M. C., Rao, K. M., and Samanta, B. “Exact Analysis of Coupled Electroelastic Behavior of a Piezoelectric Plate Under Cylindrical Bending,” *Computers and Structures*, Vol. 45, 1992, pp. 667–677.

References

16. Ray, M. C., Rao, K. M., and Samanta, B. "Exact Solution for Static Analysis of Intelligent Structures Under Cylindrical Bending," *Computers and Structures*, Vol. 47, 1993, pp. 1031–1042.
17. Heyliger, P. "Exact Solutions for Simply Supported Laminated Piezoelectric Plates," *ASME Journal of Applied Mechanics*, Vol. 64, 1997, pp. 299–306.
18. Heyliger, P. and Brooks, S. "Exact Solutions for Laminated Piezoelectric Plates in Cylindrical Bending," *Journal of Applied Mechanics*, Vol. 63, Dec. 1996, pp. 903–910.
19. Heyliger, P. R. and Brooks, S. P. "Free Vibration of Piezoelectric Laminates in Cylindrical Bending," *International Journal of Solids and Structures*, Vol. 32, 1995, pp. 2945–2959.
20. Benveniste, Y. and Dvorak, G. J. "Uniform Fields and Universal Relations in Piezoelectric Composites," *Journal of the Mechanics of Physics and Solids*, Vol. 40, No. 6, 1992, pp. 1295–1312.
21. Pagano, N. J. "Exact Solutions for Composites in Cylindrical Bending," *Journal of Composite Materials*, Vol. 3, 1969, pp. 398–411.
22. Pagano, N. J. "Exact Solutions for Rectangular Bidirectional Composites and Sandwich Plates," *Journal of Composite Materials*, Vol. 4, 1970, pp. 20–34.
23. Vel, S. S. and Batra, R. C. "Three-Dimensional Analytical Solutions for Hybrid Multilayered Piezoelectric Plates", *Journal of Applied Mechanics*, Vol. 67, No. 3, pp. 558–567, 2000.
24. Crawley, E. F., and Anderson, E. H. "Detailed Models of Piezoceramic Actuation of Beams," *Journal of Intelligent Material Systems and Structures*, Vol. 1, 1990, pp. 4–25.
25. Lee, C. K. "Theory of Laminated Piezoelectric Plates for the Design of Distributed Sensors/Actuators. Part I: Governing Equations and Reciprical Relationships," *Journal of the Acoustical Society of America*, Vol. 87, 1990, pp. 1144–1158.
26. Wang, B. T. and Rogers, C. A. "Laminate Plate Theory for Spatially Distributed Induced Strain Actuators," *Journal of Composite Materials*, Vol. 25, pp. 433–452.
27. Huang, J. H. and Wu, T. L. "Analysis of Hybrid Multilayered Piezoelectric Plates," *International Journal of Engineering Science*, Vol. 34, 1996, pp. 171–181.
28. Heyliger, P. R., Ramirez, G., and Saravanos, D. "Coupled Discrete-Layer Finite Element Models for Laminated Piezoelectric Plates," *Communications in Numerical Methods in Engineering*, Vol. 10, 1994, pp. 971–981.
29. Saravanos, D. A. and Heyliger, P. R. "Coupled Electromechanical Response of Composite Beams with Embedded Piezoelectric Sensors and Actuators," *International Journal of Intelligent Material Systems and Structures*, Vol. 6, 1995, pp. 350–363.
30. Janos, B. Z. and Hagood, N. W. "Overview of Active Fiber Composites Technology," Proceedings of the 6th International Conference on New Actuators - ACTUATOR98, Bremen, Germany, June 1998.
31. Wilkie, W. K., Bryant, R. G., High, J.W., Fox, R. L., Hellbaum, R. F., Jalink, A., Jr., Little, B. D., and Mirick, P. H. "Low-Cost Piezocomposite Actuator for Structural Control Applications," SPIE's 7th Annual International Symposium on Smart Structures and Materials, Newport Beach, CA, March 5–9, 2000.
32. Loewy, Robert G. "Recent Developments in Smart Structures with Aeronautical Applications," *Smart Materials and Structures*, Vol. 6, No. 5, Oct. 1997, p. R11–R42.

References

33. Rogers, Craig A. “Editorial: Intelligent Material Systems–The Dawn of a New Materials Age,” *Journal of Intelligent Material Systems and Structures*, Vol. 4, Jan. 1993, pp. 4–12.
34. Utku, Senol, and Wada, Ben K. “Review: Adaptive Structures in Japan,” *Journal of Intelligent Material Systems and Structures*, Vol. 4, Oct. 1993, pp. 437–451.
35. Wolfram, Stephen, *The Mathematica Book*. New York, NY: Cambridge University Press, 1999.
36. Hyer, M. W. *Stress Analysis of Fiber-Reinforced Composite Materials*. New York, NY: McGraw-Hill, 1998.
37. *ABAQUS Theory Manual, Version 5.8*, Hibbitt, Karlsson, & Sorenson, Inc., 1998.
38. Wilkie, W. K., personal correspondence.

Appendix A Model Comparisons

In order to better understand the piezoelectric effect and to verify several assumptions that are often used, several models of piezoelectric plates were developed and compared. Two simple, but relevant, problem types were selected. The modeling efforts considered in this appendix consist of four approaches: closed-form three-dimensional elasticity solutions; modified approximate solutions, based on the equations of elasticity; finite-element method (FEM) solutions using *ABAQUS* [A.1]; and semi-infinite plate-type solutions. Two simple problems were solved with each of the first three types of solution; these problems each consisted of a piezoelectric plate with electric potentials, applied to the top and bottom surface of the plate, that varied spatially in harmonic fashion. An additional two problems that consisted of a two-layer plate (one graphite/ epoxy (Gr/Ep) composite layer and one piezoelectric layer) were also solved; again the piezoelectric plate had electric potentials that varied spatially in harmonic fashion were applied to the top and bottom surfaces. These two-layer problems were solved using the three-dimensional elasticity solutions, the *ABAQUS* finite-element solutions, and the semi-infinite plate solutions.

A.1 Piezoelectric Constitutive Equations

Piezoelectric materials undergo a strain if an electric potential gradient (electric field) is applied through the material. Likewise, if a piezoelectric material is strained, it will create an electric potential gradient. Thus, the electric and elastic properties are coupled. This coupling is seen in the three-dimensional Cartesian constitutive equations as given by Tiersten [A.2]:

$$\begin{bmatrix}\sigma_{11}\\ \sigma_{22}\\ \sigma_{33}\\ \sigma_{23}\\ \sigma_{31}\\ \sigma_{12}\end{bmatrix} = \begin{bmatrix} C_{1111} & C_{1122} & C_{1133} & 0 & 0 & 0\\ C_{1122} & C_{2222} & C_{2233} & 0 & 0 & 0\\ C_{1133} & C_{2233} & C_{3333} & 0 & 0 & 0\\ 0 & 0 & 0 & C_{2323} & 0 & 0\\ 0 & 0 & 0 & 0 & C_{3131} & 0\\ 0 & 0 & 0 & 0 & 0 & C_{1212}\end{bmatrix}\begin{bmatrix}\varepsilon_{11}\\ \varepsilon_{22}\\ \varepsilon_{33}\\ 2\varepsilon_{23}\\ 2\varepsilon_{31}\\ 2\varepsilon_{12}\end{bmatrix} - \begin{bmatrix} 0 & 0 & e_{311}\\ 0 & 0 & e_{322}\\ 0 & 0 & e_{333}\\ 0 & e_{223} & 0\\ e_{113} & 0 & 0\\ 0 & 0 & 0\end{bmatrix}\begin{bmatrix}E_1\\ E_2\\ E_3\end{bmatrix} \qquad \text{(A.1)}$$

$$\begin{bmatrix}D_1\\ D_2\\ D_3\end{bmatrix} = \begin{bmatrix} 0 & 0 & 0 & 0 & e_{15} & 0\\ 0 & 0 & 0 & e_{24} & 0 & 0\\ e_{31} & e_{32} & e_{33} & 0 & 0 & 0\end{bmatrix}\begin{bmatrix}\varepsilon_{11}\\ \varepsilon_{22}\\ \varepsilon_{33}\\ 2\varepsilon_{23}\\ 2\varepsilon_{31}\\ 2\varepsilon_{12}\end{bmatrix} + \begin{bmatrix}\epsilon_{11} & 0 & 0\\ 0 & \epsilon_{22} & 0\\ 0 & 0 & \epsilon_{33}\end{bmatrix}\begin{bmatrix}E_1\\ E_2\\ E_3\end{bmatrix} \qquad \text{(A.2)}$$

In these equations, σ_{ij} are components of the stress tensor, C_{ijkl} are the stiffnesses, ε_{ij} are the components of the infinitesimal strain tensor, e_{ijk} are the piezoelectric coefficients, E_i are the components of the electric field, D_i are the electric displacements, and ϵ_{ij} are the electric permittivities. The piezoelectric coefficient matrix given is one that characterizes a material that has been *poled* such that a potential gradient in the 3 direction causes primarily a dilatational strain, while a potential gradient in the 1 direction or the 2 direction will cause primarily shear strains. Poling aligns the dipoles in a piezoceramic, which magnifies the piezoelectric effect, and is accomplished by applying a large potential gradient within the piezoceramic. A piezoelectric material may be poled in any direction; if poled in the 1 or 2 direction, the non-zero components of the piezoelectric coefficient matrix will be rearranged.

The infinitesimal strains are related to the displacements by the strain-displacement relations, namely,

$$\varepsilon_{ij} = \frac{1}{2}\left(\frac{\partial u_i}{\partial x_j} + \frac{\partial u_j}{\partial x_i}\right) \qquad i, j = 1, 3 \tag{A.3}$$

where the u_i are the displacements. The electric field is related to the gradient in the electric potential by

$$E_i = -\frac{\partial \phi}{\partial x_i} \qquad i = 1, 3 \tag{A.4}$$

where ϕ is the electric potential.

A.2 Geometry I, Problems I and II

The first geometry, Geometry I, studied in this modeling effort was created to study problems with a simple geometry and to parallel the problem considered by Heyliger and Brooks [A.3, A.4]. This geometry was the basis for the problems that were solved by the three three-dimensional approaches: elasticity solutions, modified approximate solutions based on elasticity, and finite-element solutions. In particular, this geometry consisted of a simply-supported piezoceramic plate, infinite in the x_1 direction, with a harmonic electrostatic potential distribution, independent of the x_1 direction, applied to both the top ($x_3 = +H/2$) and the bottom ($x_3 = -H/2$) of the plate (see geometry in Figure A.1). Also, for any quantity, it was assumed that

$$\frac{\partial}{\partial x_1}(\ \ ) = 0 \tag{A.5}$$

The boundary conditions were as follows:

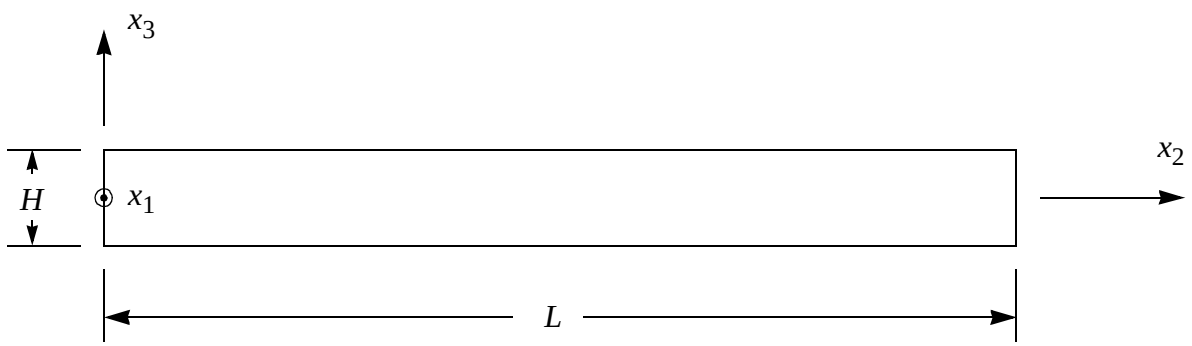

Figure A.1: Geometry I, geometry of semi-infinite plate

On $x_2 = 0, L$

$$\begin{aligned} u_3(x_1, x_2, x_3) &= 0 \\ \phi(x_1, x_2, x_3) &= 0 \\ \sigma_{12}(x_1, x_2, x_3) &= 0 \\ \sigma_{22}(x_1, x_2, x_3) &= 0 \end{aligned} \tag{A.6}$$

On $x_3 = \pm$ H/2

$$\sigma_{i3}(x_1, x_2, x_3) = 0 \qquad i = 1, 3 \tag{A.7}$$

and on $x_3 = \pm$ H/2, ϕ is of the form

$$\phi(x_1, x_2, x_3) = \pm\phi_0 \sin\left(\frac{\pi x_2}{L}\right) \tag{A.8}$$

To suppress rigid body motion, along $x_2 = L/2$,

$$u_2(x_1, x_2, x_3) = 0 \tag{A.9}$$

Two problems with this geometry were considered; the difference was in the boundary conditions for the electric potential. In Problem I, the specified electric potential was of the form of equation (A.8) and was positive on both the top and bottom of the plate. In Problem II, the specified electric potential was of the form of equation (A.8) and was positive on the bottom, but negative on the top of the plate.

A.2.1 Elasticity Solutions

Using the full three-dimensional equations of elasticity, a solution was formulated. To meet the boundary conditions, solutions for the displacements and the electric potential were assumed to be of the form

$$\begin{aligned}
u_1(x_1, x_2, x_3) &= U(x_3)\cos\left(\frac{\pi x_2}{L}\right) = \overline{U}\, e^{\frac{\pi s x_3}{L}} \cos\left(\frac{\pi x_2}{L}\right) \\
u_2(x_1, x_2, x_3) &= V(x_3)\cos\left(\frac{\pi x_2}{L}\right) = \overline{V}\, e^{\frac{\pi s x_3}{L}} \cos\left(\frac{\pi x_2}{L}\right) \\
u_3(x_1, x_2, x_3) &= W(x_3)\sin\left(\frac{\pi x_2}{L}\right) = \overline{W}\, e^{\frac{\pi s x_3}{L}} \sin\left(\frac{\pi x_2}{L}\right) \\
\phi(x_1, x_2, x_3) &= \Phi(x_3)\sin\left(\frac{\pi x_2}{L}\right) = \overline{\Phi}\, e^{\frac{\pi s x_3}{L}} \sin\left(\frac{\pi x_2}{L}\right)
\end{aligned} \tag{A.10}$$

where $\overline{U}$, $\overline{V}$, $\overline{W}$, $\overline{\Phi}$ are to-be-determined constants and s is an unknown parameter.

In addition to the equations (A.1) – (A.4), the equilibrium equations,

$$\sigma_{ij,\,j} = 0 \qquad i, j = 1, 3 \tag{A.11}$$

and the charge equation of electrostatics,

$$D_{i,\,i} = 0 \qquad i = 1, 3 \tag{A.12}$$

are used to solve this problem.

Putting equations (A.1) – (A.4) and (A.10) into the equilibrium and charge equations, equations (A.11) and (A.12), using equation (A.5), and finally dividing by the harmonic terms leads a system of four homogeneous algebraic equations in the constants of the three displacement equations and the electric potential equation of equation (A.10), namely,

$$\begin{bmatrix} (C_{3131}s^2 - C_{1212})p^2 & 0 & 0 & 0 \\ 0 & (-C_{2222} + C_{2323}s^2)p^2 & (C_{2233} + C_{2323})p^2 s & (e_{223} + e_{322})p^2 s \\ 0 & -(C_{2233} + C_{2323})p^2 s & (-C_{3333}s^2 + C_{2323})p^2 & (-e_{223} + e_{333}s^2)p^2 \\ 0 & -(e_{223} + e_{322})p^2 s & (-e_{223} + e_{333}s^2)p^2 & (\epsilon_{22} - \epsilon_{33}s^2)p^2 \end{bmatrix} \begin{bmatrix} \overline{U} \\ \overline{V} \\ \overline{W} \\ \overline{\Phi} \end{bmatrix} = \begin{bmatrix} 0 \\ 0 \\ 0 \\ 0 \end{bmatrix} \tag{A.13}$$

The first equation of (A.13) decouples from the others and the remaining three equations can be solved for the three unknowns, $\overline{V}$, $\overline{W}$, and $\overline{\Phi}$. Values of s are found by setting the determinant of the matrix equal to zero and finding the roots. This leads to a relation between $\overline{V}$, $\overline{W}$, and $\overline{\Phi}$ for each root, and hence, the solution to the problem. Numerical results will be shown shortly.

A.2.2 Approximate Elasticity Solutions

As a check and to better understand the piezoelectric effect, the constitutive equations and the elasticity solutions were simplified. The first simplification was to ignore equation (A.2) and assume that equation (A.1) represented the entire set of constitutive equations, i.e., that the electromechanical (equation (A.1)) and mechanoelectrical (equation (A.2)) effects were decoupled. The other assumptions were based on whether Problem I or Problem II is being considered.

A.2.2.1 Problem I

For Problem I, the electrostatic potential applied is the same on the top and the bottom of the plate. The electrostatic potential applied at x_3 = H/2 and −H/2 is thus given by

$$\phi_{x_3 = \frac{h}{2}, -\frac{h}{2}} = \phi_0 \sin\left(\frac{\pi x_2}{L}\right) \tag{A.14}$$

where, for numerical purposes, ϕ_0 is a constant.

It is further assumed that the only significant potential gradient in this problem is in the x_2 direction and is due to the applied harmonic electrostatic potential. With this assumption, the electric potential anywhere can be represented by

$$\phi(x_1, x_2, x_3) = \phi_0 \sin\left(\frac{\pi x_2}{L}\right) \tag{A.15}$$

From equation (A.4), then, $E_1 = E_3 = 0$.

A stress develops in the x_1 direction because there is no strain allowed in this direction ($\varepsilon_{11} = \partial u_1 / \partial x_1 = 0$, from equation (A.5)). In the other directions, using an analogy with thermal expansion, the remaining stresses are assumed to be zero:

$$\sigma_{22} = \sigma_{33} = \sigma_{23} = \sigma_{31} = \sigma_{12} = 0 \tag{A.16}$$

Applying these assumptions to equation (A.1), the following is obtained:

$$\begin{bmatrix} \sigma_{11} \\ 0 \\ 0 \\ 0 \\ 0 \\ 0 \end{bmatrix} = \begin{bmatrix} C_{1111} & C_{1122} & C_{1133} & 0 & 0 & 0 \\ C_{1122} & C_{2222} & C_{2233} & 0 & 0 & 0 \\ C_{1133} & C_{2233} & C_{3333} & 0 & 0 & 0 \\ 0 & 0 & 0 & C_{2323} & 0 & 0 \\ 0 & 0 & 0 & 0 & C_{3131} & 0 \\ 0 & 0 & 0 & 0 & 0 & C_{1212} \end{bmatrix} \begin{bmatrix} 0 \\ \varepsilon_{22} \\ \varepsilon_{33} \\ 2\varepsilon_{23} \\ 2\varepsilon_{31} \\ 2\varepsilon_{12} \end{bmatrix} - \begin{bmatrix} 0 & 0 & e_{311} \\ 0 & 0 & e_{322} \\ 0 & 0 & e_{333} \\ 0 & e_{223} & 0 \\ e_{113} & 0 & 0 \\ 0 & 0 & 0 \end{bmatrix} \begin{bmatrix} 0 \\ E_2 \\ 0 \end{bmatrix} \tag{A.17}$$

Extracting the fourth row,

$$0 = 2C_{2323}\varepsilon_{23} - e_{223}E_2 \tag{A.18}$$

so

$$\varepsilon_{23} = \frac{e_{223}}{2C_{2323}}E_2 \tag{A.19}$$

Using equations (A.4) and (A.15), the electric field strength in the x_2 direction is given by

$$E_2 = -\frac{\pi\phi_0}{L}\cos\left(\frac{\pi x_2}{L}\right) \tag{A.20}$$

so, substituting into equation (A.19), ε_{23} can be determined to be

$$\varepsilon_{23} = -\frac{\pi\phi_0}{L}\frac{e_{223}}{2C_{2323}}\cos\left(\frac{\pi x_2}{L}\right) \tag{A.21}$$

It is seen that ε_{23} is independent of x_3; that is, ε_{23} is constant thought the thickness. The second, third, fifth, and sixth rows of equation (A.17) show that

$$\begin{aligned} \varepsilon_{22} &= 0 \\ \varepsilon_{33} &= 0 \\ \varepsilon_{31} &= 0 \\ \varepsilon_{12} &= 0 \end{aligned} \tag{A.22}$$

Since $\varepsilon_{11} = 0$ from equation (A.5), the approximate elasticity solution shows there is only one nonzero strain, and it is uniform through the thickness of the plate. Numerical results from this approximate solution will be compared with the exact solution shortly.

A.2.2.2 Problem II

Problem II is similar to Problem I; the only difference is in the electrostatic-potential boundary conditions. Again, the potential on the bottom is given by

$$\phi_{x_3=-\frac{h}{2}} = \phi_0 \sin\left(\frac{\pi x_2}{L}\right) \tag{A.23}$$

but now the potential on $x_3 = H/2$ is of opposite sign and is given by

$$\phi_{x_3=\frac{h}{2}} = -\phi_0 \sin\left(\frac{\pi x_2}{L}\right) \tag{A.24}$$

Because there now is a large gradient through the thickness, the only potential gradient is now assumed to be E_3, i.e., it is assumed that

$$E_1 = E_2 = 0 \tag{A.25}$$

Again, because of equation (A.5), $\varepsilon_{11} = 0$, and it is assumed that equation (A.16) is valid. Using these assumptions, equation (A.1) now becomes

$$\begin{bmatrix} \sigma_{11} \\ 0 \\ 0 \\ 0 \\ 0 \\ 0 \end{bmatrix} = \begin{bmatrix} C_{1111} & C_{1122} & C_{1133} & 0 & 0 & 0 \\ C_{1122} & C_{2222} & C_{2233} & 0 & 0 & 0 \\ C_{1133} & C_{2233} & C_{3333} & 0 & 0 & 0 \\ 0 & 0 & 0 & C_{2323} & 0 & 0 \\ 0 & 0 & 0 & 0 & C_{3131} & 0 \\ 0 & 0 & 0 & 0 & 0 & C_{1212} \end{bmatrix} \begin{bmatrix} 0 \\ \varepsilon_{22} \\ \varepsilon_{33} \\ 2\varepsilon_{23} \\ 2\varepsilon_{31} \\ 2\varepsilon_{12} \end{bmatrix} - \begin{bmatrix} 0 & 0 & e_{311} \\ 0 & 0 & e_{322} \\ 0 & 0 & e_{333} \\ 0 & e_{223} & 0 \\ e_{113} & 0 & 0 \\ 0 & 0 & 0 \end{bmatrix} \begin{bmatrix} 0 \\ 0 \\ E_3 \end{bmatrix} \tag{A.26}$$

Equation (A.26) can be decoupled to give, in part,

$$\begin{bmatrix} \sigma_{11} \\ 0 \\ 0 \end{bmatrix} = \begin{bmatrix} C_{1111} & C_{1122} & C_{1133} \\ C_{1122} & C_{2222} & C_{2233} \\ C_{1133} & C_{2233} & C_{3333} \end{bmatrix} \begin{bmatrix} 0 \\ \varepsilon_{22} \\ \varepsilon_{33} \end{bmatrix} - \begin{bmatrix} 0 & 0 & e_{311} \\ 0 & 0 & e_{322} \\ 0 & 0 & e_{333} \end{bmatrix} \begin{bmatrix} 0 \\ 0 \\ E_3 \end{bmatrix} \tag{A.27}$$

Solving equation (A.27) for ε_{22} and ε_{33} results in

$$\varepsilon_{22} = \frac{(C_{2233}e_{333} - C_{3333}e_{322})E_3}{C_{2233}^2 - C_{2222}C_{3333}} \tag{A.28}$$

and

$$\varepsilon_{33} = -\frac{(C_{2222}e_{333} - C_{2233}e_{322})E_3}{C_{2233}^2 - C_{2222}C_{3333}} \tag{A.29}$$

The fourth, fifth, and sixth rows of equation (A.26) show that

$$\begin{aligned} \varepsilon_{23} &= 0 \\ \varepsilon_{31} &= 0 \\ \varepsilon_{12} &= 0 \end{aligned} \tag{A.30}$$

From equations (A.4), (A.23), and (A.24), the electric field strength is assumed to be

$$E_3 = \frac{2\phi_0}{h}\sin\left(\frac{\pi x_2}{L}\right) \tag{A.31}$$

i.e., the electric field strength is assumed to be constant through the thickness.

Relationships for the normal strains have been obtained in equations (A.28) and (A.29), but using the strain-displacement relations, the displacements may be obtained. The relevant strain-displacement relations are

$$\varepsilon_{22} = \frac{\partial u_2}{\partial x_2}$$
$$\varepsilon_{33} = \frac{\partial u_3}{\partial x_3} \tag{A.32}$$

Substituting for the strains on the left side of equations (A.28) and (A.29) and integrating, relations for the u_2 and u_3 displacements are obtained as

$$u_2(x_2, x_3) = \frac{2L}{\pi h}\frac{(C_{3333}e_{322} - C_{2233}e_{333})}{C_{2233}^2 - C_{2222}C_{3333}}\cos\left(\frac{\pi x_2}{L}\right) + f(x_3) \tag{A.33}$$

$$u_3(x_2, x_3) = \frac{2x_3}{h}\frac{(C_{2233}e_{322} - C_{2222}e_{333})}{C_{2233}^2 - C_{2222}C_{3333}}\sin\left(\frac{\pi x_2}{L}\right) + g(x_2) \tag{A.34}$$

The functions of integration, $f(x_3)$ and $g(x_2)$, can be eliminated. Because u_2 is taken to be zero at $x_2 = L/2$, as stipulated in equation (A.9), $f(x_3)$ must zero. The function of integration, $g(x_2)$, can be eliminated because the problem is symmetric in x_3 and along $x_3 = 0$, $u_3 = 0$. Results from this approximate solution will be compared with the exact solution to the problem shortly.

A.2.3 ABAQUS Finite-Element Solutions

The *ABAQUS* finite-element code was used to find a solution to both Problems I and II. The finite-element mesh that was used consisted of 30 piezoelectric, three-dimensional, 20-noded brick elements (C3D20E). The mesh used to model the geometry of Figure A.1 was three elements in the x_3 direction, one element in the x_1 direction, and 10 elements in the x_2 direction. The electric potential boundary conditions were met by specifying the proper voltage at all of the nodes on the top and bottom of the plate. Finite-element results will be compared with results from the exact and approximate solutions in the next section.

A.2.4 Comparison of Results for Problems I and II

Problems I and II were solved using each of the three aforementioned methods. The somewhat unrealistic dimensions of the plate were L = 1 m and H = 0.2 m. In addition, ϕ_0 = 1 V/m. These numerical values were chosen strictly for ease of computation. The material was assumed to be PZT-5A, a piezoceramic, and the material properties are given in Table A.1 (from [A.5]).

Table A.1: PZT-5A material properties used

Property (GPa)	Value	Property	Value
C_{1111}	99.201	e_{311} (C m^{-2})	−7.209
C_{2222}	99.201	e_{322} (C m^{-2})	−7.209
C_{3333}	86.856	e_{333} (C m^{-2})	15.118
C_{1122}	54.016	e_{223} (C m^{-2})	12.322
C_{1133}	50.778	e_{113} (C m^{-2})	12.322
C_{2233}	50.778	ϵ_{11} (10^{-10} F/m)	153.0
C_{2323}	21.100	ϵ_{22} (10^{-10} F/m)	153.0
C_{3131}	21.100	ϵ_{33} (10^{-10} F/m)	150.0
C_{1212}	22.593		

A.2.4.1 Problem I

A comparison of the results for Problem I is seen in Figures A.2, A.3, and A.4. Figures A.2 and A.3 show the u_3 and u_2 displacements for both *ABAQUS* and the elasticity solution; the displacements could not be found for Problem I using the approximate approach. Figure A.4 shows the engineering shear strains for each of the three solutions. It can be seen that each of these solution types gives very similar results, suggesting that each is a valid method for solving Problem I. Although the γ_{23} is not constant through the thickness for the *ABAQUS* and exact elasticity solutions, the variation of γ_{23} through the thickness is small, only about 5% for both solution types, as in the assumption in the approximate elasticity solution. Therefore, the approximations of Section A.2.2.1, given by equations (A.15) and (A.16), are valid.

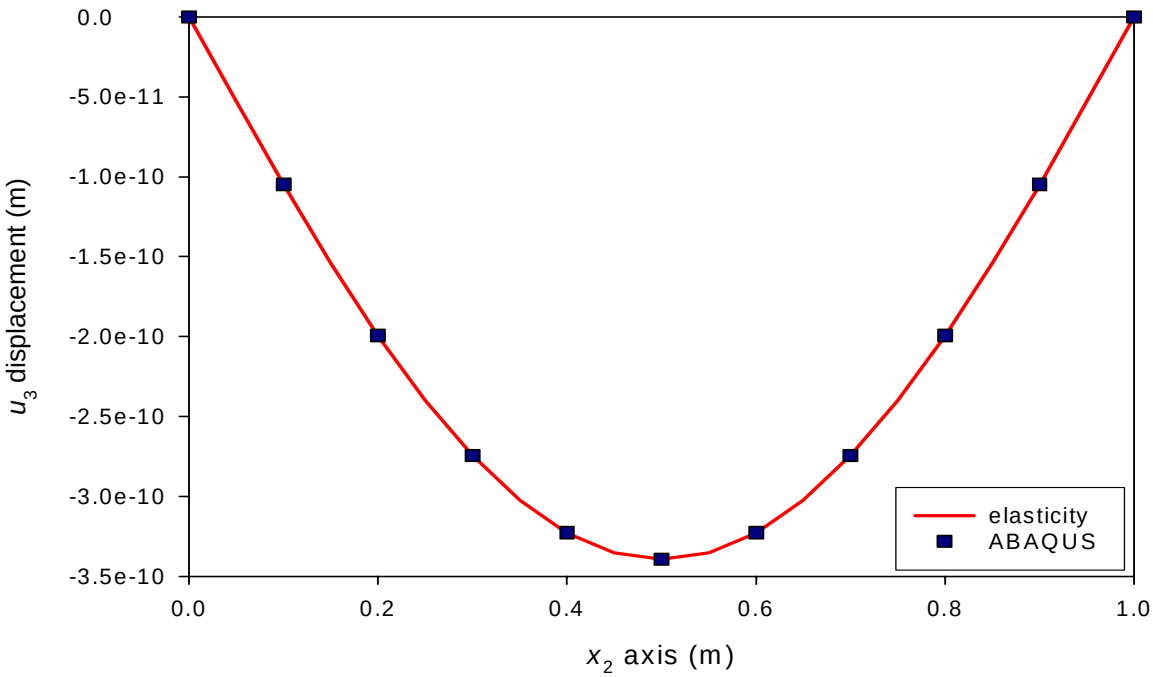

Figure A.2: u_3 displacement for the bottom of the plate, $x_3 = -H/2$, Problem I

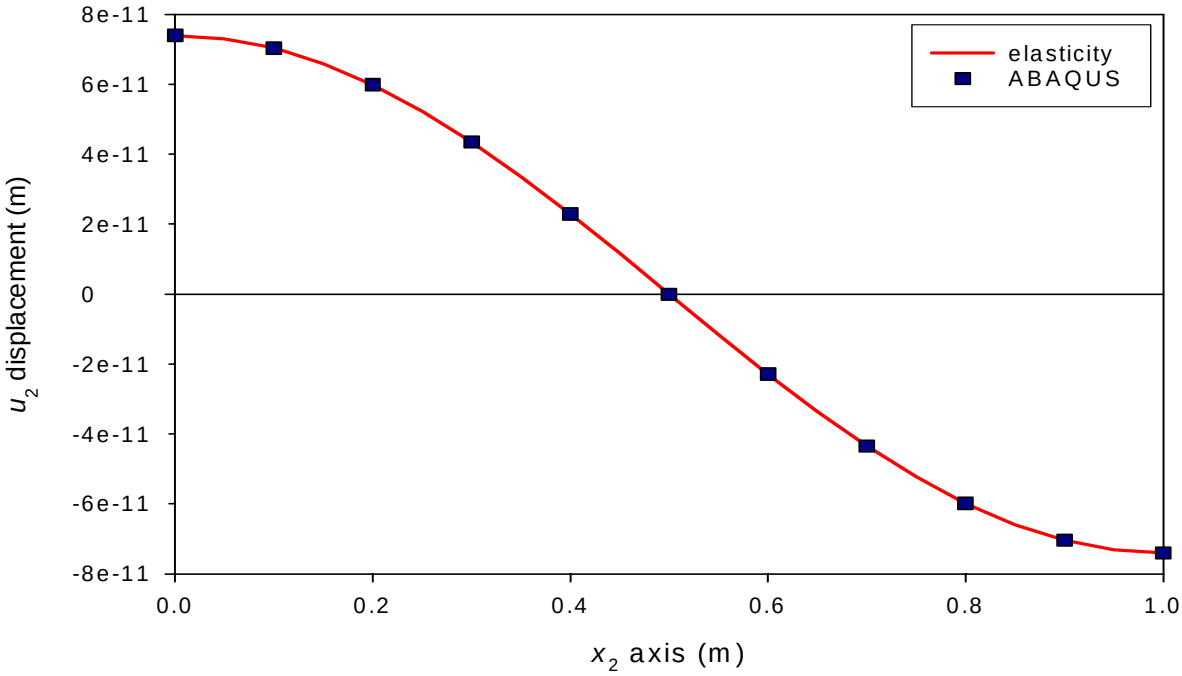

Figure A.3: u_2 displacement for the bottom of the plate, $x_3 = -H/2$, Problem I

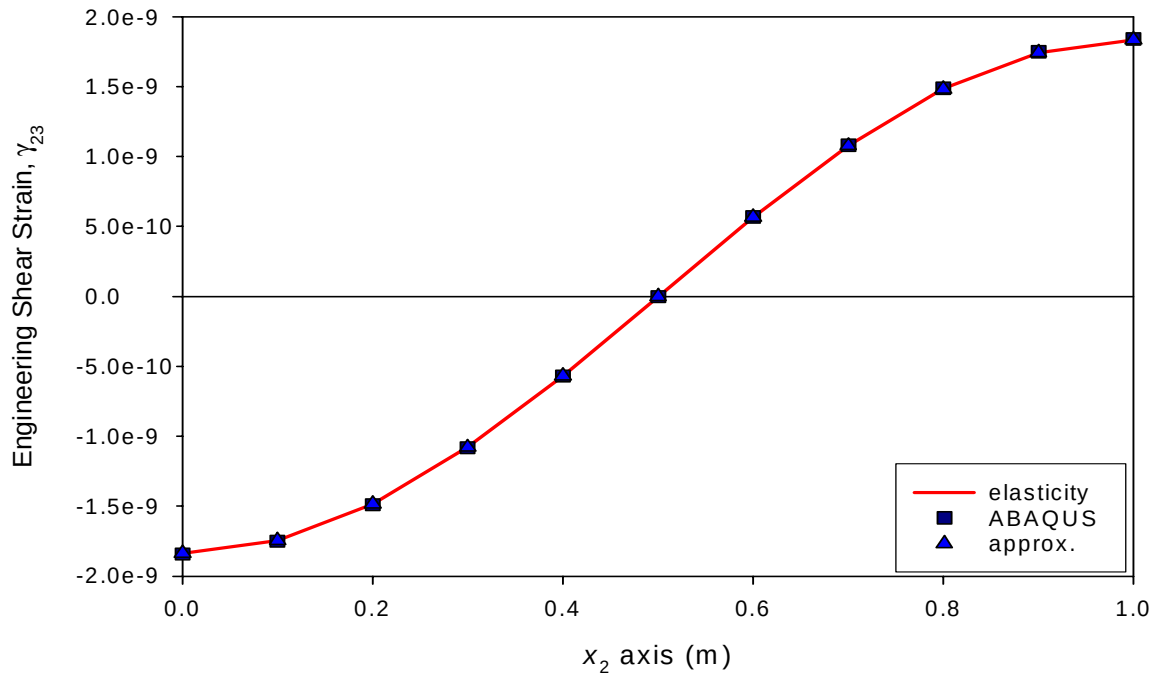

Figure A.4: Engineering shear strain for the bottom of the plate, $x_3 = -H/2$, Problem I

A.2.4.2 Problem II

A comparison of the results for Problem II is seen in Figures A.5, A.6, and A.7. Figures A.5 and A.6 show the u_3 and u_2 displacements for the *ABAQUS*, elasticity, and approximate solutions. Figure A.7 shows the engineering shear strains for the *ABAQUS* and elasticity solutions. It can be seen that these solution types give very similar results, suggesting that each is a valid method for solving Problem II. Therefore, the approximations of Section A.2.2.2, given by equations (A.16), (A.25), and (A.31), are valid.

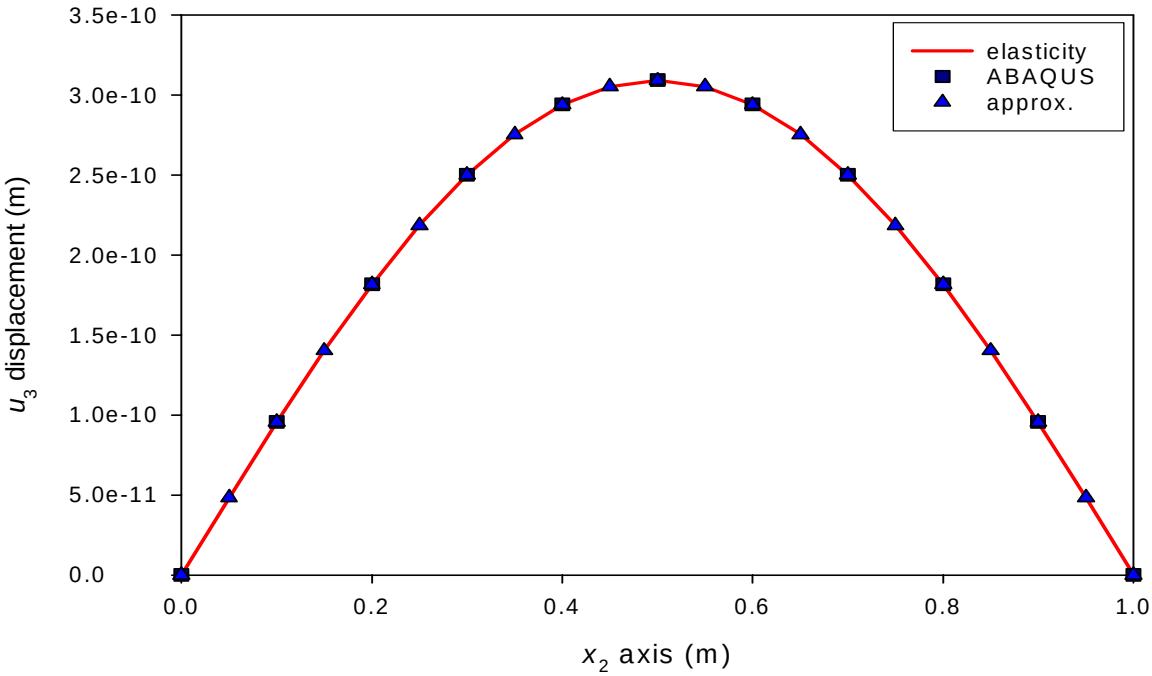

Figure A.5: u_3 displacement for the bottom of the plate, $x_3 = -H/2$, Problem II

A.3 Geometry II, Problems III and IV

A two-layer plate geometry is used to compare the three-dimensional elasticity and finite-element solutions with a two-dimensional plate solution. The geometry consists of a semi-infinite plate with two layers, as shown in Figure A.8. The top layer is PZT-5A and the bottom layer is graph-

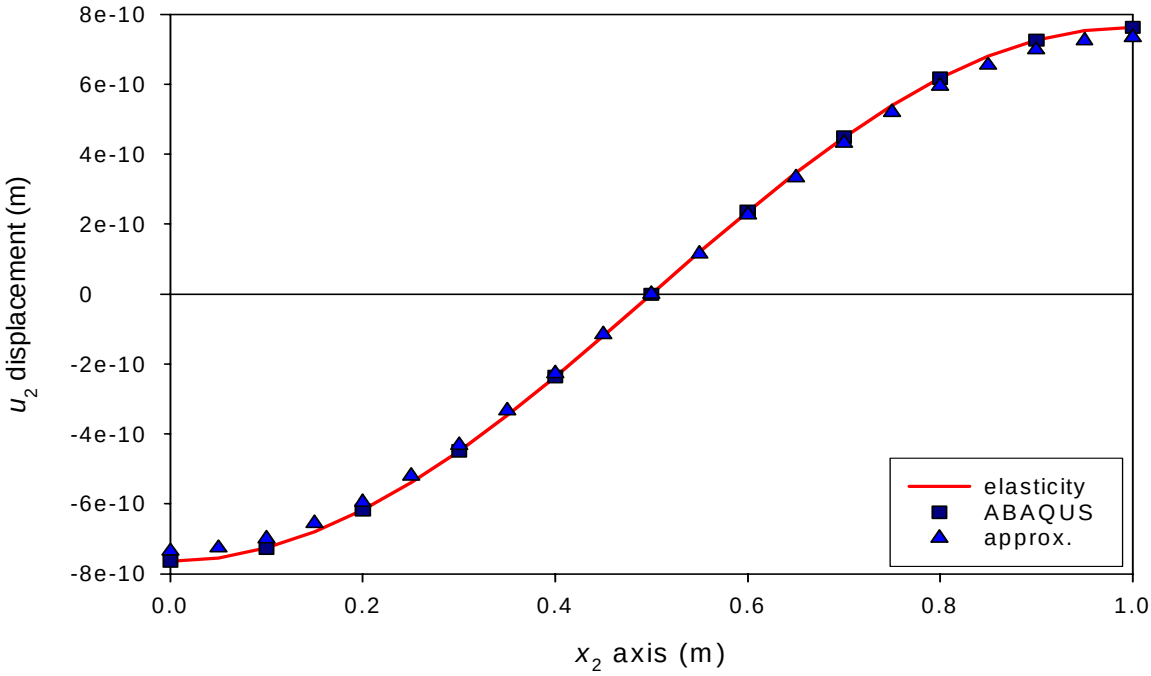

Figure A.6: u_2 displacement for the bottom of the plate, $x_3 = -H/2$, Problem II

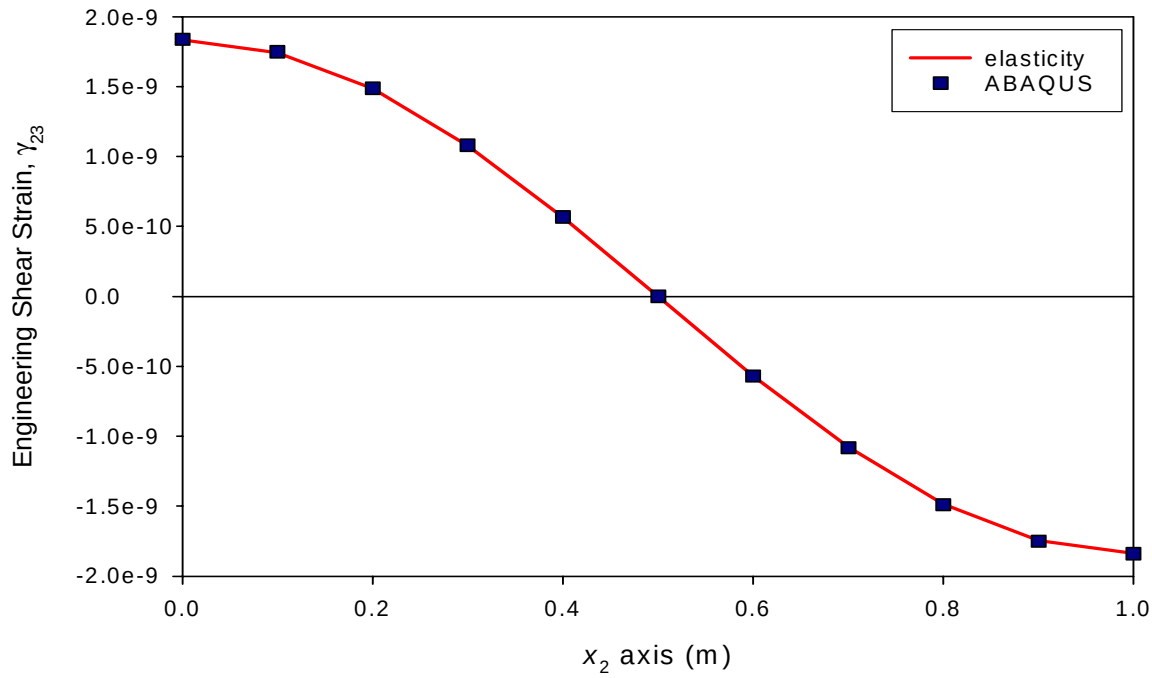

Figure A.7: Engineering shear strain for the bottom of the plate, $x_3 = -H/2$, Problem II

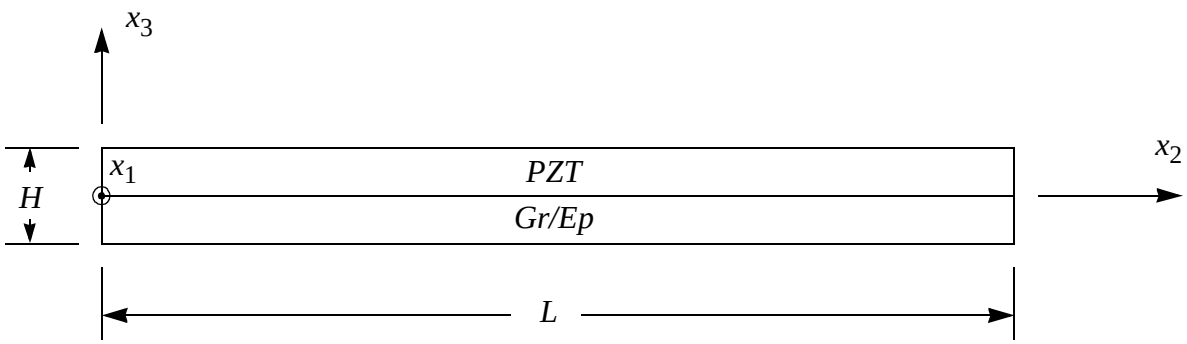

Figure A.8: Geometry II, geometry of two-layer semi-infinite plate

ite/epoxy (Gr/Ep). The material properties of the PZT are given in Table A.1, while the material properties of the graphite/epoxy layer are given in Table A.2. As with the problems in Section A.2, an electrostatic potential, harmonically distributed, is applied to the top and bottom of the piezoceramic layer and the problem is infinite in the x_1 direction and independent of position along the x_1 axis. Equations (A.6) – (A.8), from Section A.2, also hold for this problem.

Table A.2: Graphite/epoxy material properties for Problems III and IV

Property (GPa)	Value
C_{1111}	183.44
C_{2222}	11.662
C_{3333}	11.662
C_{1122}	4.363
C_{1133}	4.363
C_{2233}	3.918
C_{2323}	2.870
C_{3131}	7.170
C_{1212}	7.170

A.3.1 The Two-Dimensional Solutions

A discussion of classical lamination theory and the plate assumptions is given in Hyer [A.6]. The assumption that allows for the two-dimensional simplification of this problem is that the electric potential gradient through the thickness of the piezoceramic is assumed to vary linearly with x_3. The effective piezoelectric strains may thus be represented by

$$\begin{aligned} \varepsilon_1^E &= d_{31}\frac{\partial \phi}{\partial x_3} \\ \varepsilon_2^E &= d_{32}\frac{\partial \phi}{\partial x_3} \end{aligned} \tag{A.35}$$

where d_{31} and d_{32} are the piezoelectric constants, the derivation of which may be found in Appendix B, and $\partial\phi/\partial x_3$ is thus assumed to be constant. Because $\partial\phi/\partial x_3$ is assumed constant, the induced strains are just a function of the in-plane directions. Using exact three-dimensional elasticity analyses, Ray et al. [A.7,A.8] found that, for thin, single-layer plates, the electric potential varies linearly through the thickness of the plate. This assumption was also employed for Problem II in Section A.2.2.2 with equation (A.31) and was shown in Figures A.5 and A.6 to give answers very close to the exact solution.

The midplane strains are given by the linear strain-displacement relations:

$$\begin{aligned} \varepsilon_1^\circ &= \frac{\partial u_1^\circ}{\partial x_1} \\ \varepsilon_2^\circ &= \frac{\partial u_2^\circ}{\partial x_2} \\ \gamma_{12}^\circ &= \frac{\partial u_1^\circ}{\partial x_2} + \frac{\partial u_2^\circ}{\partial x_1} \end{aligned} \tag{A.36}$$

The displacement and electric potential fields are assumed to be of the form

$$\begin{aligned} u_1^\circ &= 0 \\ u_2^\circ &= \overline{V}\cos\frac{\pi x_2}{L} \\ u_3^\circ &= \overline{W}\sin\frac{\pi x_2}{L} \\ \phi &= \overline{\Phi}\left(\frac{4x_3}{H}-1\right)\sin\frac{\pi x_2}{L} \end{aligned} \tag{A.37}$$

where $\overline{V}$ and $\overline{W}$ are to-be-determined constants, and $\overline{\Phi}$ is a known constant. Note that $\phi = 0$ in the graphite/epoxy layer. Equation (A.37) is similar, in spirit, to equation (A.10) and was chosen to satisfy the boundary conditions. The two-dimensional equilibrium equations for a plate with no external load applied are

$$\begin{aligned} \frac{\partial N_1}{\partial x_1}+\frac{\partial N_{12}}{\partial x_2} &= 0 \\ \frac{\partial N_{12}}{\partial x_1}+\frac{\partial N_2}{\partial x_2} &= 0 \\ \frac{\partial^2 M_1}{\partial {x_1}^2}+2\frac{\partial^2 M_{12}}{\partial x_1 \partial x_2}+\frac{\partial^2 M_2}{\partial {x_2}^2} &= 0 \end{aligned} \tag{A.38}$$

where the N_{ij}s and M_{ij}s are the force and moment resultants and are defined as usual (see Hyer [A.6]). The first of the equilibrium equations is identically satisfied, so the last two equilibrium equations are solved simultaneously to find $\overline{V}$ and $\overline{W}$, which allow the displacements to be found anywhere on the plate.

A.3.2 Comparison of Results for Problems III and IV

Two different plate geometries, Problem III and Problem IV, were used to compare the two- and three-dimensional solution strategies. These problems were identical in all aspects, except for the plate thickness: 0.4 m for Problem III and 0.1 m thick for Problem IV. The common quantities are L = 1.0 m, $\phi = 1.0 \sin(\pi x_2/L)$ V along $x_3 = H/2$, and $\phi = -1.0 \sin(\pi x_2/L)$ V along $x_3 = 0$. Thus, based on the magnitudes of H and L, Problem III considers a plate that could be considered thick, while Problem IV considers a thinner plate.

A.3.2.1 Problem III

Plots of the u_2 and u_3 displacements are seen in Figures A.9 and A.10. It is seen that there is excellent agreement between the two three-dimensional solutions, namely the elasticity and finite-element solutions. However, the agreement between the two-dimensional solution and the three-dimensional solutions is not as good.

A.3.2.2 Problem IV

Figures A.11 and A.12 show the u_2 and u_3 displacements for Problem IV. Again, the agreement is better between the two three-dimensional solutions. As expected, in this problem, the two-dimensional solution agrees with the three-dimensional solutions better than the agreement seen in Problem III. However, the primary lesson to be learned is that for thin plates, it is reasonable to assume that the electromechanical (equation (A.1)) and mechanoelectrical (equation (A.2)) effects were decoupled (i.e., one can ignore equation (A.2) when using thin piezoelectrics as actuators) and that the electric field strength is constant through the thickness. Thus, for thin plates, the strain effects, in equation (A.1), due to the electric field can be modeled analogously to thermal expansion strain-effects.

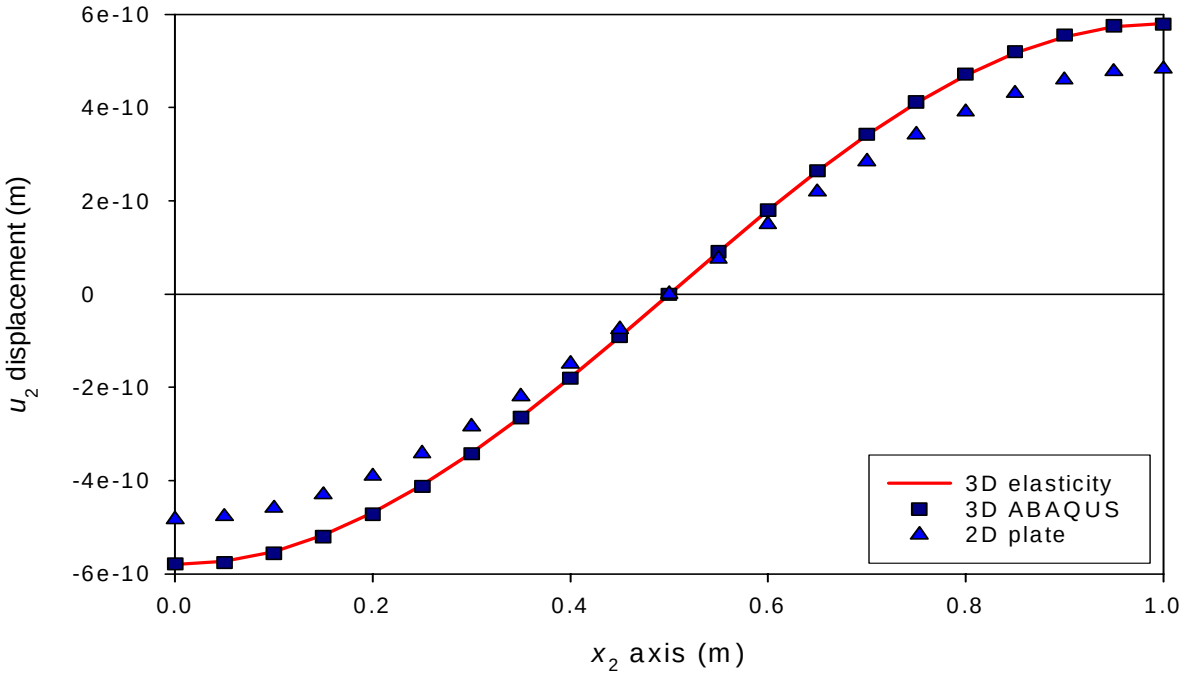

Figure A.9: u_2 displacement for the middle of the plate, $x_3 = 0$, Problem III

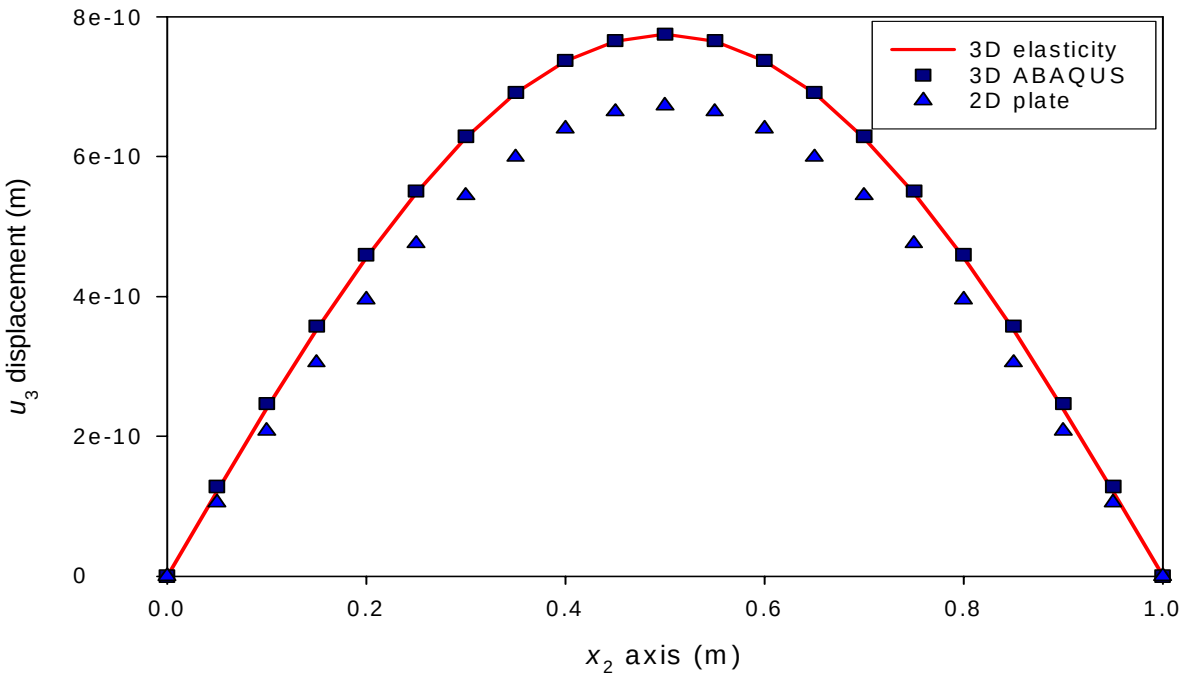

Figure A.10: u_3 displacement for the middle of the plate, $x_3 = 0$, Problem III

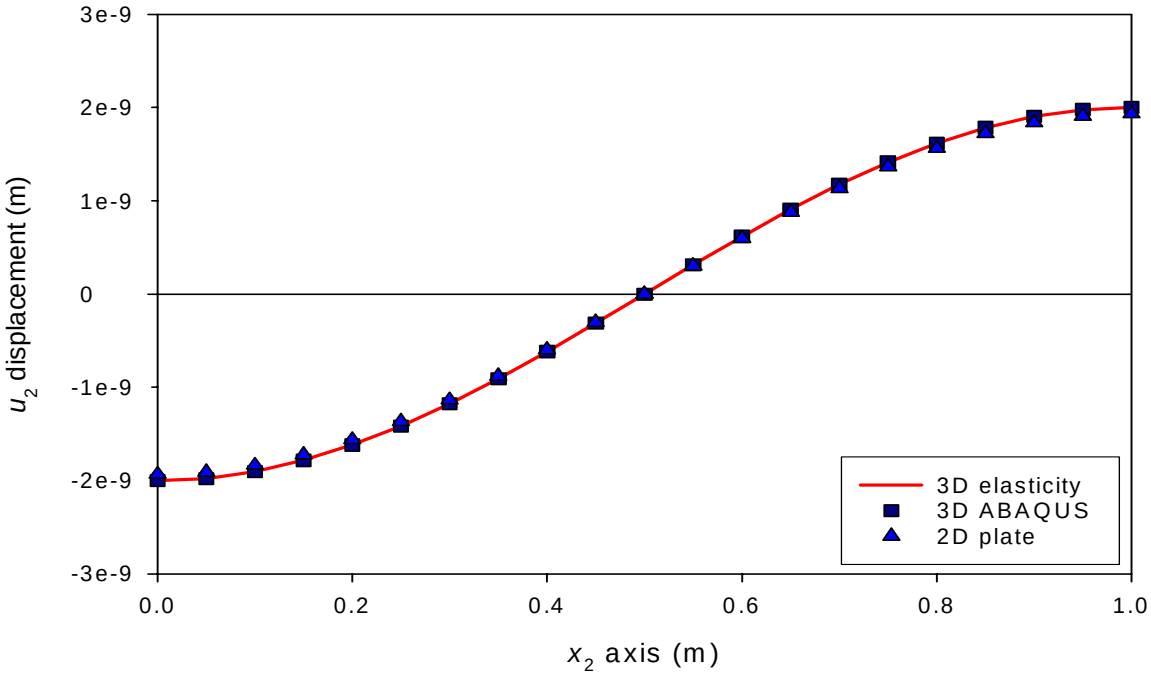

Figure A.11: u_2 displacement for the middle of the plate, x_3 = 0, Problem IV

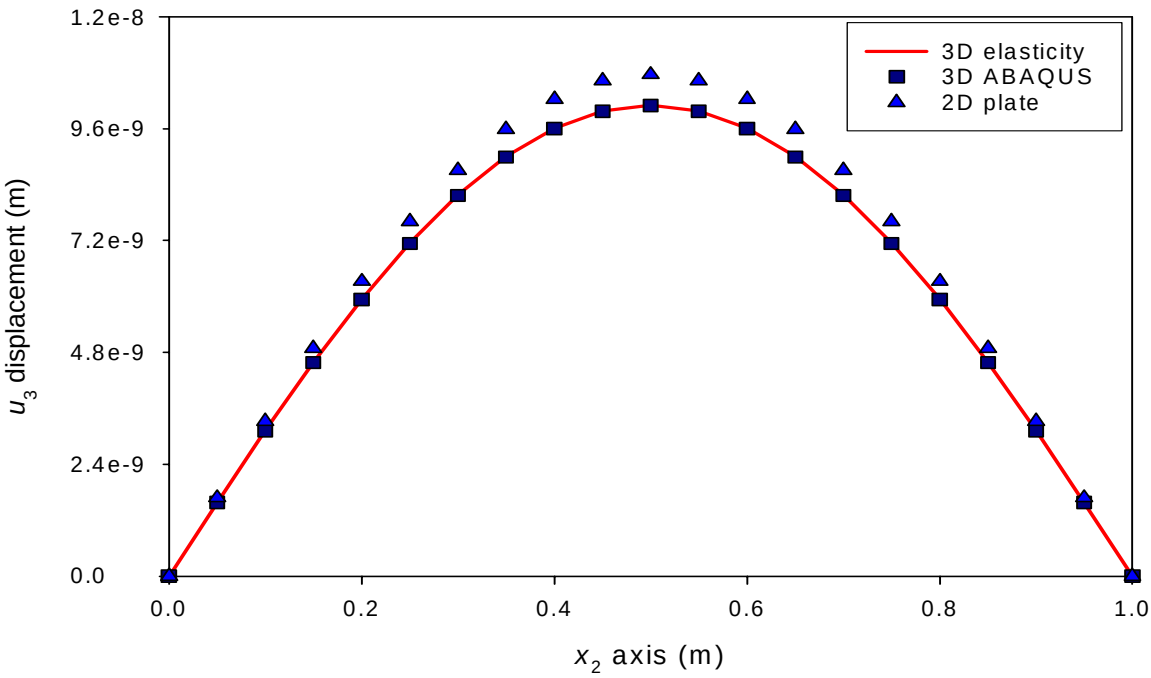

Figure A.12: u_3 displacement for the middle of the plate, x_3 = 0, Problem IV

A.4 References

A.1. *ABAQUS Theory Manual, Version 5.8*, Hibbitt, Karlsson, & Sorenson, Inc., 1998.

A.2. Tiersten, H. F. *Linear Piezoelectric Plate Vibrations: Elements of the Linear Theory of Piezoelectricity and the Vibrations of Piezoelectric Plates*, Plenum Press, New York, 1969.

A.3. Heyliger, P. "Exact Solutions for Simply Supported Laminated Piezoelectric Plates," *Journal of Applied Mechanics*, Vol. 64, 1997, pp. 299–306.

A.4. Heyliger, P. and Brooks, S. "Exact Solutions for Laminated Piezoelectric Plates in Cylindrical Bending," *Journal of Applied Mechanics*, Vol. 63, Dec. 1996, pp. 903–910.

A.5. Vel, S. S. and Batra, R. C. "Three-Dimensional Analytical Solutions for Hybrid Multilayered Piezoelectric Plates", *Journal of Applied Mechanics*, Vol. 67, No. 3, pp. 558–567, 2000.

A.6. Hyer, M. W. *Stress Analysis of Fiber-Reinforced Composite Materials*. New York, NY: McGraw-Hill, 1998.

A.7. Ray, M. C., Rao, K. M., and Samanta, B. "Exact Analysis of Coupled Electroelastic Behavior of a Piezoelectric Plate Under Cylindrical Bending," *Computers and Structures*, Vol. 45, 1992, pp. 667–677.

A.8. Ray, M. C., Rao, K. M., and Samanta, B. "Exact Solution for Static Analysis of Intelligent Structures Under Cylindrical Bending," *Computers and Structures*, Vol. 47, 1993, pp. 1031–1042.

Appendix B Derivation of Two-Dimensional Piezoelectric Constants

In this appendix, the two-dimensional piezoelectric constants, d_{31} and d_{32}, are derived from the three-dimensional piezoelectric constitutive equations.

B.1 Derivation from Three-Dimensional Equations

The three-dimensional piezoelectric electromechanical equation for a material poled in the 3 direction is

$$\begin{bmatrix} \sigma_{11} \\ \sigma_{22} \\ \sigma_{33} \\ \sigma_{23} \\ \sigma_{31} \\ \sigma_{12} \end{bmatrix} = \begin{bmatrix} C_{1111} & C_{1122} & C_{1133} & 0 & 0 & 0 \\ C_{1122} & C_{2222} & C_{2233} & 0 & 0 & 0 \\ C_{1133} & C_{2233} & C_{3333} & 0 & 0 & 0 \\ 0 & 0 & 0 & C_{2323} & 0 & 0 \\ 0 & 0 & 0 & 0 & C_{3131} & 0 \\ 0 & 0 & 0 & 0 & 0 & C_{1212} \end{bmatrix} \begin{bmatrix} \varepsilon_{11} \\ \varepsilon_{22} \\ \varepsilon_{33} \\ 2\varepsilon_{23} \\ 2\varepsilon_{31} \\ 2\varepsilon_{12} \end{bmatrix} - \begin{bmatrix} 0 & 0 & e_{311} \\ 0 & 0 & e_{322} \\ 0 & 0 & e_{333} \\ 0 & e_{223} & 0 \\ e_{113} & 0 & 0 \\ 0 & 0 & 0 \end{bmatrix} \begin{bmatrix} E_1 \\ E_2 \\ E_3 \end{bmatrix} \qquad \text{(B.1)}$$

where the σ_{ij} are the stresses, ε_{ij} are the strains, C_{ijkl} are the stiffnesses, the e_{ijk} are the piezoelectric coefficients, and E_{ij} are the components of the electric field. Equation B.1 can be used to derive the piezoelectric constants which are used in the simplified two-dimensional plate equations. This appendix will cover the derivation of these piezoelectric constants. The plane stress assumption ($\sigma_{33} = \sigma_{23} = \sigma_{31} = 0$) is used to simplify equation B.1:

$$\begin{bmatrix}\sigma_{11}\\ \sigma_{22}\\ 0\\ 0\\ 0\\ \sigma_{12}\end{bmatrix} = \begin{bmatrix}C_{1111} & C_{1122} & C_{1133} & 0 & 0 & 0\\ C_{1122} & C_{2222} & C_{2233} & 0 & 0 & 0\\ C_{1133} & C_{2233} & C_{3333} & 0 & 0 & 0\\ 0 & 0 & 0 & C_{2323} & 0 & 0\\ 0 & 0 & 0 & 0 & C_{3131} & 0\\ 0 & 0 & 0 & 0 & 0 & C_{1212}\end{bmatrix}\begin{bmatrix}\varepsilon_{11}\\ \varepsilon_{22}\\ \varepsilon_{33}\\ 2\varepsilon_{23}\\ 2\varepsilon_{31}\\ 2\varepsilon_{12}\end{bmatrix} - \begin{bmatrix}0 & 0 & e_{311}\\ 0 & 0 & e_{322}\\ 0 & 0 & e_{333}\\ 0 & e_{223} & 0\\ e_{113} & 0 & 0\\ 0 & 0 & 0\end{bmatrix}\begin{bmatrix}E_1\\ E_2\\ E_3\end{bmatrix} \tag{B.2}$$

Equation B.2 can be reduced to a series of three equations by using the third row of equation B.2 to solve for ε_{33}:

$$\varepsilon_{33} = -\frac{1}{C_{3333}}(C_{1133}\varepsilon_{11} + C_{2233}\varepsilon_{22} - e_{333}E_3) \tag{B.3}$$

Noting that, due to the Kirchhoff assumption employed in plate theory, $\varepsilon_{23} = \varepsilon_{31} = 0$, and considering only a through-thickness electric field ($E_1 = E_2 = 0$), the reduced equations can be written as

$$\begin{bmatrix}\sigma_{11}\\ \sigma_{22}\\ \sigma_{12}\end{bmatrix} = \begin{bmatrix}Q_{11} & Q_{12} & 0\\ Q_{12} & Q_{22} & 0\\ 0 & 0 & Q_{66}\end{bmatrix}\begin{bmatrix}\varepsilon_{11}\\ \varepsilon_{22}\\ 2\varepsilon_{12}\end{bmatrix} - \begin{bmatrix}b_{31}\\ b_{32}\\ b_{36}\end{bmatrix}\begin{bmatrix}E_3\end{bmatrix} \tag{B.4}$$

where the Q_{ij}s are the reduced stiffnesses and the b_{ij}s are reduced piezoelectric coefficients and are given by

$$\begin{aligned} Q_{11} &= C_{1111} - \frac{C_{1133}^2}{C_{3333}} \\ Q_{12} &= C_{1122} - \frac{C_{1133}C_{2233}}{C_{3333}} \\ Q_{22} &= C_{2222} - \frac{C_{2233}^2}{C_{3333}} \\ Q_{66} &= C_{1212} \end{aligned} \tag{B.5}$$

and

$$\begin{aligned} b_{31} &= e_{311} - \frac{C_{1133}}{C_{3333}} e_{333} \\ b_{32} &= e_{322} - \frac{C_{2233}}{C_{3333}} e_{333} \\ b_{36} &= 0 \end{aligned} \tag{B.6}$$

To find the two-dimensional so-called piezoelectric constants, the d_{ij}s, the terms on the right hand side of equation B.4 are redefined so equation B.4 is of the form

$$\begin{bmatrix} \sigma_{11} \\ \sigma_{22} \\ \sigma_{12} \end{bmatrix} = \begin{bmatrix} Q_{11} & Q_{12} & 0 \\ Q_{12} & Q_{22} & 0 \\ 0 & 0 & Q_{66} \end{bmatrix} \begin{bmatrix} \varepsilon_{11} - d_{31}E_3 \\ \varepsilon_{22} - d_{32}E_3 \\ 2\varepsilon_{12} \end{bmatrix} \tag{B.7}$$

where the d_{ij}s are given by

$$d_{31} = \frac{b_{32}Q_{12} - b_{31}Q_{22}}{Q_{12}^2 - Q_{11}Q_{22}}$$
$$d_{32} = -\frac{b_{32}Q_{11} - b_{31}Q_{12}}{Q_{12}^2 - Q_{11}Q_{22}} \quad \text{(B.8)}$$

B.2 Numerical Example

Using the properties for PZT-5A obtained from Vel and Batra [B.1] and shown in Table B.1, the piezoelectric constants were found to be $d_{31} = d_{32} = -171 \times 10^{-12}$ m/V, which is what Morgon Matroc, Inc., a manufacturer, gives [[B.2]].

Table B.1: PZT-5A material properties used

Property (GPa)	Value	Property	Value
C_{1111}	99.201	e_{311} (C m^{-2})	−7.209
C_{2222}	99.201	e_{322} (C m^{-2})	−7.209
C_{3333}	86.856	e_{333} (C m^{-2})	15.118
C_{1122}	54.016	e_{223} (C m^{-2})	12.322
C_{1133}	50.778	e_{113} (C m^{-2})	12.322
C_{2233}	50.778	ϵ_{11} (10^{-10} F/m)	153.0
C_{2323}	21.100	ϵ_{22} (10^{-10} F/m)	153.0
C_{3131}	21.100	ϵ_{33} (10^{-10} F/m)	150.0
C_{1212}	22.593		

B.3 References

B.1. Vel, S. S. and Batra, R. C. “Three-Dimensional Analytical Solutions for Hybrid Multilayered Piezoelectric Plates”, *Journal of Applied Mechanics*, Vol. 67, No. 3, pp. 558–567, 2000.

B.2. Morgon Matroc, Inc., product literature.

Appendix C Summary of All Snap-Through Test Results

In this appendix, the strain vs. voltage relations measured during all testing are shown. Shown first are the relations from the experiments where the laminate was hanging from the strain gage wire. Shown second are the relations from the experiments where the laminate was lying on a table with the actuator facing up. Finally, the relations from the experiments where the laminate was lying on a table with the actuator facing down are shown. Table C.1 gives a summary of all the experiments. During all the experiments where the laminate was hanging, the laminate

Table C.1: Summary of all experimental tests

Test Number	Maximum Voltage (V)	Number of Snapping Events	Voltages of Snapping Events (V)	*Hanging* (H), MFC Facing *Up* (U), *Down* (D)
hang1	2012	1	1773	H
hang2	1704	1	1665	H
hang3	1768	1	1714	H
hang4	1704	1	1685	H
hang5	1636	1	1640	H
hang6	1704	1	1694	H
up1	2065	1*	1729	U
up2	2900	3	1919 2891 1631**	U
up3	2905	3	1758 2632 1650**	U
up4	2002	1*	1875	U

Table C.1: Summary of all experimental tests

Test Number	Maximum Voltage (V)	Number of Snapping Events	Voltages of Snapping Events (V)	*Hanging* (H), MFC Facing *Up* (U), *Down* (D)
up5	2612	2	1631 2017	U
up6	2964	3	1895 2471 2075**	U
up7	3565	3	1773 2451 1509**	U
up8	3071	3	1670 2441 1650**	U
down1	2114	2	1621 2105	D
down2	1489	1	1484	D
down3	1939	1	1587	D
down4	2046	1*	1650	D
down5	2012	1*	1597	D
down6	2637	2	1743 2456	D
down7	2373	2	1675 2368	D
down8	2227	2	1685 2153	D
down9	1699	1	1655	D
down10	1733	1	1675	D
down11	1680	1	1670	D
down12	1533	1	1523	D
down13	1582	1	1563	D

*Incomplete snap through
**Snap through while decreasing voltage

snapped as intended, with only one snapping event occurring while the voltage was being increased. This was not the case with the experiments where the laminate was lying on a table. When the laminate was lying on a table with the actuator up, up to three snapping events occurred and sometimes complete snap through was not realized. The incomplete snapping events consisted of one or perhaps two corners snapping and reversing curvature, while the remainder of the laminate remained in its original configuration. Often, partial snap through occurred as the voltage was being increased, and as the voltage was being decreased, complete snap through occurred. When the laminate was lying on a table with the actuator down, up to two snapping events occurred, and sometimes complete snap through was not achieved.

C.1 Laminate Hanging

Figure C.1 shows pictures of the laminate hanging from the strain gage wire; this was the position for the hanging experiments. Figures C.2 – C.7 are the strain versus applied voltage curves for these hanging experiments. Although the strain vs. voltage relation shown in Figure C.6 may appear to represent a partial snapping event, in fact, there was only one snapping event; the frequency of the data acquisition was not fast enough to capture the initiation of snap-through.

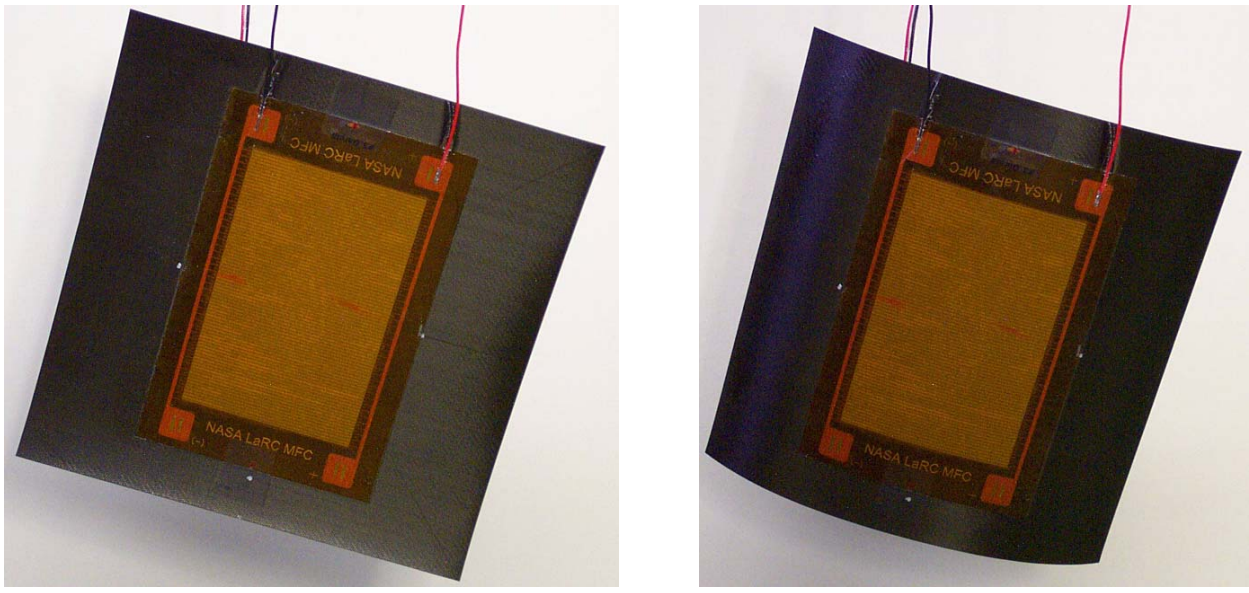

Figure C.1: Pictures of experiment where laminate was hanging

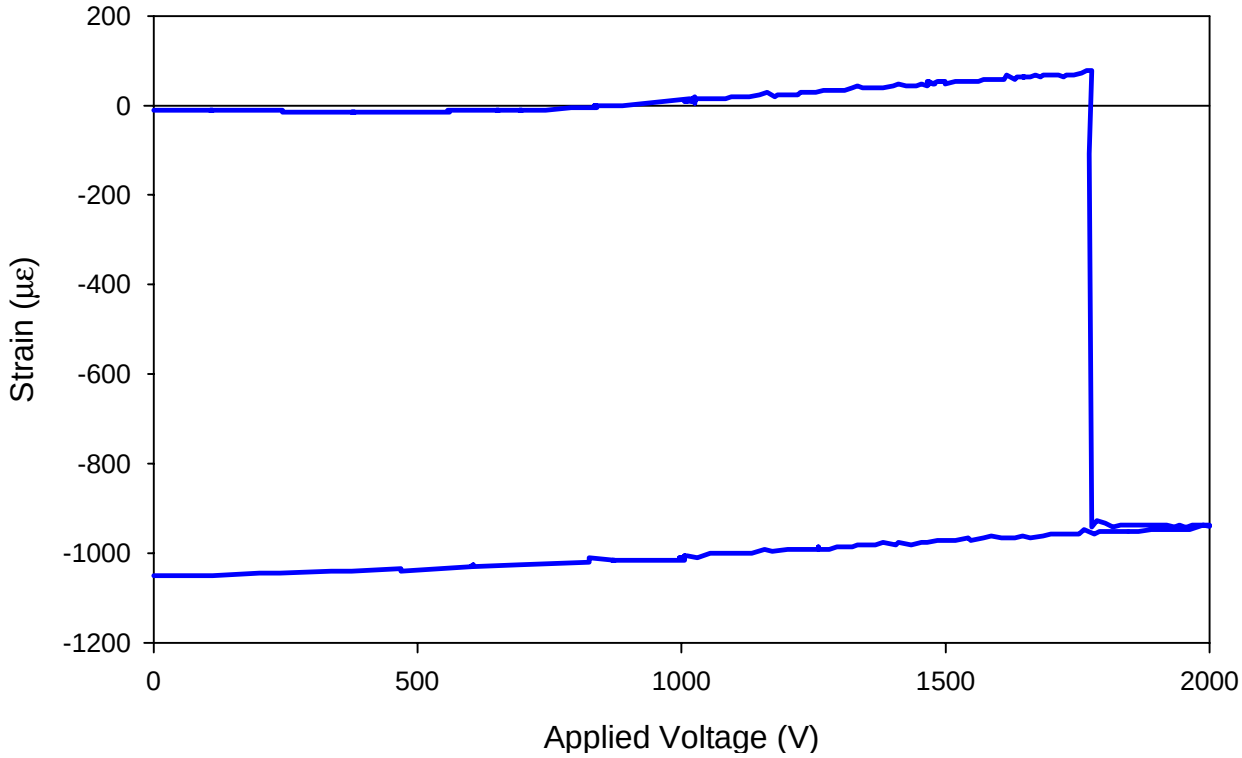

Figure C.2: Strain vs. applied voltage for test hang1

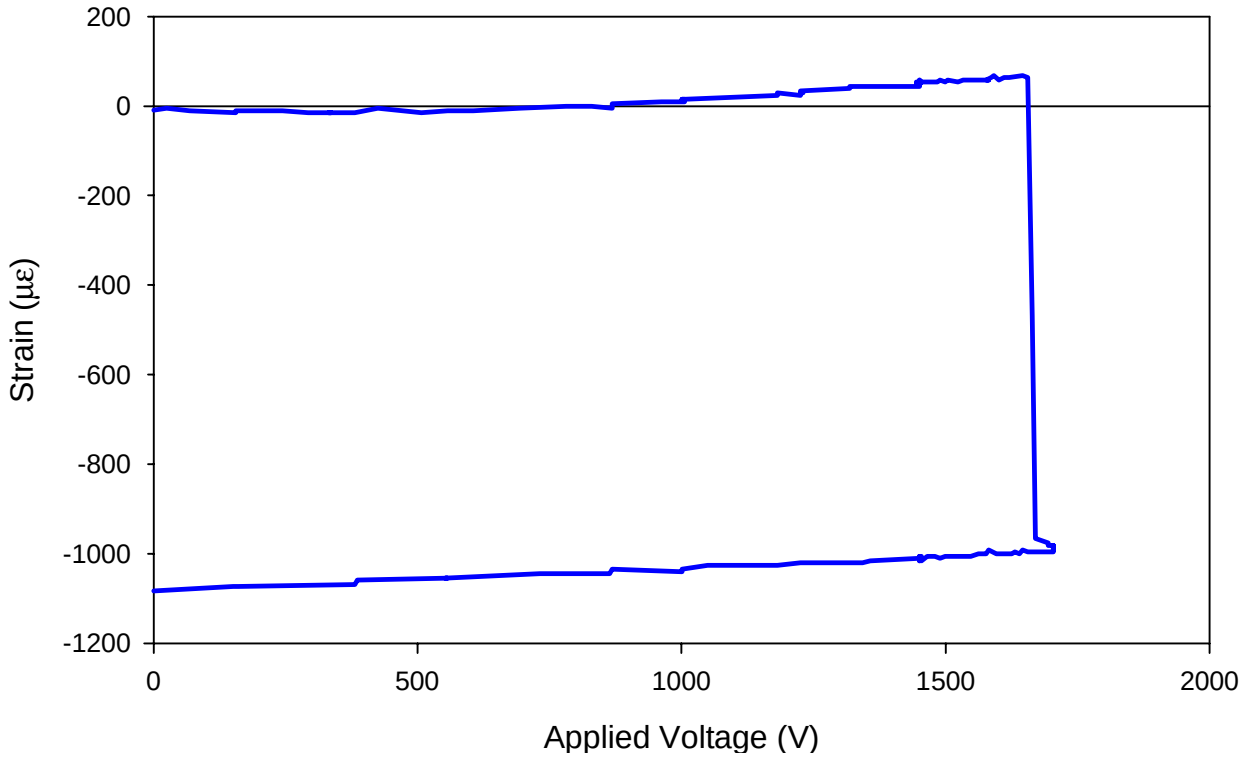

Figure C.3: Strain vs. applied voltage for test hang2

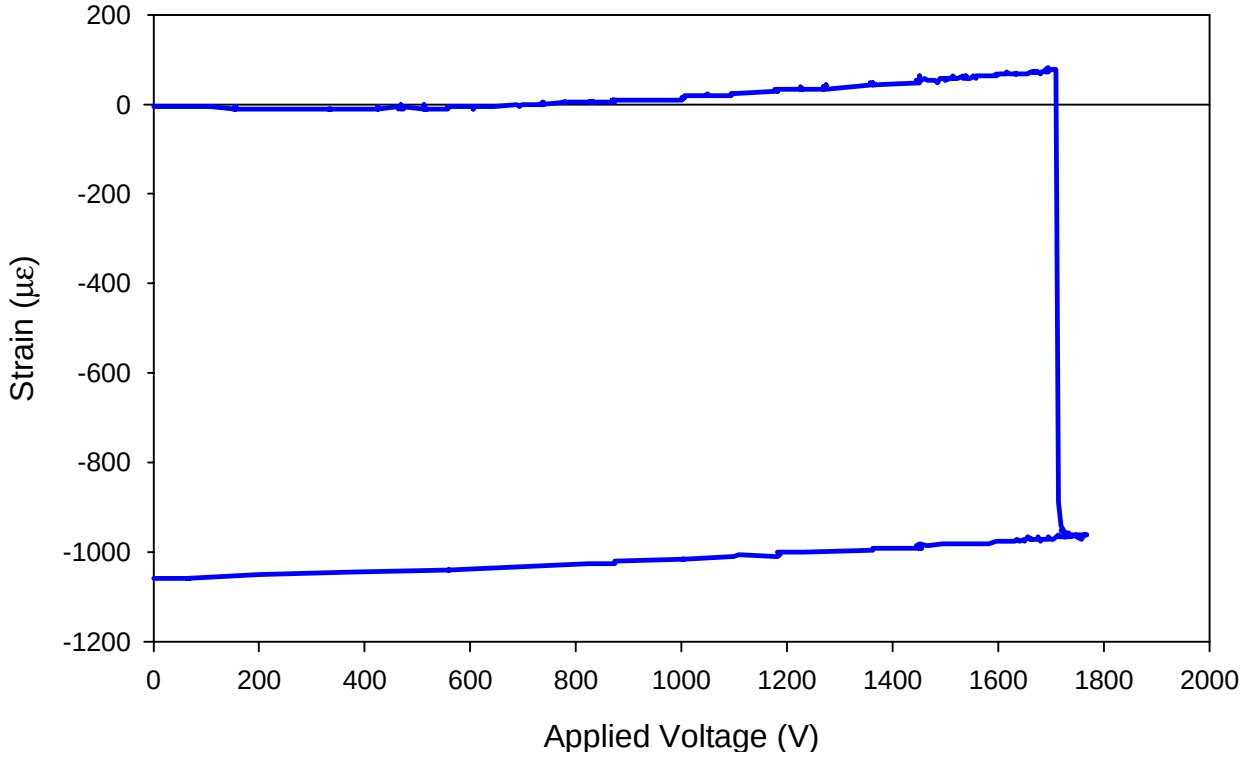

Figure C.4: Strain vs. applied voltage for test hang3

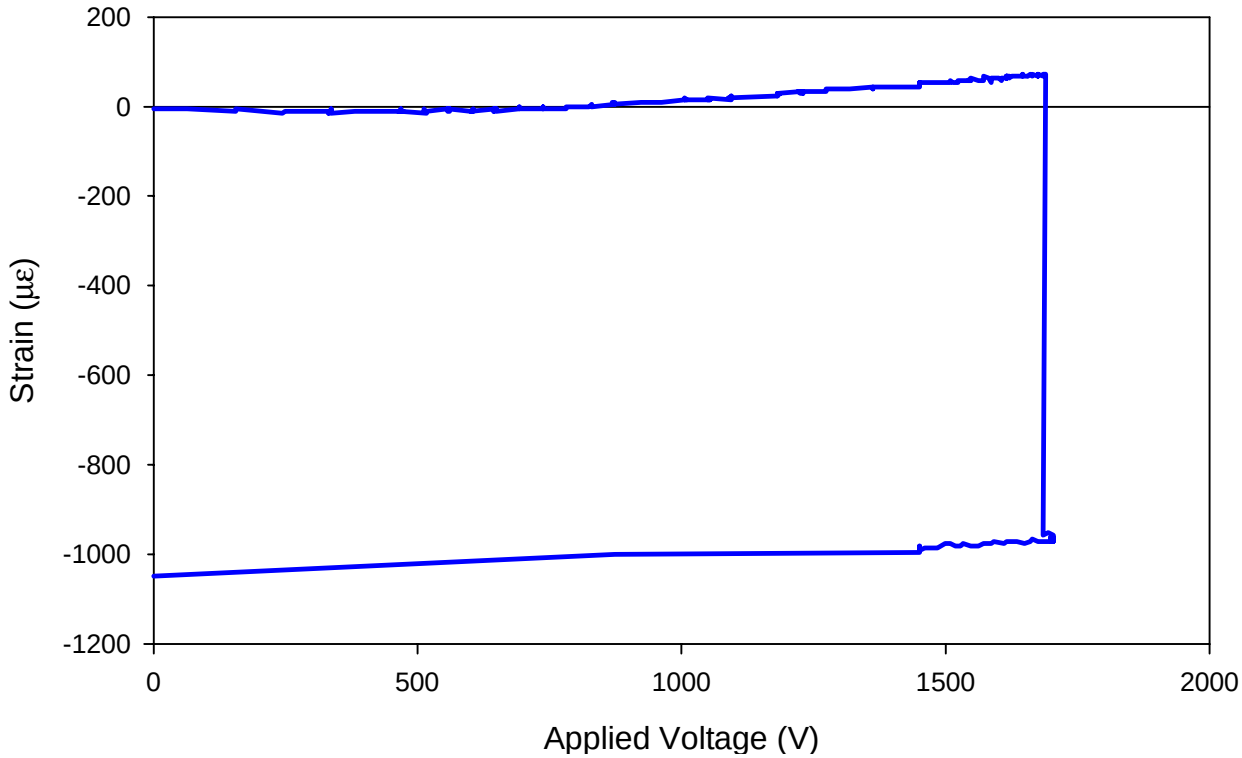

Figure C.5: Strain vs. applied voltage for test hang4

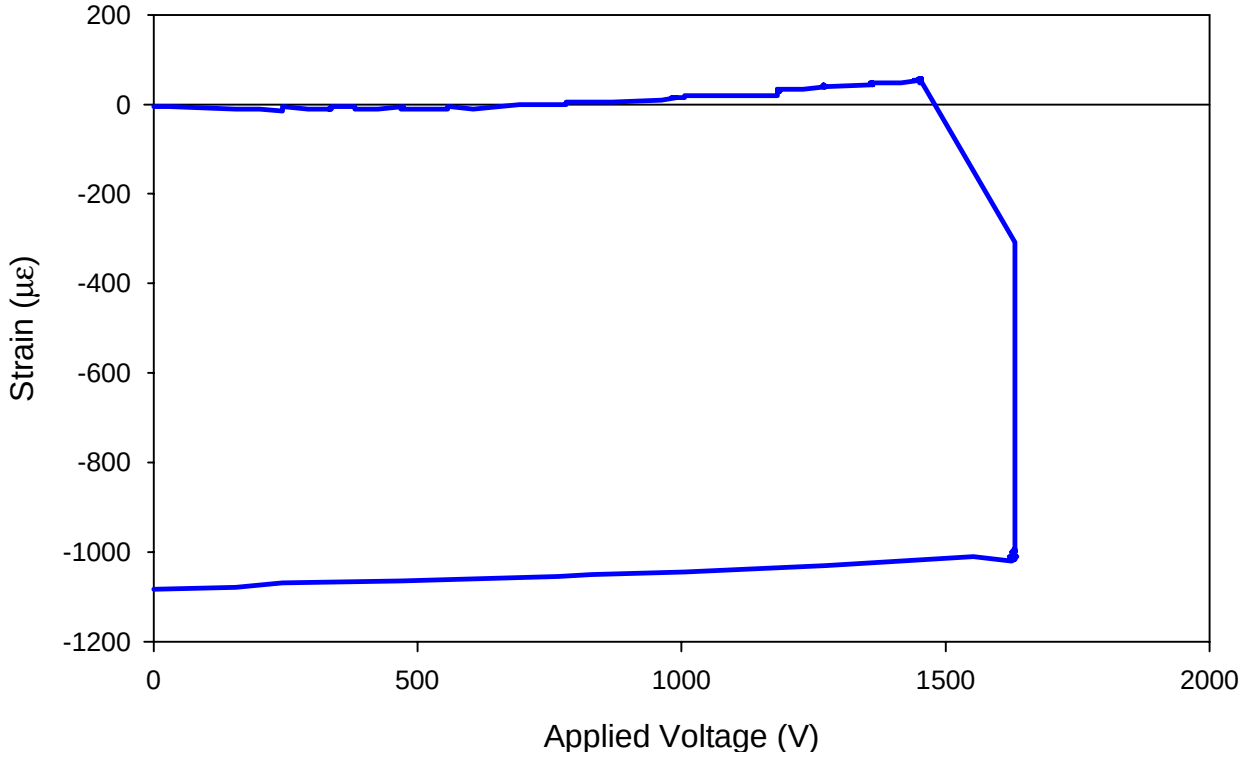

Figure C.6: Strain vs. applied voltage for test hang5

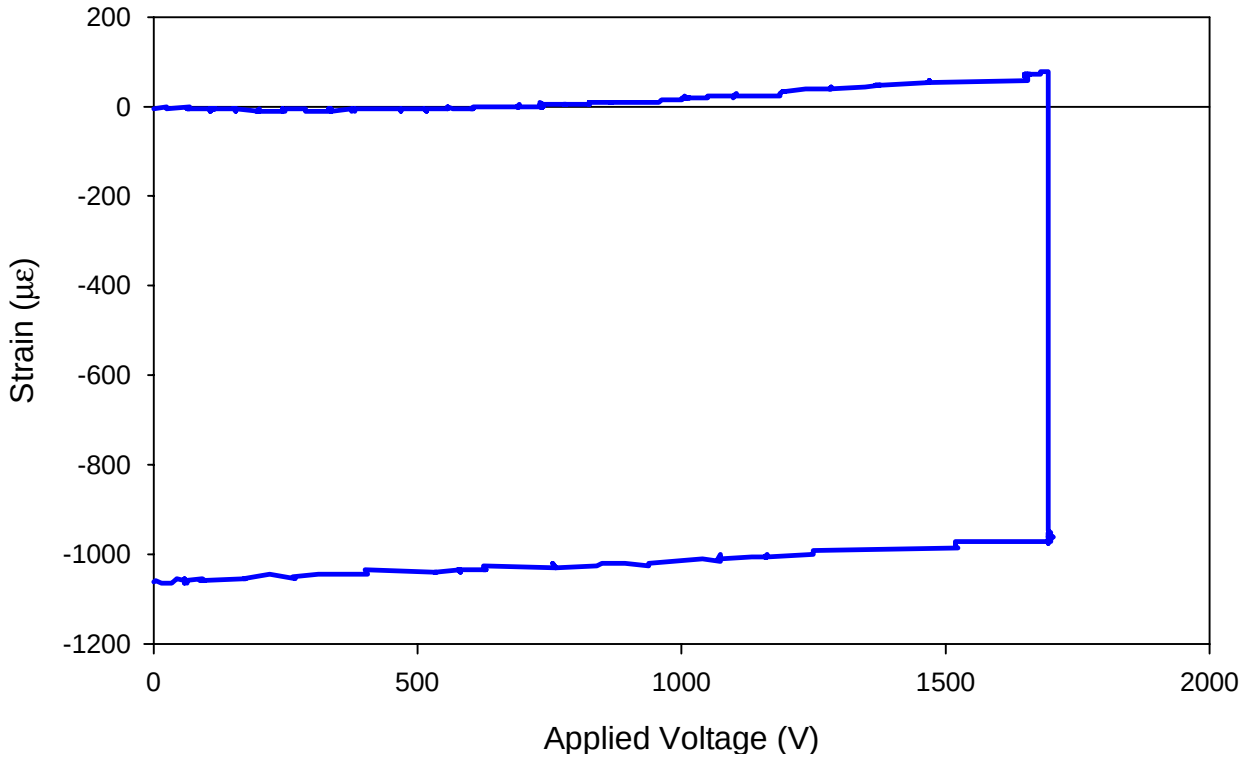

Figure C.7: Strain vs. applied voltage for test hang6

C.2 Laminate Lying With Actuator Up

Figure C.8 shows pictures of the laminate lying on a table with the actuator facing up; this was the position for the actuator-up experiments. Two views of one of the partially-snapped shapes are seen in Figure C.9. In this figure, note that only one corner of the actuator/laminate structure is pointing down, while the other three corners remain pointing up, as they do in the second stable configuration. Figures C.10 – C.17 are the strain versus applied voltage relations for these actuator-up experiments. An example of the strain response for the partial snapping events is seen and is noted in the strain-voltage response of Figure C.11. For the tests where there were three snapping events, the sequence was to have one corner snap first, another two corners snap next, and finally the last corner and the rest of laminate snap.

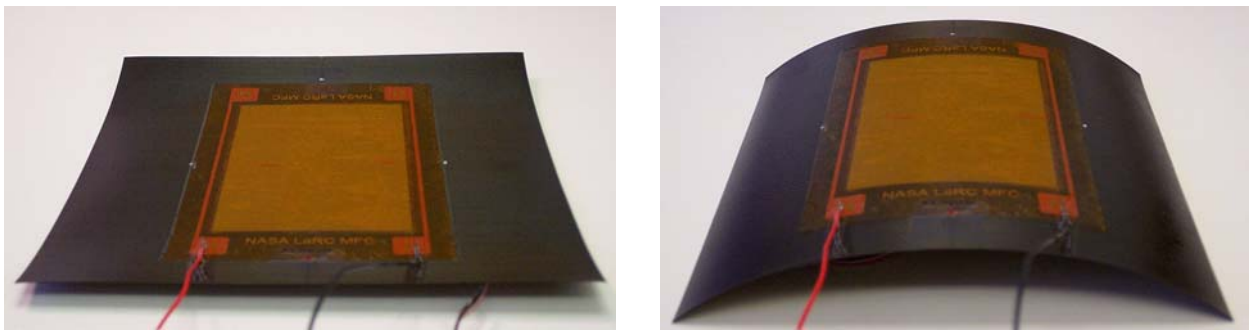

Figure C.8: Pictures of experiment where actuator was facing up

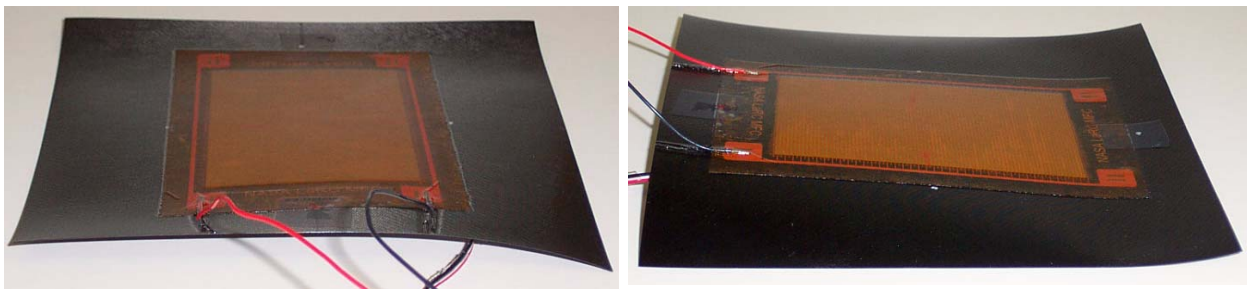

Figure C.9: Two views of a partially-snapped stable shape from actuator-up experiment

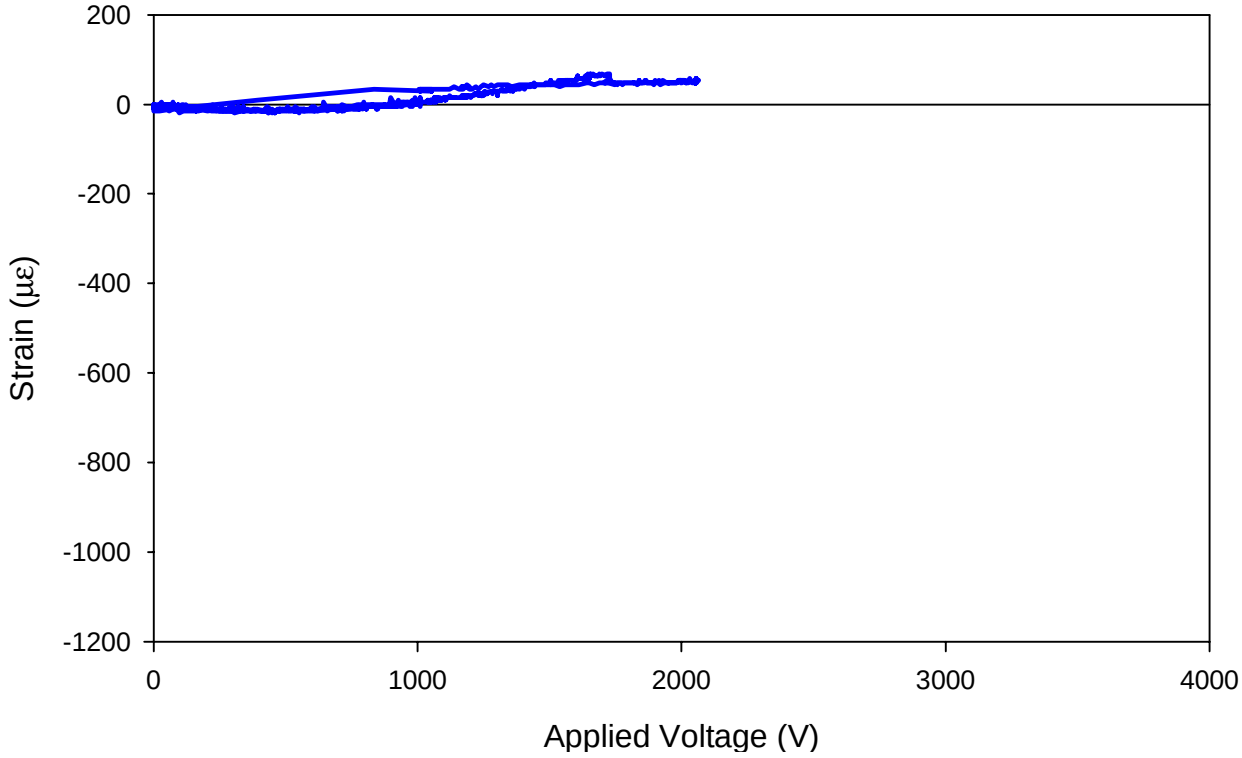

Figure C.10: Strain vs. applied voltage for test up1

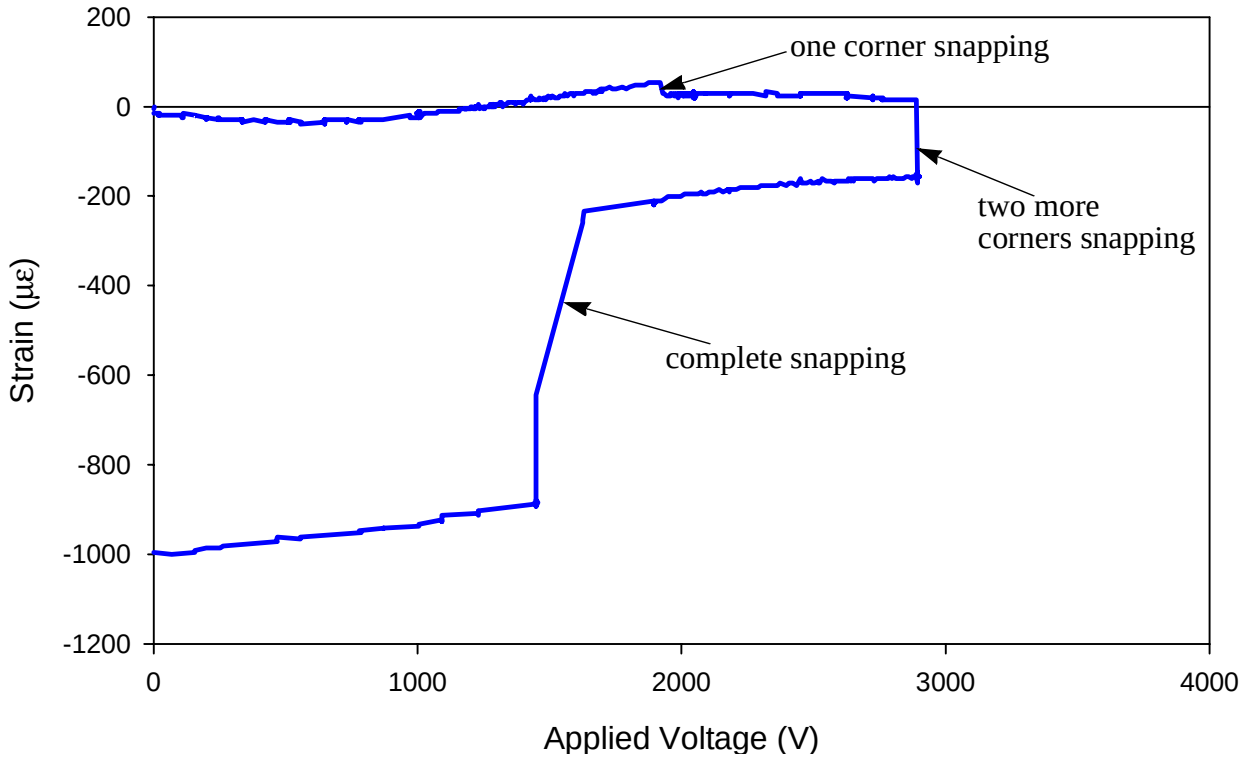

Figure C.11: Strain vs. applied voltage for test up2

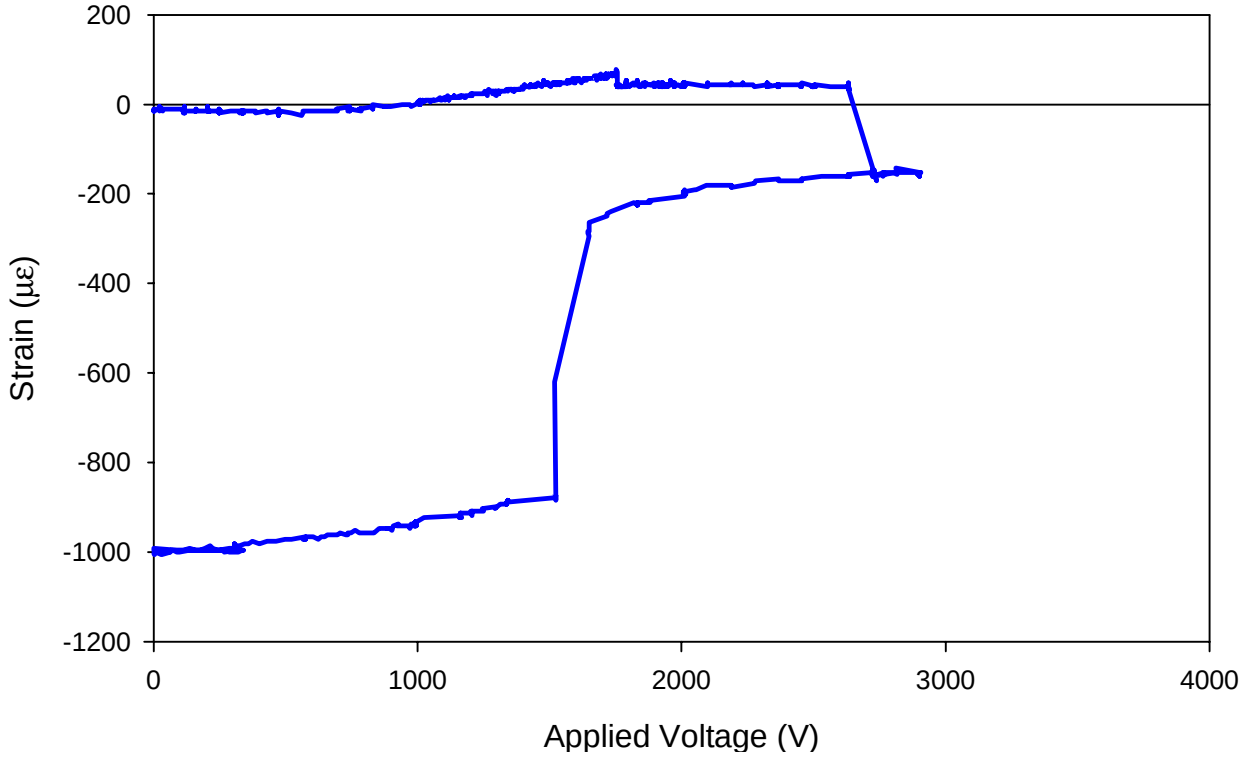

Figure C.12: Strain vs. applied voltage for test up3

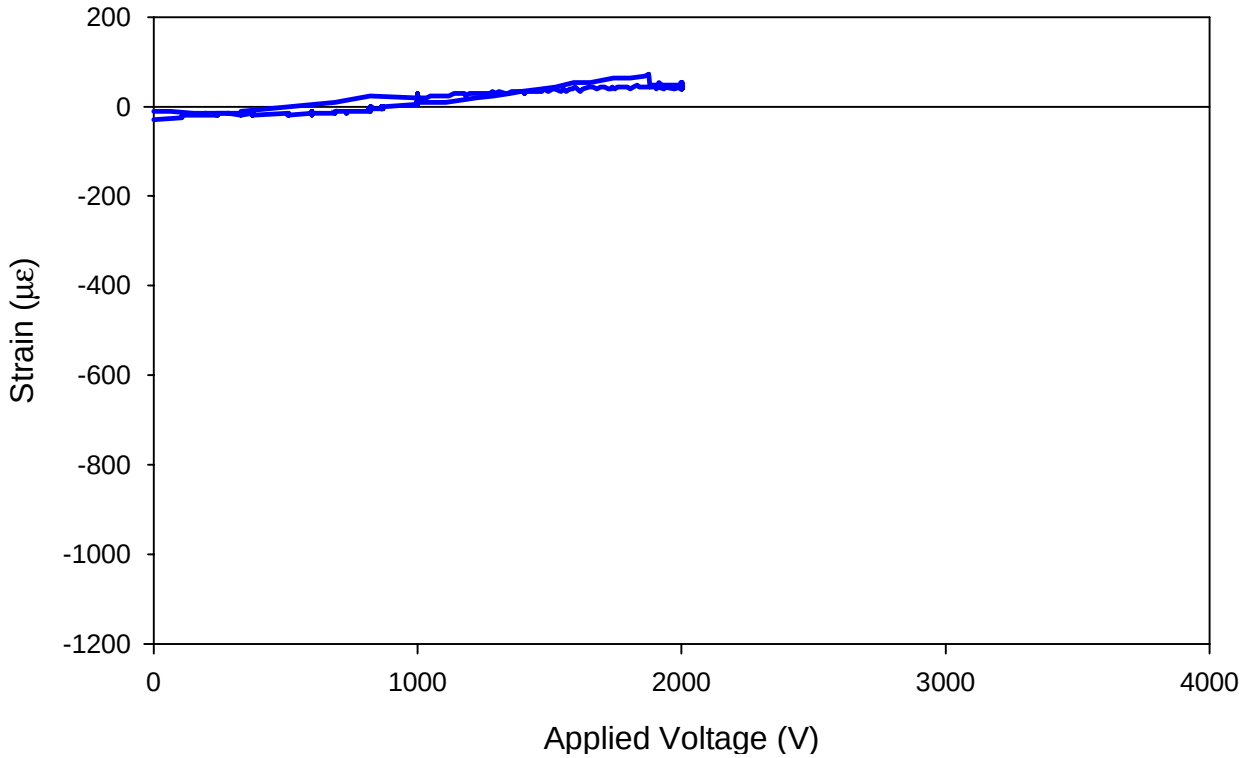

Figure C.13: Strain vs. applied voltage for test up4

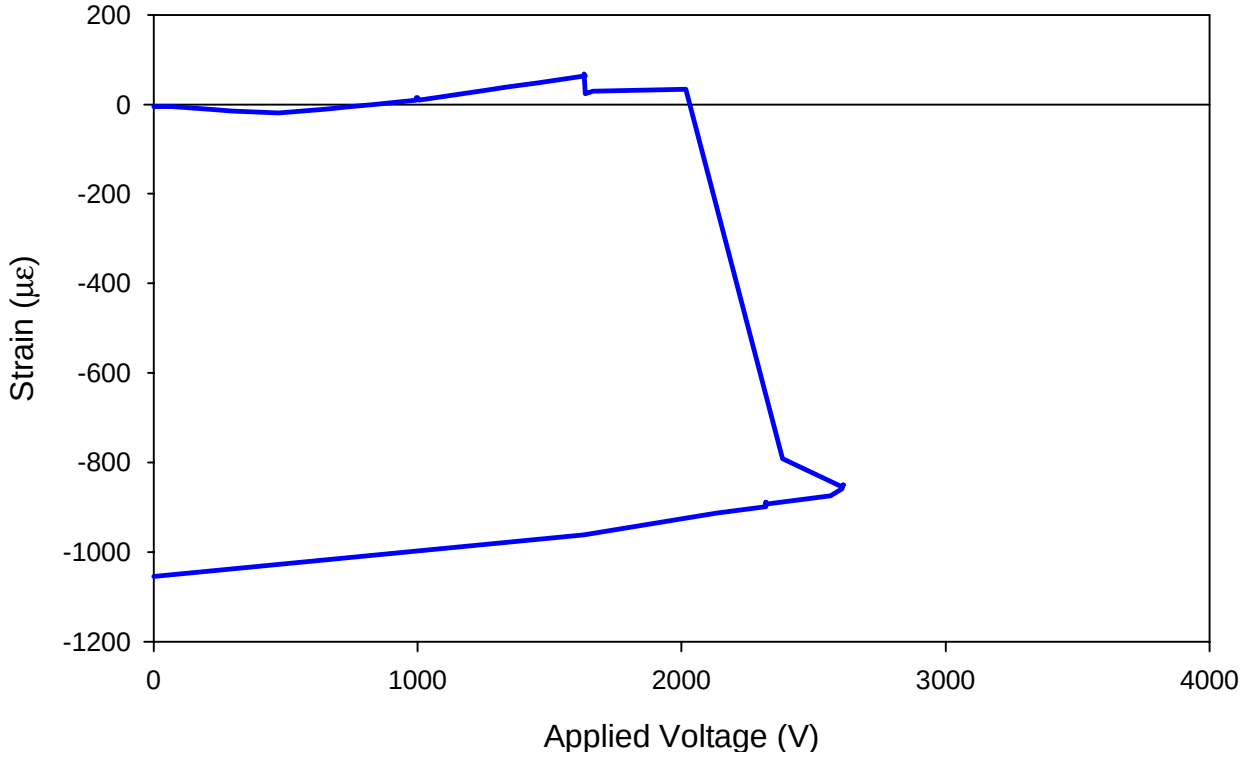

Figure C.14: Strain vs. applied voltage for test up5

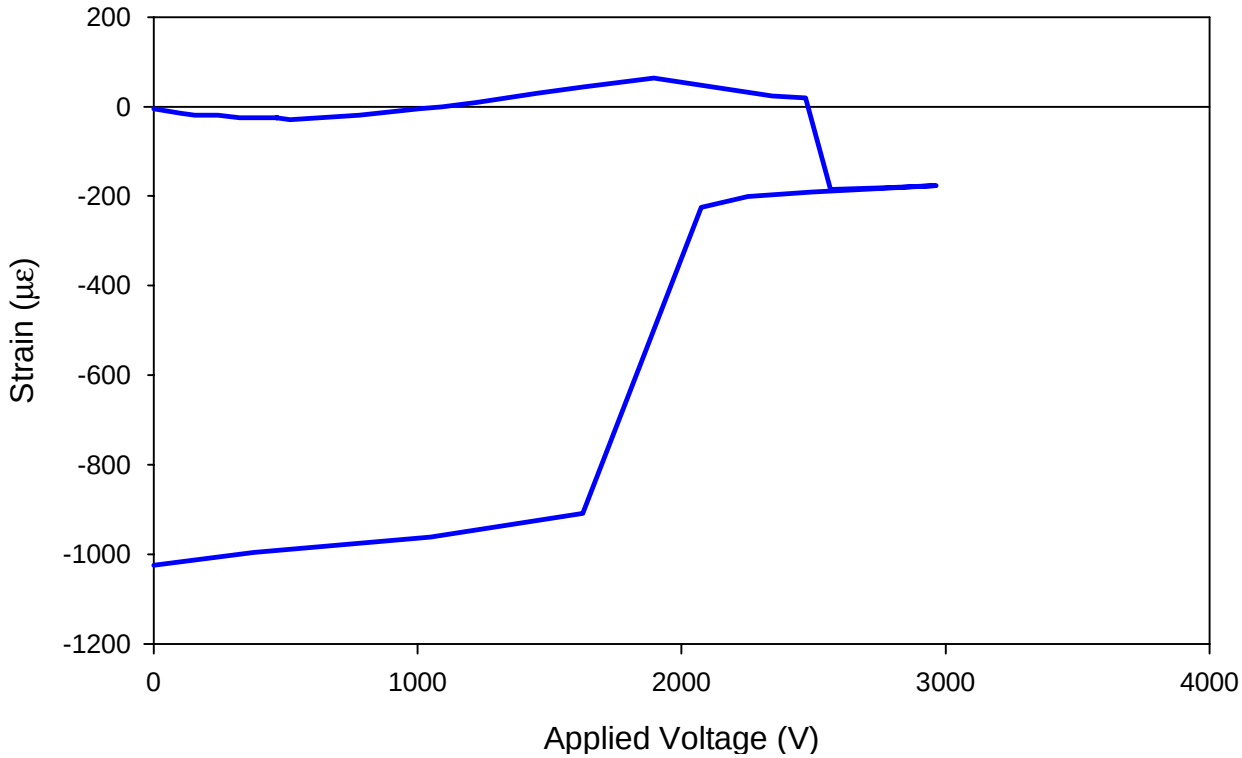

Figure C.15: Strain vs. applied voltage for test up6

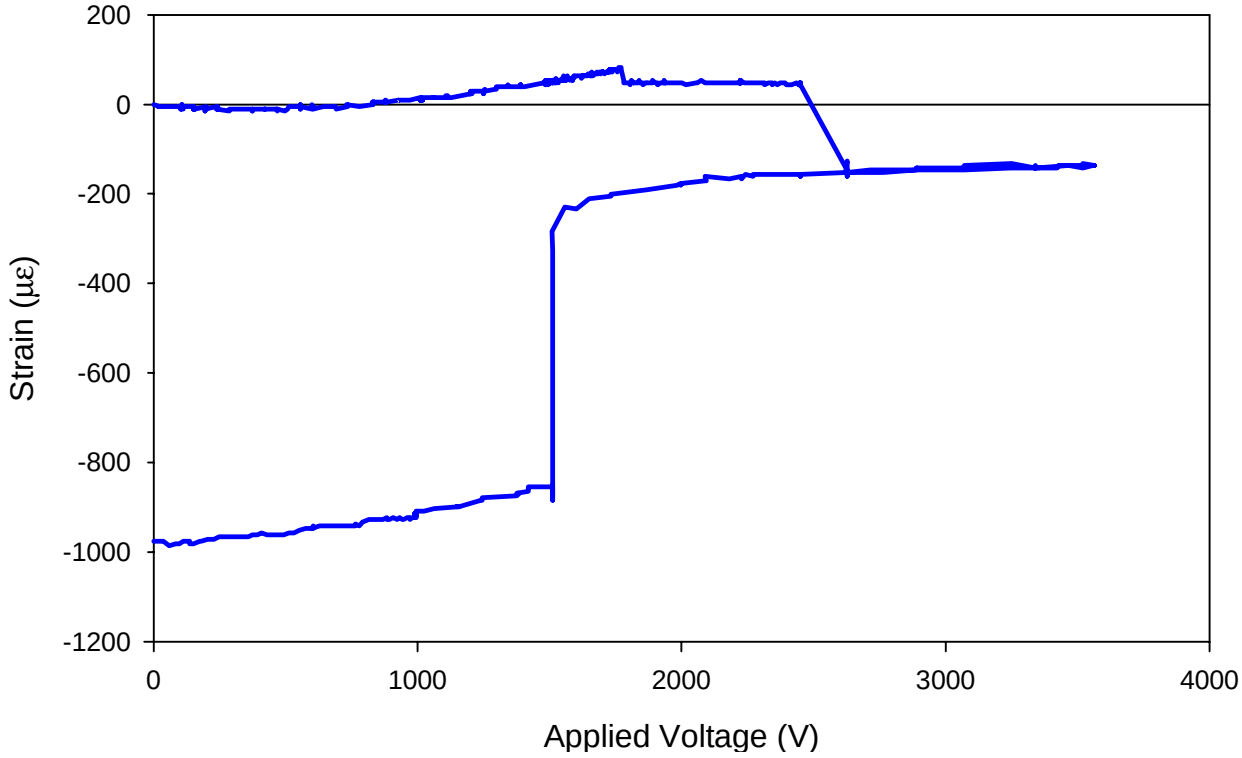

Figure C.16: Strain vs. applied voltage for test up7

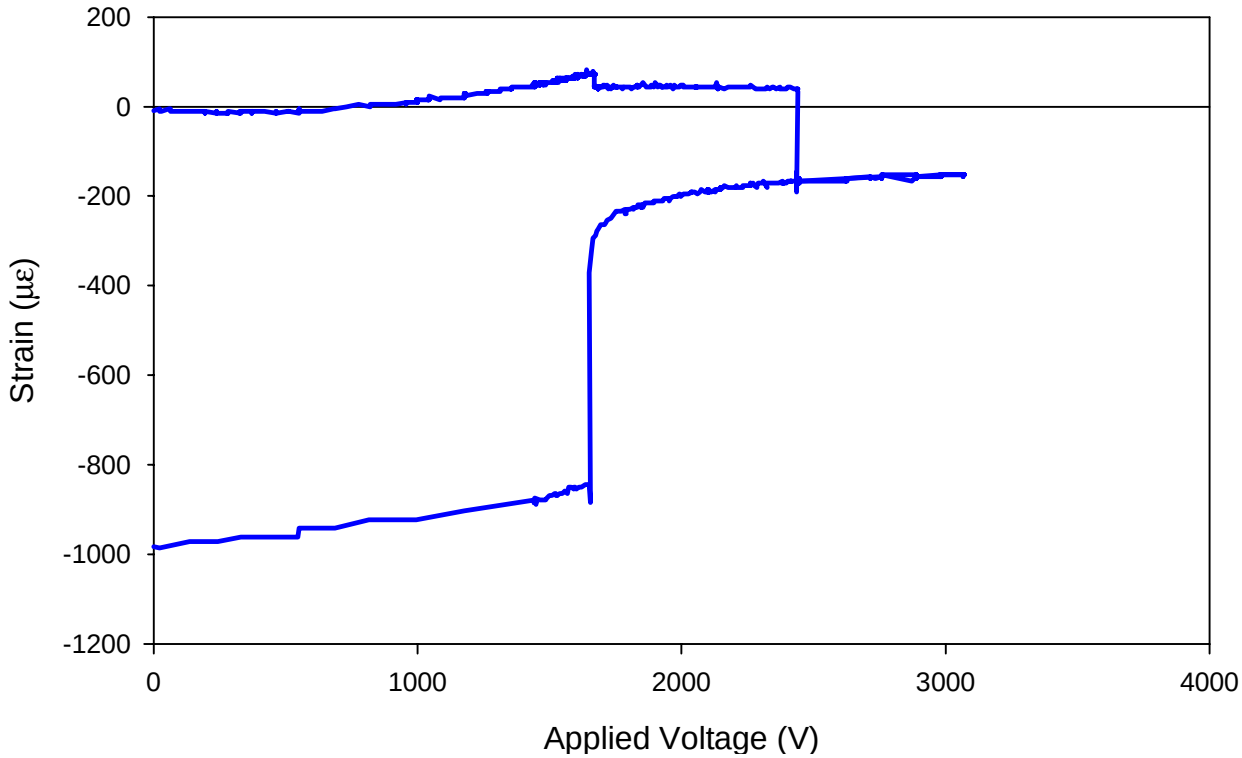

Figure C.17: Strain vs. applied voltage for test up8

C.3 Laminate Lying With Actuator Down

Figure C.18 shows pictures of the laminate lying on a table with the actuator facing down; this was the position for the actuator-down experiments. Figures C.19 – C.31 are the strain versus applied voltage curves for these actuator-down experiments.

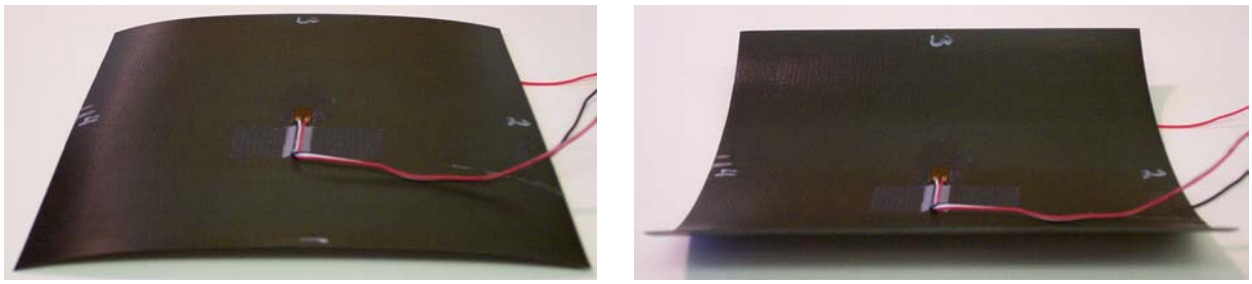

Figure C.18: Pictures of experiment where actuator was facing down

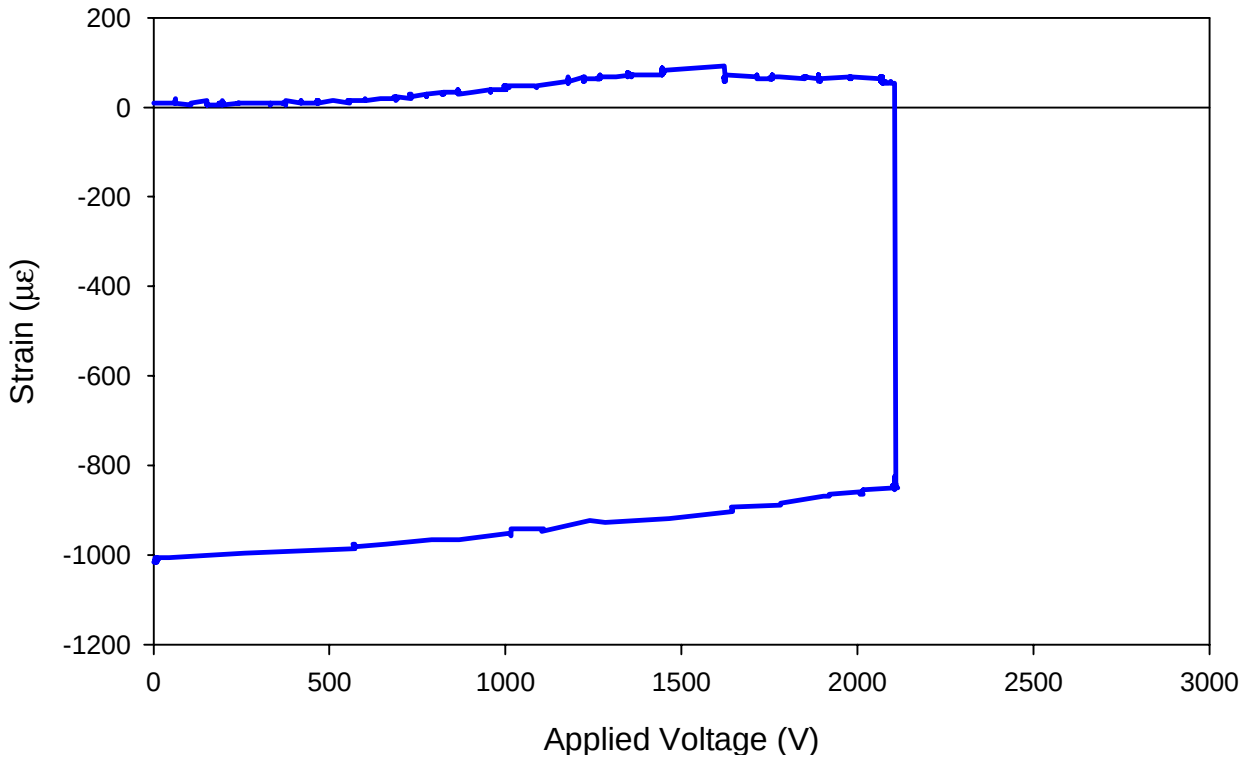

Figure C.19: Strain vs. applied voltage for test down1

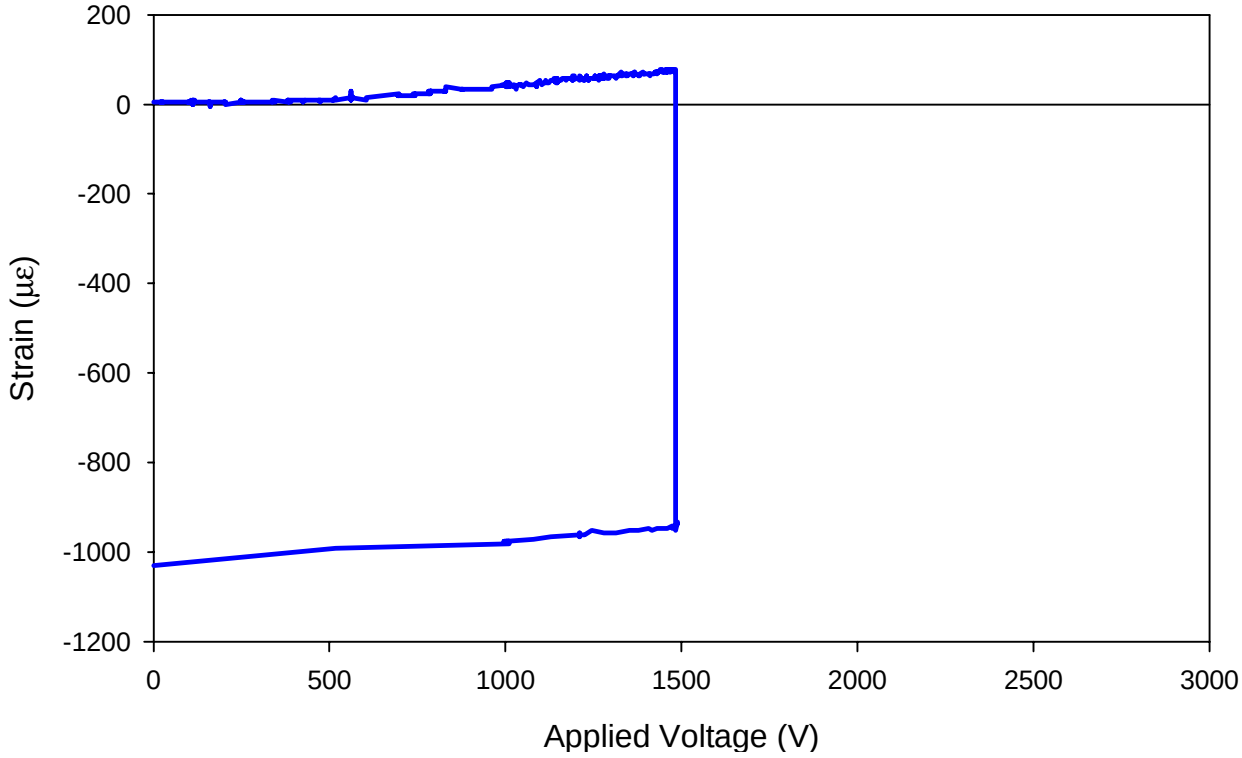

Figure C.20: Strain vs. applied voltage for test down2

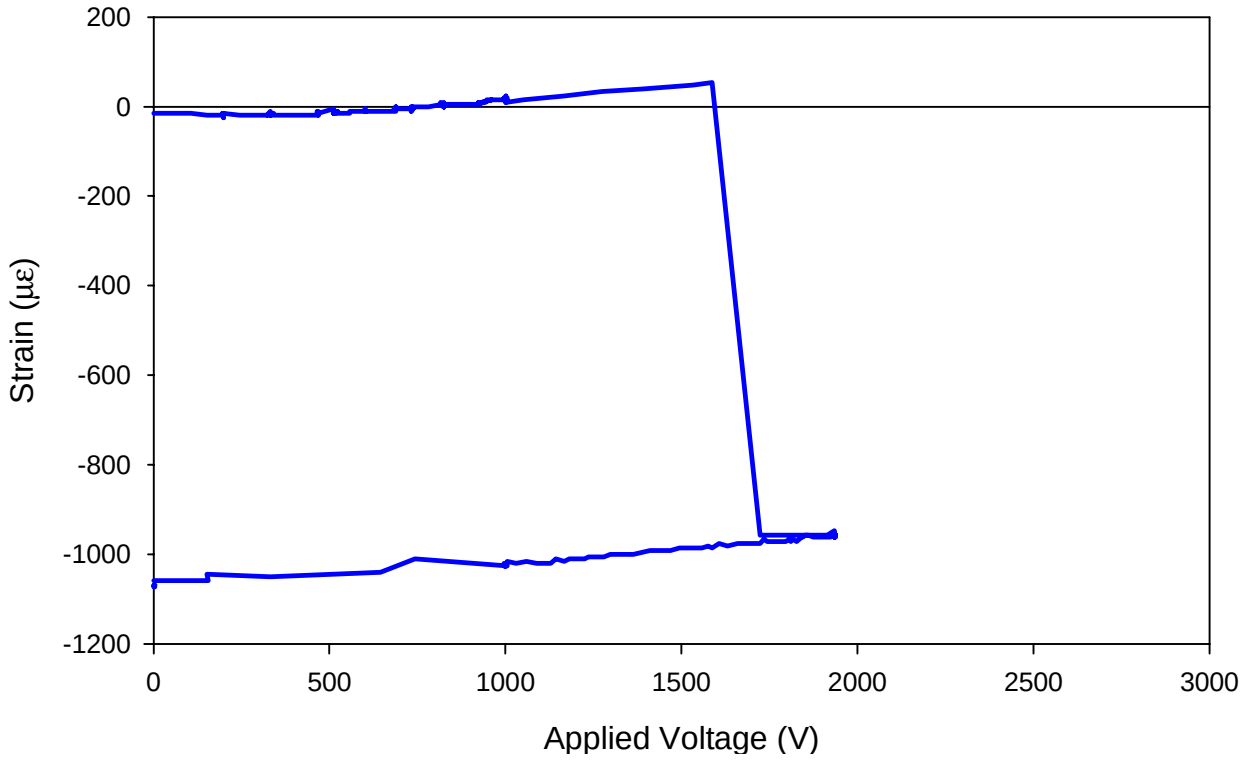

Figure C.21: Strain vs. applied voltage for test down3

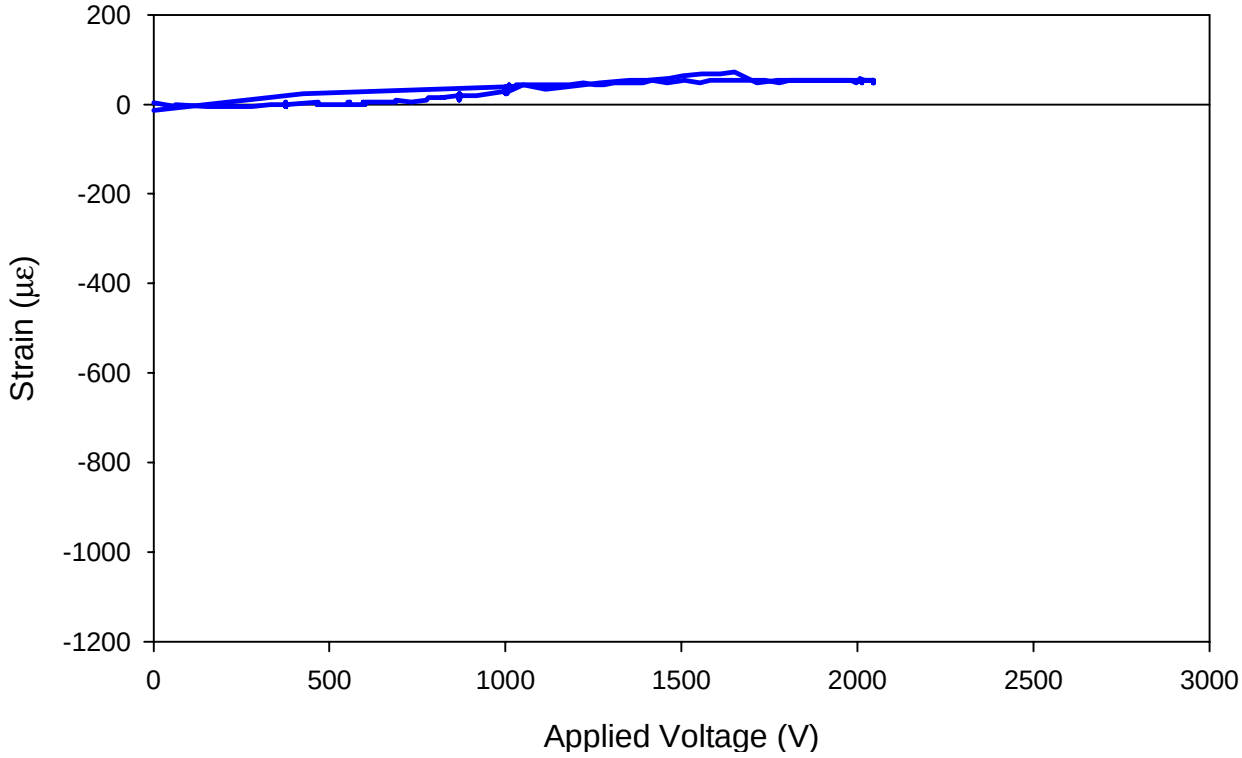

Figure C.22: Strain vs. applied voltage for test down4

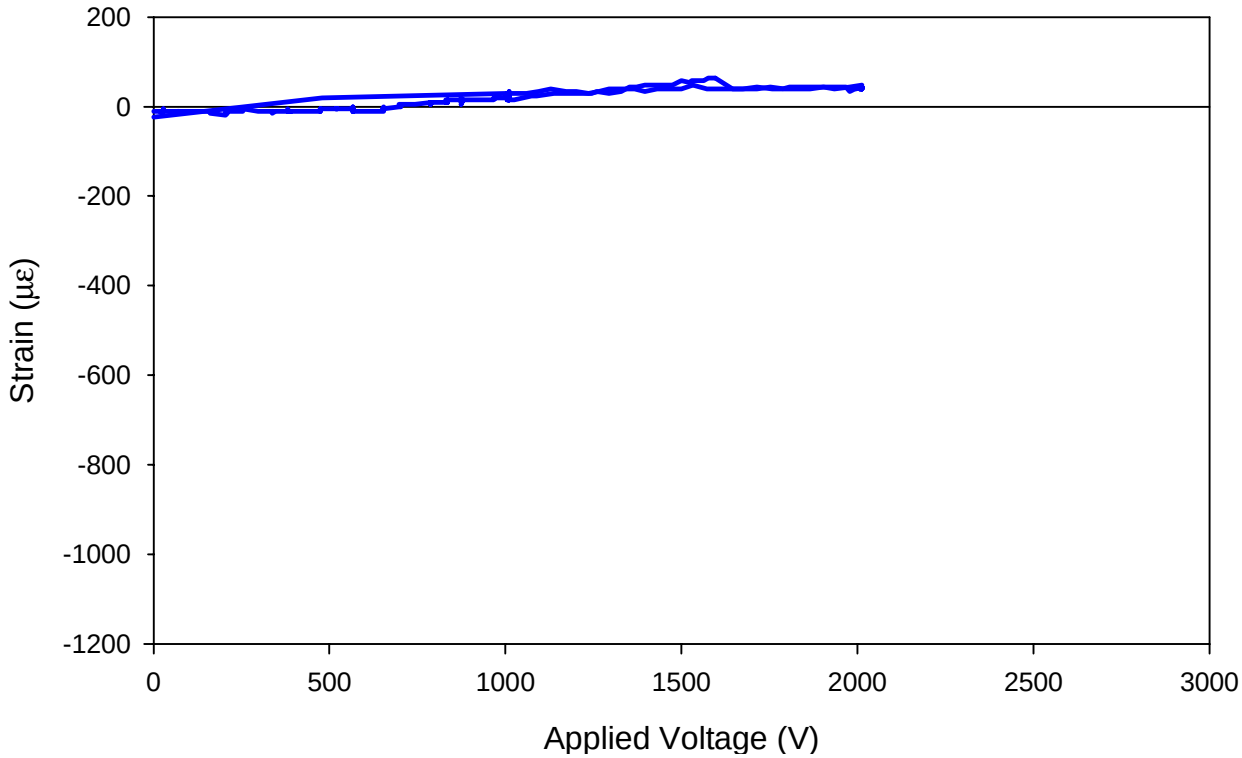

Figure C.23: Strain vs. applied voltage for test down5

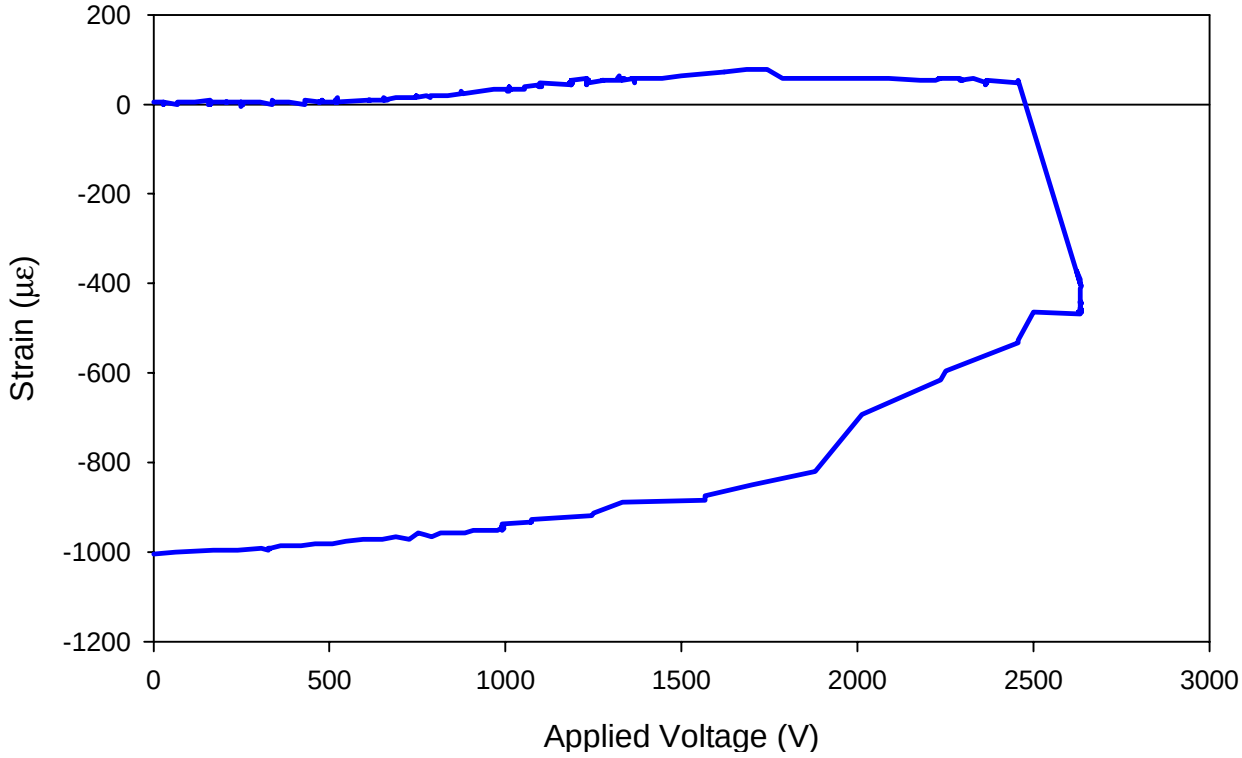

Figure C.24: Strain vs. applied voltage for test down6

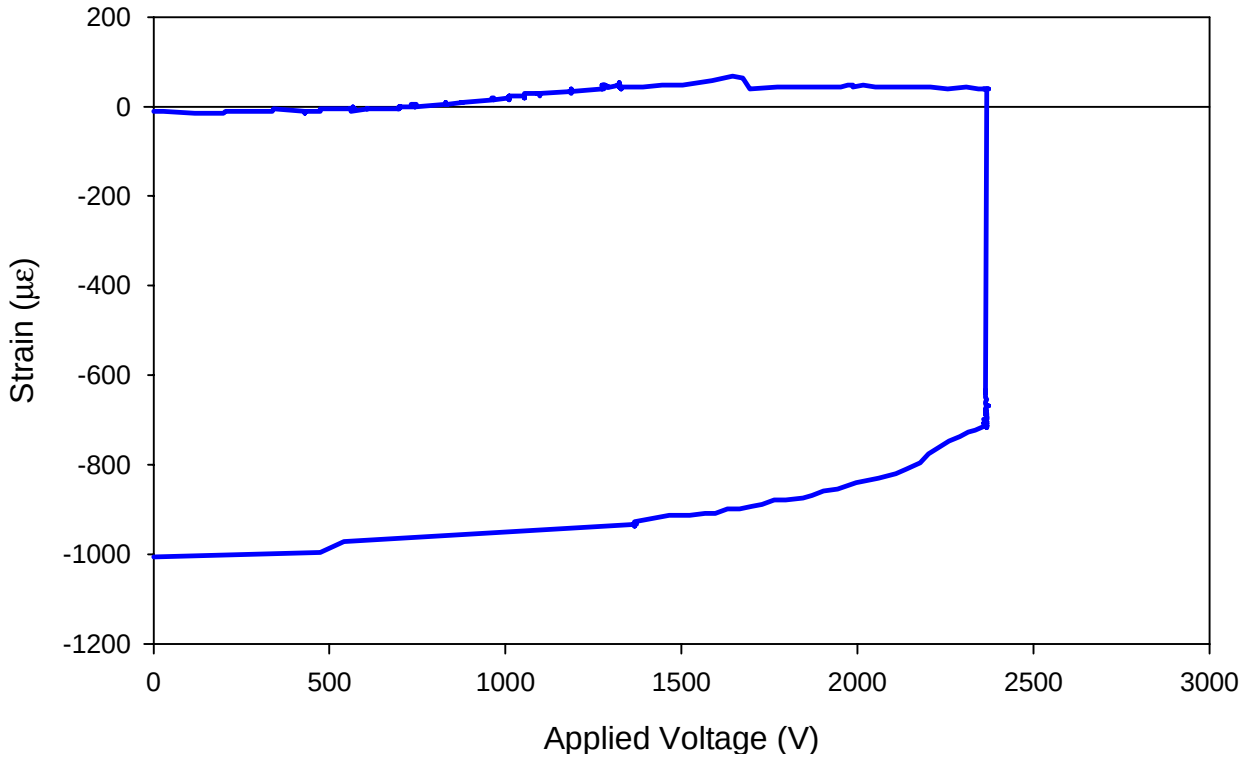

Figure C.25: Strain vs. applied voltage for test down7

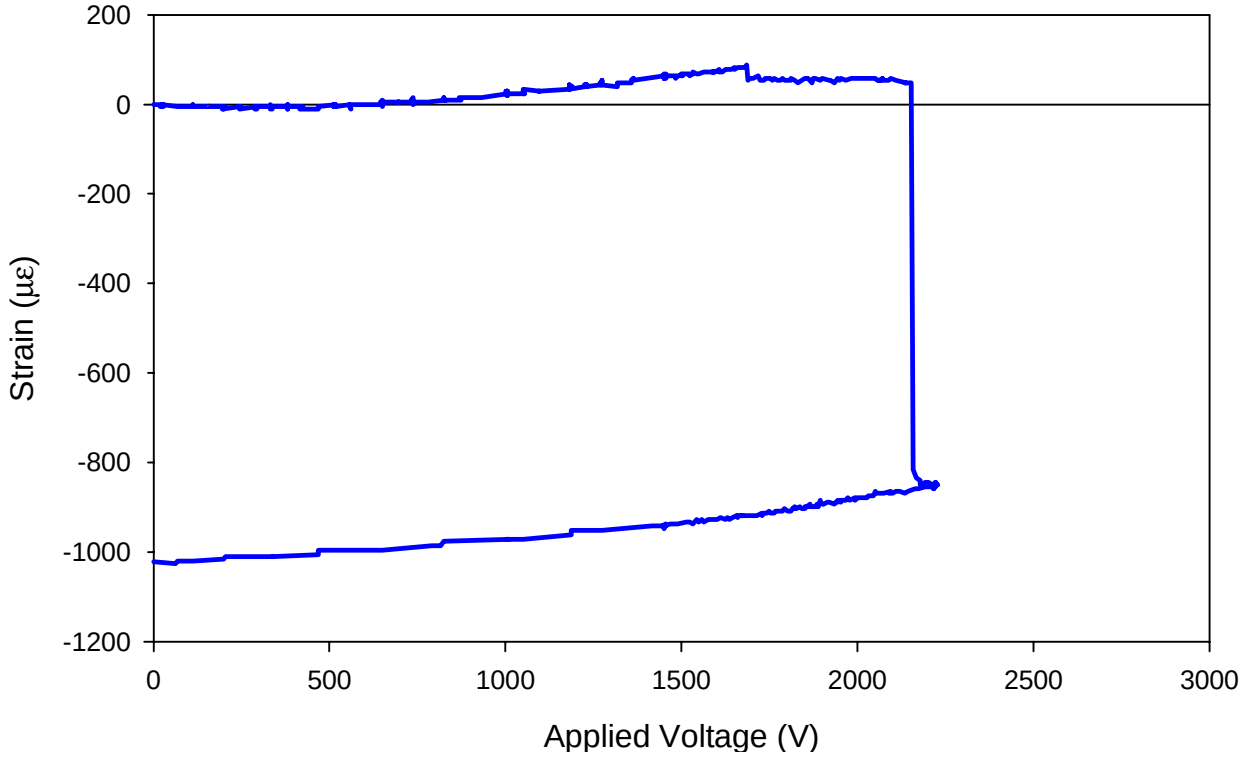

Figure C.26: Strain vs. applied voltage for test down8

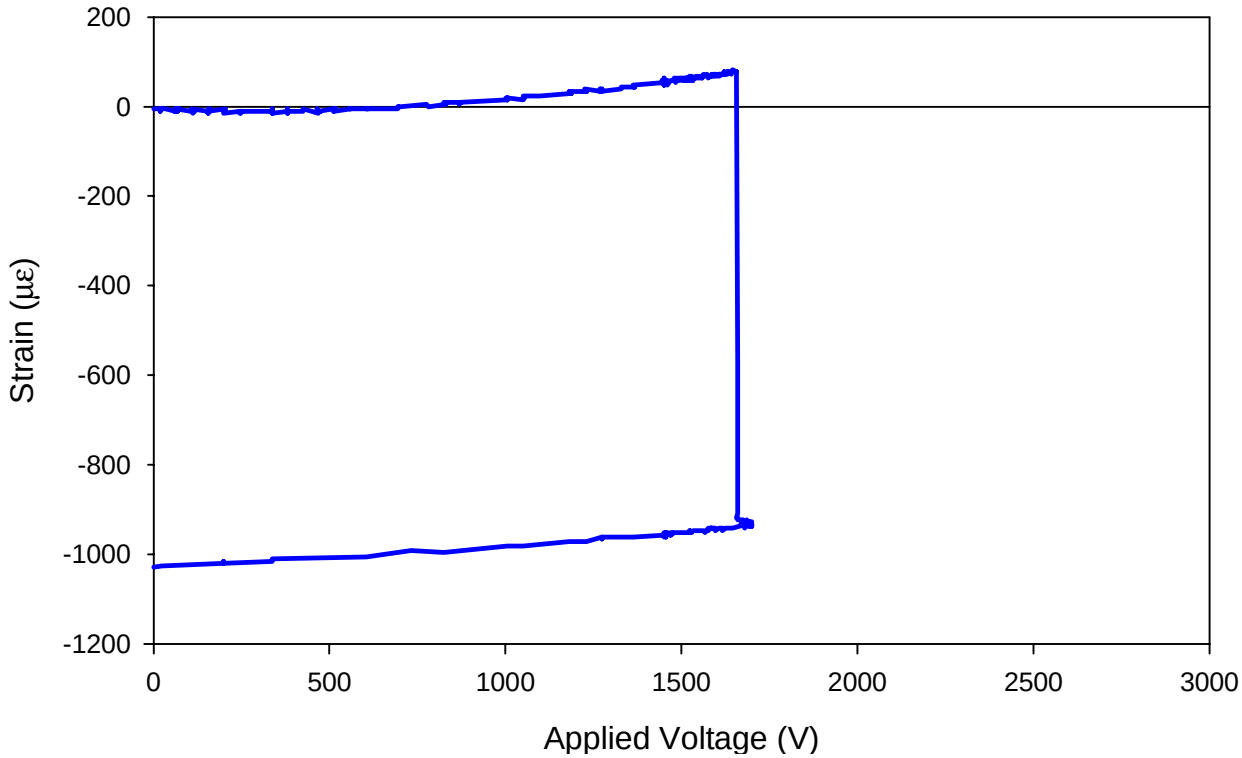

Figure C.27: Strain vs. applied voltage for test down9

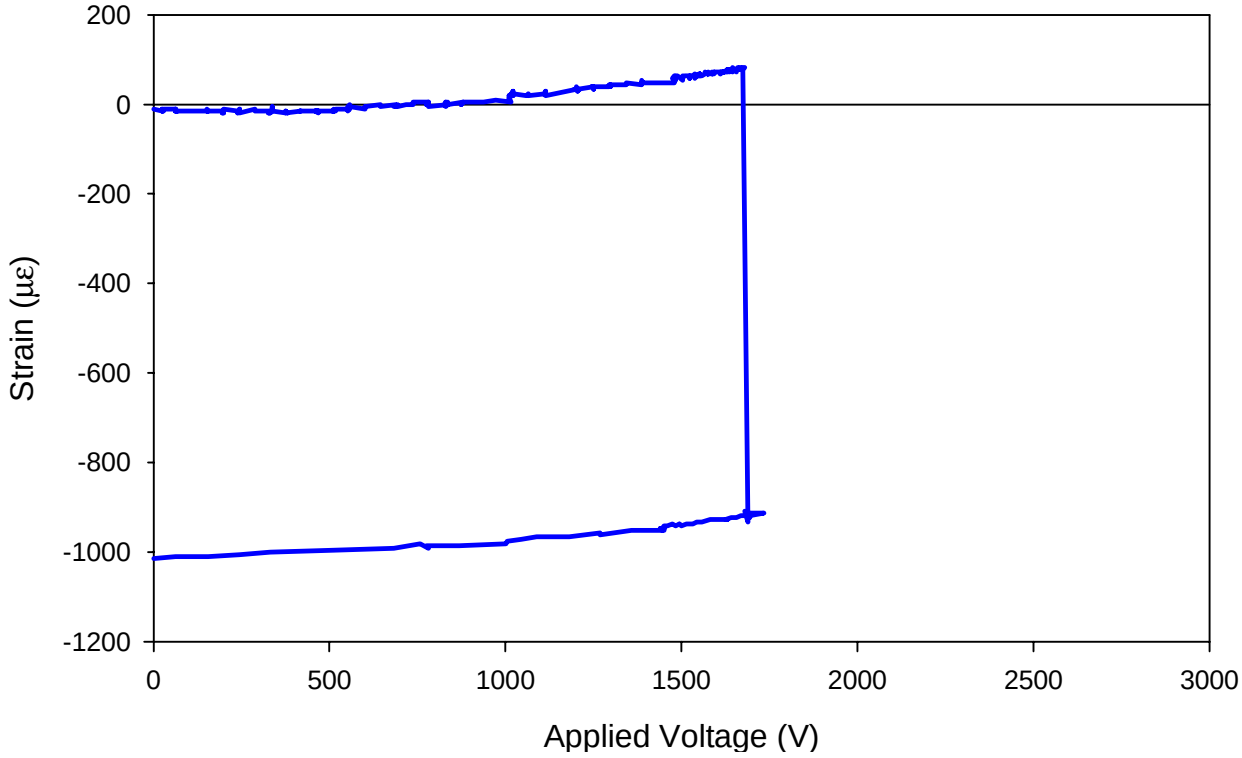

Figure C.28: Strain vs. applied voltage for test down10

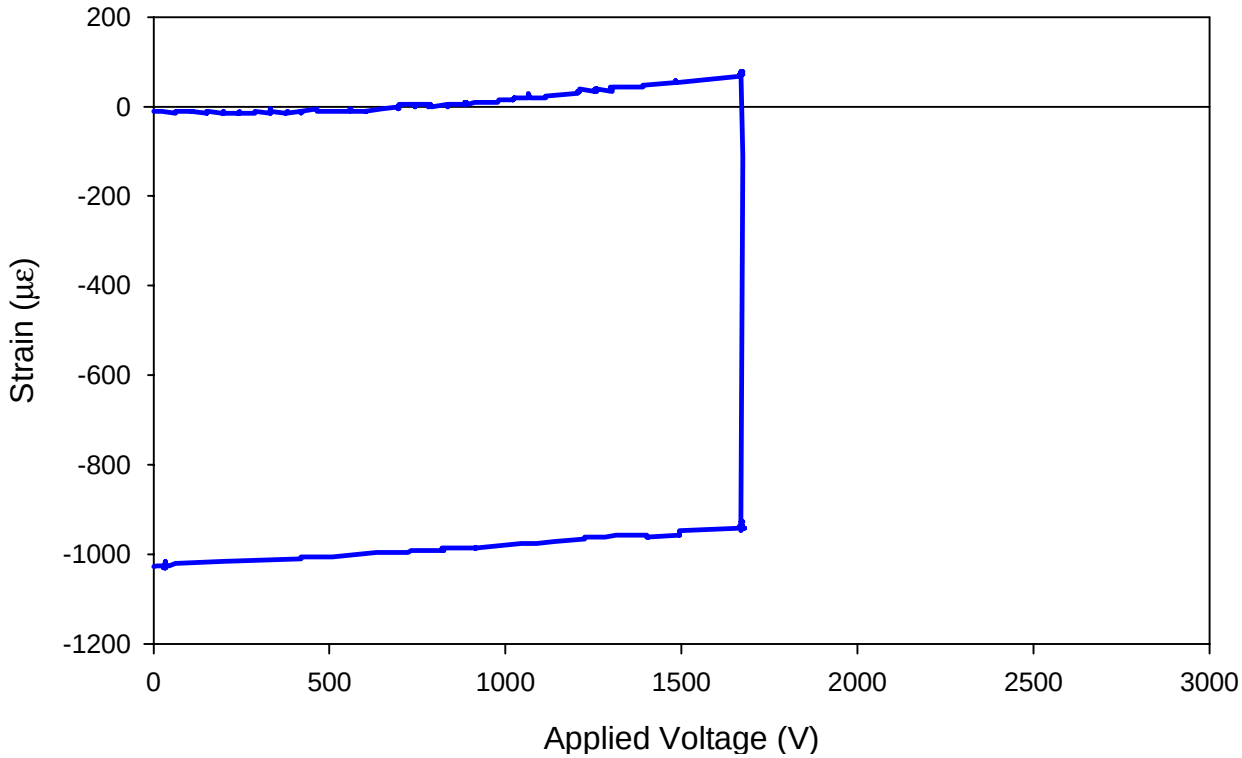

Figure C.29: Strain vs. applied voltage for test down11

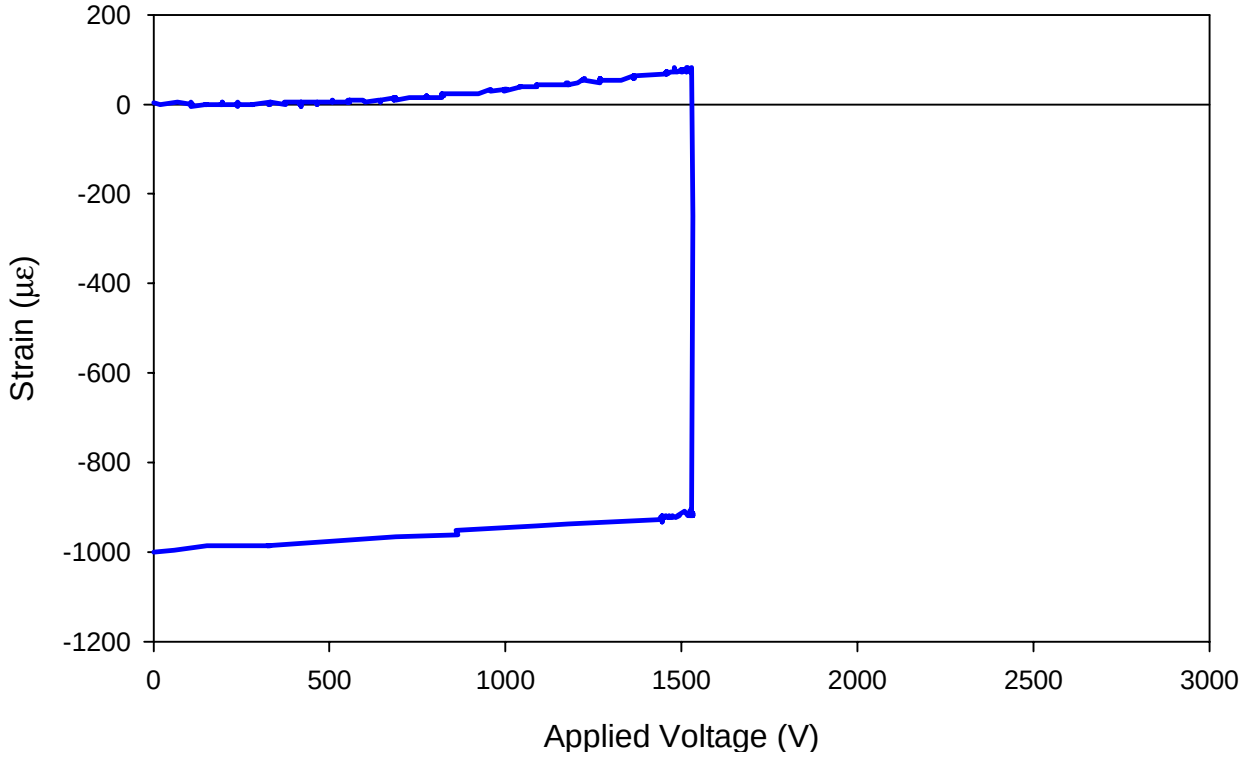

Figure C.30: Strain vs. applied voltage for test down12

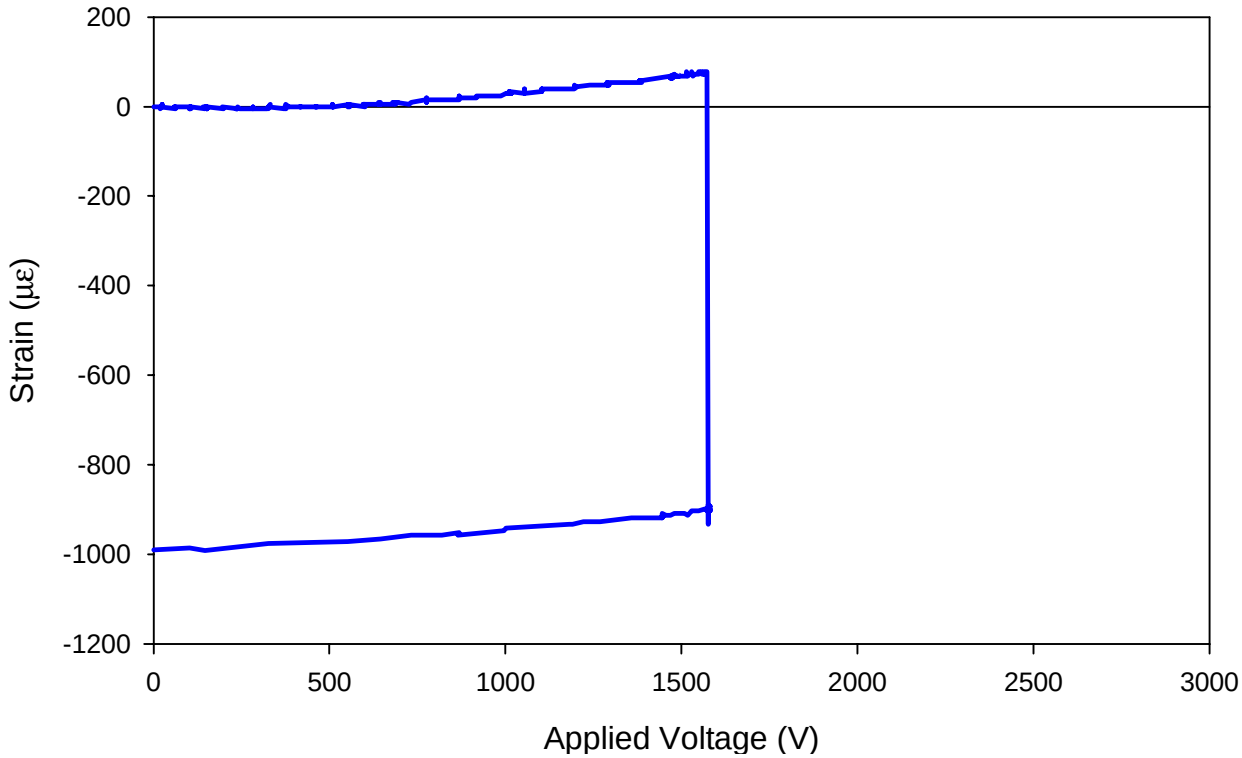

Figure C.31: Strain vs. applied voltage for test down13

Vita

Marc Robert Schultz

Marc Robert Schultz was born on December 17, 1972 and spent his early years in New City, New York. After graduating from Clarkstown Senior High School South in 1991, he attended the State University of New York, University at Buffalo. While an undergraduate, he spent two summers participating in the Summer Undergraduate Research Program sponsored by the National Science Foundation (NSF) Science and Technology Center for High Performance Polymeric Adhesives and Composites at Virginia Polytechnic Institute and State University (Virginia Tech). In 1995, Marc graduated summa cum laude from the University at Buffalo with a Bachelor of Science degree in Mechanical Engineering. Upon graduation, he enrolled at Virginia Tech to pursue graduate studies in the Engineering Mechanics. Marc hiked the entire Appalachian Trail from Georgia to Maine in 1998. Shortly after returning from the Appalachian Trail, Marc successfully defended his Master of Science degree in Engineering Mechanics. On July 13, 2002, Marc married Meagan Heckcrote, the love of his life.